Politechnika Wrocławska

FIELD OF SCIENCE: Engineering and technology (Dziedzina nauk inżynieryjno-technicznych)

DISCIPLINE OF SCIENCE: **Chemical engineering (Inżynieria chemiczna)**

DOCTORAL DISSERTATION

Electrodeposition of ternary zinc–iron–molybdenum and zinc–iron–tungsten alloy coatings designed for corrosion protection of steel

Hafiz Muhammad Shoaib

Supervisor:
dr hab. inż. Juliusz Winiarski, prof. uczelni

Assistant supervisor:
Dr. inż. Anna Mazur-Nowacka

Keywords: electroplating; zinc alloy coatings; protective coatings; corrosion resistance; structure; EIS; TEM; XRD;

WROCŁAW 2026

Acknowledgement

Undertaking this PhD has been a truly life-changing experience for me, and it would not have been possible to do without the support and guidance that I received from my people.

I would like to express my deepest gratitude to my supervisor, **Professor Juliusz Winiarski,** for his invaluable guidance, constant encouragement, feedback, and support throughout the course of this doctoral research. His scientific insight, patience, and critical feedback played a pivotal role in shaping this work and in strengthening my research skills. I am also extremely thankful to my co-supervisor, **Dr**. **Anna Mazur-Nowacka**, for her insightful suggestions and encouragement over the years. Her lab support, teaching guidance, continued motivation, constructive discussions, and comments pushed me to sharpen my thinking and brought greater depth to this work. Special thanks are extended to **Miss Iwona** for their technical assistance and laboratory support. Their contributions were instrumental in the successful completion of this research.

Above all, I owe my heartfelt gratitude to my family for their unconditional love, understanding, and sacrifices. My deepest thanks go to my beloved daughter **Hiba Noor** and son **Muhammad Roman**, who suffered my absence and limited time with remarkable patience during their growing years; this work is dedicated to them. I am profoundly grateful for their silent strength and inspiration. I also wish to thank my friends who stood by me with moral and emotional support, offering encouragement during challenging times and celebrating every small achievement along the way. Without their faith in me, this journey would not have been possible.

Abstract

In the present study, the electrodeposition characteristics, microstructural development, and corrosion resistance of two advanced zinc-based ternary alloys, Zn-Fe-Mo and Zn-Fe-W, electrodeposited from sulphate baths with and without the presence of ammonium ions, have been investigated. The electrochemical characteristics of the alloys have been correlated with the bath composition and the current density of deposition.

Significant changes in the reduction potential of zinc and iron are indicated by cyclic voltammograms. The reduction potential of zinc changes from -1.12 to -1.2 and finally to -1.25 volts versus Ag/AgCl as the electrolyte changes from ammonium sulphate to sodium sulphate solution. Similarly, the iron reduction potential changes from -0.40 to -0.80 and finally to -1.25 volts versus Ag/AgCl as the electrolyte changes from ammonium sulphate to sodium sulphate solution. Co-reduction of molybdenum and tungsten with iron is also indicated by cyclic voltammograms due to the formation of complexes involving the above three metals along with ammonium ions and citrate ions. The presence of complexes is also supported by the UV-Vis spectra obtained from the electrolyte solutions. Continuous evolution of the electrolyte is indicated by spectra due to the complexation of metal ions, redox reactions, and the formation of polynuclear molybdate/tungstate complexes at around 650-880 nm, and depletion of iron is indicated at around 480 nm. The microstructural analysis revealed that the Zn-Fe-Mo coatings deposited within the range of current density used exhibited a compact, nanocrystalline columnar morphology with fibrous, oval-shaped crystallites of 20-40 nm size, whereas the morphology of the Zn-Fe-W coatings was found to be dependent on the current density used, with low current density values ranging from 10-15 mA cm^{-2} resulting in rough, powdery, and porous surfaces, whereas a dense, fine-grained morphology was achieved with a current density of 20 mA cm^{-2}, and a larger current density of 25 mA cm^{-2} resulted in a coarser, nodular morphology. The homogeneous elemental distribution for Zn–Fe–Mo coatings with an Mo content between 0.2 and 5.0 wt.% in the ammonium-containing electrolytes was confirmed by the EDX analysis, which indicated a reduction in the Mo content with an increase in the current density due to the selective deposition of Zn, while the Zn–Fe–W coatings demonstrated an increase in the Fe and W contents in the ammonium-containing electrolytes by the metal-ammonia and metal-citrate complexation mechanisms, with the maximum contents of W reaching 3 to 5 wt.% at a current density of 20 mA cm^{-2}, and the maximum content of Fe 11wt.% at 25 mA cm^{-2}. Surface roughness tests confirmed the SEM results, which found a smooth surface finish of the Zn–Fe–Mo coatings, while there was a

reduction in Ra of the Zn–Fe–W coatings with increasing current density, though lower in ammonium-containing baths due to refinement in nucleation and growth. Cross-sectional analysis of both systems by FIB/SEM presented dense columnar microstructures, although localized interfacial microvoids were observed in Zn–Fe–W coatings prepared from ammonium-containing baths during early stages of deposition due to hydrogen evolution, whereas Zn–Fe–Mo coatings exhibited more uniform through-thickness integrity. The XRD analysis also showed that the Zn-Fe-Mo coatings remained nanocrystalline, with the texture being dependent on the ammonium ions, whereas the Zn-Fe-W coatings showed a phase transformation from Zn- to Fe-Zn intermetallic phases, dominated by the $Fe_{22}Zn_{78}$ phase, when the current density increased, without the presence of tungsten phases due to their low concentration. The electrochemical measurement showed the optimal corrosion behavior at intermediate to high current densities by both alloy systems. In particular, compact microstructures and balanced alloy compositions were achieved at 20 mA cm^{-2}. In the case of the Zn-Fe-Mo coatings, the low corrosion current densities (ranging from 0.3 to 1 µA cm^{-2}), Mo-assisted passivation at low current densities, and high impedance values (with the highest value being 75 kΩ·cm^2 in the case of the Na_2SO_4 derived coatings at 25 mA cm^{-2}) are achieved. In the case of the Zn-Fe-W coatings, the stable corrosion potentials (around -1000 mV vs. Ag|AgCl), the highest polarization resistance at 20 mA cm^{-2}, and the highest values of the barrier resistance (around 6.6 kΩ·cm^2) are achieved. Overall, the results demonstrate strong structure-composition-corrosion relationships in Zn-Fe-Mo as well as Zn-Fe-W, and confirm that optimization of the current density, in association with the ammonium-assisted complexation, is a requirement in order to produce dense, homogeneous, and corrosion-resistant Zn-based ternary alloy coatings.

Streszczenie

W niniejszej rozprawie opisano badania procesu elektroosadzania, kształtowania mikrostruktury oraz odporności na korozję dwóch zaawansowanych powłok stopowych trójskładnikowych na bazie cynku, Zn-Fe-Mo i Zn-Fe-W, osadzanych galwanicznie z kąpieli siarczanowych z dodatkiem i bez udziału jonów amonowych. Charakterystykę elektrochemiczną powłok stopowych skorelowano ze składem kąpieli oraz gęstością prądu osadzania.

Badania woltamperometryczne wykazały znaczne zmiany potencjału redukcji cynku i żelaza. Potencjał redukcji cynku zmienia się z −1,12 do −1,2, a ostatecznie do −1,25 V wzgl. Ag|AgCl, gdy w elektrolicie zamiast siarczanu amonu obecny jest siarczan sodu. Podobnie, potencjał redukcji żelaza zmienia się z −0,40 do −0,80, a ostatecznie do −1,25 V wzgl. Ag|AgCl. Na współosadzanie molibdenu i wolframu z żelazem wskazują również krzywe woltamperometryczne, co wynika z tworzenia kompleksów z udziałem trzech metali tworzących powłokę wraz z jonami amonowymi i cytrynianowymi. Obecność kompleksów potwierdzają również widma UV-Vis zmierzone w kąpielach. Zmiany jakościowe w kąpielach są widoczne na widmach i są związane z kompleksowaniem jonów metali, reakcjami redoks i tworzeniem kompleksów molibdenianowych / wolframianowych przy około 650-880 nm, a malejącym udziałem form kompleksowych żelaza przy około 480 nm. Analiza mikrostrukturalna wykazała, że powłoki Zn-Fe-Mo osadzone w zakresie użytej gęstości prądu wykazywały zwartą, nanokrystaliczną i kolumnową strukturę z włókniście ułożonymi owalnymi krystalitami o rozmiarze 20-40 nm. Morfologia powłok Zn-Fe-W okazała się być silnie zależna od użytej gęstości prądu, przy czym niskie wartości gęstości prądu w zakresie 10-15 mA cm^{-2} skutkowały powłokami szorstkimi, proszkowymi i porowatymi, podczas gdy zwartą, drobnoziarnistą powłokę osadzono dopiero przy gęstości prądu 20 mA cm^{-2}. Z kolei powłoki osadzone przy gęstość prądu 25 mA cm^{-2} były już wyraźnie gruboziarniste. Jednorodny rozkład pierwiastków dla powłok Zn-Fe-Mo (zawierających Mo w ilości od 0,2 do 5,0 % mas.) osadzonych w kapieli zawierającej jony amonowe został potwierdzony analizami EDX. Analizy te wskazały na zmniejszenie zawartości Mo wraz ze wzrostem gęstości prądu osadzania z powodu selektywnego osadzania Zn, podczas gdy powłoki Zn-Fe-W wykazały wzrost zawartości Fe i W w kapielach zawierających jony amonowe poprzez mechanizmy kompleksowania metal-jon amonowy i metal-jon cytrynianowy, przy czym maksymalna zawartość W osiągnęła od 3 do 5 % mas. przy gęstości prądu 20 mA cm^{-2}, a maksymalna zawartość Fe 11 % mas. przy 25 mA cm^{-2}. Badania chropowatości powierzchni

są zgodne z wynikami analiz SEM i wykazały gładką powierzchnię powłok Zn-Fe-Mo, podczas gdy wraz ze wzrostem gęstości prądu obserwowano zmniejszenie chropowatości, Ra, powłok Zn-Fe-W, choć niższego w kąpielach zawierających jony amonowe ze względu na rozdrobnienie ziarna. Analiza przekrojów poprzecznych obu powłok metodą FIB/SEM wykazała ich zwartą kolumnową budowę, chociaż w powłokach Zn-Fe-W osadzonych z kąpieli zawierających siarczan amonu, najprawdopodobniej z powodu wydzielania wodoru we wczesnym etapie osadzania, zaobserwowano drobne puste przestrzenie, podczas gdy powłoki Zn-Fe-Mo charakteryzowały się bardziej równomierną budową na całym przekroju. Analiza XRD wykazała, że powłoki Zn-Fe-Mo zachowały strukturę nanokrystaliczną, a ich tekstura zależała od obecności jonów amonowych w kąpieli. W przypadku powłok Zn-Fe-W wraz ze wzrostem gęstości prądu zaobserwowano wyraźną zmianę w składzie fazowym – przejście z fazy Zn w fazę międzymetaliczną Fe-Zn, zbliżoną składem do $Fe_{22}Zn_{78}$, bez obecności faz bogatych w wolfram ze względu na jego niską zawartość. Pomiary korozyjne wykazały najlepszą odporność na korozję obu rodzajów powłok stopowych przy średnich i wysokich gęstościach prądu osadzania. Zwarte powłoki stopowe o dobrej jakości uzyskano zwłaszcza przy gęstości prądu 20 mA cm^{-2}. W przypadku powłok Zn-Fe-Mo uzyskano niskie gęstości prądu korozyjnego (w zakresie od 0,3 do 1 μA cm^{-2}), pewne właściwości pasywne wspomagane obecnością molibdenu przy niskich gęstościach prądu oraz wysokie wartości impedancji (nawet do 75 kΩ cm^2 w przypadku powłok z kąpieli zawierających Na_2SO_4 przy 25 mA cm^{-2}). W przypadku powłok Zn-Fe-W uzyskano stabilne potencjały korozji (około −1,0 V względem Ag|AgCl), najwyższą rezystancję polaryzacji przy 20 mA cm^{-2} oraz najwyższe wartości rezystancji powłok (około 6,6 kΩ cm^2). Ogólnie rzecz biorąc, wyniki wskazują na silne powiązania między strukturą, składem i odpornością na korozję powłok stopowych Zn-Fe-Mo i Zn-Fe-W. Badania potwierdzają, że dobór odpowiedniej gęstości prądu oraz prowadzenie procesu elektroosadzania w kąpielach siarczanowych zawierających jony amonowe jest wymogiem koniecznym do wytworzenia zwartych, jednorodnych i odpornych na korozję powłok stopowych Zn-Fe-Mo i Zn-Fe-W.

Abbreviations:

Zn – Zinc

Fe – Iron

Mo – Molybdenum

W – Tungsten

Zn–Fe–Mo – Zinc–Iron–Molybdenum Alloy Coating

Zn–Fe–W – Zinc–Iron–Tungsten Alloy Coating

Na_2SO_4 – Sodium Sulphate

$(NH_4)_2SO_4$ – Ammonium Sulphate

NaCl – Sodium chloride

NH_4^+ – Ammonium Ion

CV – Cyclic Voltammetry

Ag|AgCl – Silver/Silver Chloride Reference Electrode

UV–Vis – Ultraviolet–Visible Spectroscopy

mA cm^{-2} – Milliampere per Square Centimetre

SEM – Scanning Electron Microscopy

EDX – Energy-Dispersive X-ray Spectroscopy

FIB/SEM – Focused Ion Beam / Scanning Electron Microscopy

XRD – X-ray Diffraction

Fe_xZn_x – Iron–Zinc Intermetallic Phase

Ra – Arithmetic Average Surface Roughness

LPR – Linear Polarization Resistance

Rp – Polarization Resistance

EIS – Electrochemical Impedance Spectroscopy

Ecorr – Corrosion Potential

icorr – Corrosion Current Density

CPE – Constant Phase Element

wt.% – Weight Percent

R_1 – Solution Resistance

R_2 – Surface Layer Resistance

R_3 – Charge-Transfer (Barrier) Resistance

CPE-p – Constant Phase Element Parameter (Capacitance Term)

CPE-T – Constant Phase Element Exponent

Warburg Element (W) – Diffusion Impedance Element

θ – Phase angle

χ^2 – Chi-squared goodness-of-fit parameter

EDXS – Energy Dispersive X-ray Spectroscopy

EEC – Electrical Equivalent Circuit

βa – Anodic Tafel slope

βc – Cathodic Tafel slope

Table of Contents

Chapter 1

1.1 Overview:

Electrodeposition of Zinc and Zinc alloys is extensively used in many industries and has distinctive advantages over other finishing processes. In practice, Zn-Ni and Zn-Co coatings require harmful metal salts with Ni(II) and Co(II) ions as compared to the Zn-Fe coating with iron(II) sulphate salt, which is less harmful. Many extensive research works have been reported on the deposition mechanism of Zn-Fe group metal alloys. It has been concluded that deposition of zinc with iron metal (Zn-Fe) alloy coating shows good resistance to corrosion as compared to single metal deposition[1], [2]. Another possibility to modify the properties of binary zinc alloy coatings is to introduce a third alloying component characterized by high corrosion resistance and better mechanical properties than zinc and an iron group metal (Zn-Fe). One of the potential choices here is molybdenum. It is known from the literature on the subject that, if introduced into a nickel coating, molybdenum improves its utility properties, such as hardness, wear resistance, and corrosion resistance [3]. Therefore, it is more convenient to use a zinc and iron (Zn-Fe) alloy coating in addition to a molybdenum or tungsten, or Zn-Fe-Mo (or Zn-Fe-W) ternary alloy coatings.

It has been proved that the influence of Mo concentration in Zn-Fe alloy coating has more corrosion resistance potential as compared to Zn-Fe alloy coating[4]. Much higher microhardness resulted when molybdenum was introduced into a two-component system like Zn-Ni and Zn-Co [5], [6].

Electrodeposition of metal Mo from aqueous solution is difficult because of the high oxidation state of the Mo ion; however, electrodeposition of metallic Mo is possible under co-deposition with iron-group elements, referred to as the principal of induced co-deposition[7]. Zinc coatings containing iron and molybdenum showed significantly higher indentation microhardness than Zn and other binary zinc alloy coatings [8]. The best plating exhibited high corrosion resistance comparable with that of Zn–Ni plating, revealing promise for Zn–Fe–Mo plating as potential alternatives for Zn–Ni plating[9]. Anomalous co-deposition has been observed mostly at high current densities, whereas at low values of current density the co-deposition is normal[8], [10].

1.2 Problem Statement:

The study of Zn-Fe-Mo/W alloy coatings has become a very active field of research because of the need for environmentally friendly, corrosion-resistant, and mechanically robust coatings that are readily available. In order to produce these coatings, electrodeposition provides a versatile method, with process parameters playing a vital role. In comparison with traditional Zn-Ni alloys, Zn-Fe alloys with Mo and W have shown improved corrosion and wear resistance. To better understand these phenomena, it is necessary to further investigate the electrodeposition process and the mechanisms behind the improved properties of these alloys. The induced co-deposition of molybdenum or tungsten is, however, complicated and the side processes taking place in the aqueous plating baths (i.e. hydrogen evolution reaction) cause the structure of these coatings may contain inhomogeneities that would shorten the life time of developed coating material. Due to these limitations, the deposition process of these coatings has so far only been mastered on the micro-scale using mainly rotating disc electrodes. Therefore, the aim of this project is to develop a method of rack electrodeposition taking into account the influence of side processes, the effect of bath ageing, etc., and to transfer the electrodeposition process towards near-real conditions.

1.3 Hypothesis:

Electrodeposited zinc alloy coatings containing both an iron group metal (Fe) and a refractory metal (Mo, W) are predicted to be superior in corrosion resistance to regular zinc coatings when applied to steel substrates. Improved cathodic protection features, wherein the zinc element will corrode preferentially while imparting sacrificial protection, while the alloying elements will contribute to increasing the protective properties and overall coating lifetime.

The conditions of the electrodeposition process (current density, bath composition) can be adjusted to control the composition and microstructure of these alloy coatings, thus modifying their protective properties for specific corrosive environments.

1.4 Research question:

- Creation of own concept of the electrodeposition of zinc alloy coatings containing an iron group metal (Fe) and molybdenum (Mo) or tungsten (W).
- Finding important relationships between the composition of plating baths and plating parameters on the structure of coatings, their chemical composition and properties.
- Adjustment of the composition and working conditions of selected electroplating baths to improve the stability of the process.

- Verification of the concept of the galvanizing process on a laboratory scale. Preparation of a doctoral dissertation.

1.5 Scope of the study:

The study evaluates the performance of ternary alloy coatings of zinc-iron-molybdenum (Zn-Fe-Mo) and zinc-iron-tungsten (Zn-Fe-W). The goal is to find the optimum possible conditions through appropriate selection of process parameters such as current density and electrolyte composition. By carefully managing these factors, coatings can achieve improved deposition, corrosion resistance, surface smoothness, and appropriate metal distribution, making them suitable for mechanical and other finishing applications.

Chapter 2

2.1 Introduction

Electroplating is a common industrial technique that involves the deposition of a thin layer of a material, such as metal, on the surface of another material, such as a substrate, through the use of an electric current. Electroplating finds extensive use in various industries, such as electronics, automotive, aerospace, and consumer products, because it can improve the characteristics of the base material. It normally entails submerging the substrate in a solution containing the metal ions to deposit and, simultaneously, passing an electric current to cause the deposition. The migration of ions, which produces well-defined surfaces with a conformal thickness profile and high quality, is the fundamental nature of electroplating.

The primary advantages of electroplating are that it can precisely manage layer thickness, form high-quality morphology, well-controlled composition and homogeneity, low work-piece heat load, and low cost of production per factory product. Electroplating is not only decorative, but also has functional applications, such as enhancing corrosion resistance, conductivity, and general durability. The surface engineering of metals is a crucial phase in any manufacturing process, since it affects how a product will look and work in the end.

There are numerous processes and technologies that can be categorized as additive or subtractive, depending on the intended characteristics of the components' geometry, base material, and surface. Four main parts make up a basic electroplating setup: an anode, a cathode, the electrolytic solution, and a power supply. The design and application area will determine the type, kind, and arrangement of each of these components.

During the early part of the 1800s, a large number of scientists, such as Alessandro Volta and Michael Faraday, were actively involved in performing a series of innovative and pioneering experiments that were centered on the complex nature of electricity and the complicated behavior of electrolytes. The findings and observations obtained from these rigorous experiments formed an important platform that would eventually lead to the phenomenal development of electroplating methods and a host of other significant electrochemical processes [11]. Since its discovery in the middle of the 1800s, electroplating has been utilized for many years and has grown to be part of man's actions, either deliberately or inadvertently [12], [13], [14]. Throughout its different stages, this process is always changing and growing

in line with the times and the technological advances that shape our lives in this place and time. In recent years, research and development within the metal finishing sectors has grown rapidly due to the advent of the Fourth Industrial Revolution [15], [16] . A wide range of applications require durable metals and flexible manufacturing processes. In many industries, including automotive, aerospace, jewellery and machinery, we need durable metals and adaptable manufacturing processes [17], [18].

Economically, electroplating remains an affordable method for creating high-quality, durable components and products in industries. Electroplated items such as gold, copper and nickel are in increasing demand, although price fluctuations in these metals are a financial concern [19]. Because of fluctuating costs, industries moved to alloy-based coatings in most applications, which carry the same performance advantages with minimal amounts of costly precious metals. In addition, process innovations such as high-efficiency plating processes and resource efficiency reduce the production cost. Closed-loop wastewater treatment technology, including modified sorption materials like Akdolit-Gran, that minimize environmental impact and maximize cost savings through water recycling and minimizing hazardous waste disposal costs, is also invested in by companies [20]. The economic viability of electroplating is also facilitated by developments in automation and energy conservation technology, which allow production processes to be more efficient and to enhance overall profitability. Due to increasing demands on quality, performance, functionality, and reproducibility of the plated product, the metal finishing industry is changing substantially. Improved plating technology, along with increased variation in customer needs, has led to shifts in historic market shares in an attempt to fulfil stringent requirements on new qualities of coating and performance. Several statistics figures reveal that electroplating now dominates the world metal finishing revenues with almost 40% of the revenue market and projected to be more than US $21 billion by 2026 [21].

2.2 Application of Electroplating

Electroplating has the potential to significantly enhance the electrical conductivity of a material. The electronics sector makes extensive use of the electroplating process in the manufacture and production of numerous components such as printed circuit boards, or PCBs as they are popularly called, connectors that facilitate electrical contacts, and semiconductor devices that are crucial for today's electronic applications. Among these processes, copper electroplating stands out prominently in this sector, primarily because of its extremely high electrical conductivity, which facilitates effective transmission of electricity, and high heat

conductivity, which makes it well-suited for use in applications where heat dissipation is crucial. To be able to meet the evolving needs of contemporary electronics manufacturing, several sophisticated copper plating techniques have been developed and devised, including pulse copper plating, which optimizes the plating process, and ultrasonic copper plating, which enhances the quality and uniformity of the deposited layer [22]. The high conductivity of copper enables efficient signal transmission and reduces the possibility of electrical failure [23]. In electronics, gold and silver electroplating processes are utilised for the manufacture of contacts and interconnects, where high reliability along with low electrical resistance are essential for proper functioning. In addition, in recent times, a shift towards palladium-nickel alloys is also being observed, which is a less expensive and long-lasting substitute for gold in contact applications [24], [25].

The deposited metal layer can also improve the mechanical properties of the substrate, such as hardness and wear resistance. Chrome plating, for example, is typically done to extend the life of automobile parts by depositing a hard, abrasion-resistant surface capable of withstand abrasion and friction [26].

Electroplating is extensively utilized for improving the appearance of various products. Perhaps the most common decorative use is the careful depositing of metals such as nickel, chrome, and gold onto substrates to produce a shiny, reflective, and visually pleasing surface that adds to the overall attractiveness. For instance, scientists have explored the application of tin-ruthenium alloys, identifying them as an environmentally friendly and promising alternative to conventional nickel and palladium formulations for decorative applications[27]. Palladium-nickel alloys can also be used as decorative coatings in the electronics and jewellery industries, providing enhanced hardness and wear resistance compared to pure palladium when used as decorative coatings [25]. Gold plating is used in the manufacturing of jewellery and ornaments to impart a luxurious and elite appearance. Likewise, silver plating is utilized in cutlery and other home accessories to obtain a refined and appealing finish[28].

Electroplating plays an extremely important and central role in the ongoing development of energy storage systems, including essential components that include batteries and supercapacitors. The method given here is utilized to deposit electrocatalyst material on the surface of electrodes with the primary objective of enhancing and increasing their overall efficiency and performance. For instance, various nickel-zinc alloys and other advanced

nanostructured materials have been specially developed for use in future batteries, including state-of-the-art fuel cells at the frontline of existing technology [29], [30].

One of the most prominent and important functional applications of the electroplating process is to create and apply a protective coating that serves as a barrier to the ill effects of corrosion. By plating a layer consisting of a corrosion-resistant metal such as zinc, nickel, or chromium, the substrate is protected against environmental conditions that may lead to degradation. Electroplating extends the life of components by improving their corrosion resistance and durability. This means that parts do not need to be replaced as often, which saves money on maintenance. This is very important in fields where machines have to work in very harsh conditions, like on ships or in high-temperature environments[26], [28]. To place this in perspective, zinc electroplating has gained a lot of popularity and is being extensively utilized in the automotive and construction sectors as a means to shield steel from the corrosive effects of corrosion [31]. In addition, nickel and chrome coatings are also utilized for the sole purpose of enhancing corrosion resistance, especially in conditions that are very harsh and demanding [32].

Even though there have been major advances in technology and processing over the last four decades, industrial companies continue to face strategic challenges like corrosion protection and product durability as well as energy conservation, cost reduction, and toxic waste reduction[33].

Table 1: Application of Electroplating

Application	**Key Features**	**References**
Decorative Coatings	Shiny surfaces, ideal aesthetics, and eco-friendliness	[27], [34], [35]
Electronics Industry	Copper, gold, and silver plating for PCBs, contacts, and interconnects	[22], [36]
Energy conversion and storage	Electrocatalytic materials for batteries and supercapacitors	[29], [30]
Microsystems	Nickel, copper, and gold deposits for micro relays and valves	[37], [38]
Brush Plating	Portable and selective deposition for industrial repair and chrome alternatives	[39]

Corrosion Protection	Zinc, nickel and chrome coatings for steel protection	[31], [32], [40]

2.3 Zinc Electroplating

Zinc is recognised as the metal with the most general use in the process of electrodeposition. Over time, this particular element has been especially devoted to playing the very significant role of safeguarding ferrous materials against the deteriorating effects of corrosion. The coatings function on two important mechanisms: barrier protection, where the steel is essentially shielded from the corrosive attack of the environment, and therefore corrosion is stopped; and galvanic (or sacrificial) protection, where zinc will corrode in preference to protect the underlying steel even in the case where the coating has been scratched or damaged[41], [42]. This protective quality is so effective that it prevents the various atmospheric agents from reaching the supporting material, thereby ensuring its protection against corrosion. However, in the case of scratches or porosity, there is also an electrochemical protection. Indeed, zinc metal has an electrochemical standard potential that is very negative, and in particular more negative than iron, therefore, if rust is formed, a galvanic cell is activated in which the zinc is sacrificed by acting as an anode, restoring the metallic iron [43].

Zinc coatings are commonly used as cathodic protection because they serve as sacrificial anodes that prevent the degradation of the underlying metal surfaces. Zinc coatings have demonstrated economic success in the automotive, aerospace, and construction industries[44]. Depending on the environment, these coatings are particularly suitable for slightly alkaline and neutral environments. Despite their good performance, their performance is often limited in highly acidic or saline conditions, where the oxide layer can rapidly degrade [45], [46].

2.4 Zinc Alloy Electroplating

In the past couple of years, alloy coatings have gained a great deal of attention in various industrial applications because of their enhanced mechanical properties, improved corrosion resistance, and wear resistance compared to pure metal coatings. The inherent limitations of Zn, such as its relatively low mechanical strength to begin with, as well as its high corrosion rate in aggressive environments, have necessitated the development of ternary and quaternary alloy systems to overcome these limitations [9], [47].

Research has increasingly targeted the development of biodegradable zinc alloys with vast possibilities for use in various medical and environmental applications. Such specific alloys have controlled rates of corrosion, which renders them particularly suitable for research under the ambit of orthopedic and cardiovascular implant use [48]. Further optimisation of alloy compositions continues to be a central research area of focus. For example, the introduction of trace amounts of transition metals such as iron and nickel has been seen to provide considerable improvements in corrosion resistance in zinc coatings. The improvement does not affect their mechanical properties negatively, rendering the alloys both functional and reliable in specific applications [49], [50]. The formulation and creation of green electrolytes, along with the establishment of low-cost synthesis pathways, are of the utmost importance for the large-scale use and application of zinc alloy coatings in a wide range of applications. Numerous attempts have been directed towards substituting traditional toxic electrolytes with greener ones that are halide-free and low in toxicity [45], [51].

Zinc alloy coatings containing Fe, Co, or Ni and molybdenum or tungsten are characterised by high corrosion resistance and good mechanical properties (i.e. microhardness higher than 400 HV) when compared to the binary zinc alloy coatings with only nickel, iron, or cobalt [52], [53]. Alloying elements like Ni and Co impart greater corrosion resistance to zinc coatings by enhancing crystallographic texture and packing density[54]. Typical zinc binary alloys demonstrate improved mechanical properties, such as hardness and wear resistance, which contribute to their long-term durability[55], [56]. In automotive and industrial settings, these coatings can withstand high temperatures and harsh environments [55]. Another refractory metal, tungsten, has been investigated for its ability to enhance the wear resistance of alloy coatings and their heat stability as a result of being a refractory metal. Several studies have shown that the addition of W to Zn-based alloys is capable of improving their mechanical properties, such as hardness and wear resistance, while maintaining their corrosion resistance at the same level [57], [58].

Electrodepositions of zinc and zinc alloy are extensively used in many industries and have distinctive advantages over other finishing processes. In practice, Zn-Ni and Zn-Co coatings require harmful metal salts with Ni(II) and Co(II) ions as compared to Zn-Fe coatings with iron(II) sulphate salt, which is less harmful. Zn–Ni alloys are one of the most researched zinc-based coatings because of their high corrosion resistance and mechanical properties. It was found that Zn–Ni coatings containing 15–18% nickel have better protection than pure zinc coatings. This is explained by the formation of γ-Ni_5Zn_{21} and δ-Ni_3Zn_{22} phases [59]. Also,

demonstrated that the γ-Ni_5Zn_{21} phase in Zn-Ni coatings inhibits red rust development by forming a dense oxide layer, exhibiting better performance than pure zinc under salt-spray tests (>1,000 hours). These coatings are used in preference in marine and aerospace applications. Challenges involve hydrogen embrittlement on electroplating, requiring the addition of brighteners and stress relievers [60]. The Zn-Co alloy is particularly useful for coating applications that require a high level of adhesion and wear resistance [61]. Manganese alloying in zinc coatings is aimed at reinforcing wear resistance along with corrosion protection. P P Chung et al. [62] and R Munz et al. [63] noted electrodeposition of Zn-Mn alloy coatings from ionic liquid electrolytes and added that coatings possessed higher hardness and corrosion protection than pure zinc coatings. Adding magnesium to zinc coatings has been investigated to enhance biocompatibility and corrosion resistance for biomedical use. Research on Mg-Zn alloys with chitosan-based coatings has exhibited uniform coatings that effectively enhance corrosion resistance in simulated body fluids [64]. Additionally, Zn-loaded montmorillonite coatings on biodegradable Mg alloys have shown enhanced corrosion resistance, biocompatibility, and antibacterial activity, and have potential for use in orthopedic applications [65]. A zinc-iron alloy coating (Zn-Fe) has gained significant attention due to its superior corrosion resistance and mechanical properties. Many extensive research works have been reported on the deposition mechanism of Zn-Fe group metal alloys [66], [67], [68]. It has been concluded that deposition of zinc with iron metal (Zn-Fe) alloy coating shows good resistance to corrosion as compared to single metal deposition [2], [69].

Another possibility of modifying the properties of binary zinc alloy coatings is to introduce a third alloying component characterized by high corrosion resistance and better mechanical properties compared to zinc and an iron group metal (Zn-Fe). The combination of Mo or W in Zn-based alloys is expected to synergistically enhance both the corrosion and wear-resistant properties of the coating. It is known from the literature on the subject that if introduced into a nickel coating, molybdenum improves its utility properties, such as hardness, wear resistance, and corrosion resistance [3]. There has been some speculation that the iron-group metals may act as catalysts in the formation of intermediate products in the process of induced co-deposition according to the mechanism [70], [71], [72]. Therefore, it is more convenient to use a Zn-Fe alloy coating in addition to a molybdenum or Zn-Fe-Mo ternary alloy coating. Much basic research has been found investigating the electrochemical deposition process of zinc, iron and molybdenum (Zn-Fe-Mo) alloy coating [4], [8], [73], [74]. It has been proved that the influence of Mo concentration in Zn-Fe alloy coating has more corrosion resistance

potential as compared to Zn-Fe alloy coating [4]. Much higher microhardness resulted when molybdenum was introduced into a two-component system Zn-Ni and Zn-Co [5], [6].

Metal Mo is difficult to electrodeposit from aqueous solutions because of its high oxidation state; however, metallic Mo can be electrodeposited under co-deposition with iron-group elements, known as the principle of induced co-deposition.[7] Extensive research has been conducted on the incorporation of tungsten (W), due to its exceptional properties such as high melting point, superior wear resistance, remarkable hardness, and excellent anti-friction characteristics [75]. Studies have demonstrated that the introduction of tungsten into ternary Ni-Fe-W alloys refines the grain structure, improves microstructural uniformity, and significantly increases the surface hardness of composite coatings [75]. These advantages have spurred interest in the combination of Zn-Fe alloy coatings with tungsten to form ternary Zn-Fe-W systems, which offer enhanced performance over binary alloys. Consequently, researchers have focused on exploring the electrochemical deposition processes involved in synthesizing zinc, iron, and Zn-Fe-W alloy coatings, with foundational studies providing critical insights into their fabrication and properties [76].

Although the impact of various parameters on alloy coating deposition processes has been extensively analyzed, challenges persist in electrodepositing metallic tungsten from aqueous solutions. This difficulty arises because tungsten predominantly exists in aqueous media as oxyanion species, including paratungstates $[HW_6O_{21}]^{5-}$, metatungstates $[H_2W_{21}O_{40}]^{6-}$, and tungstate $[WO_4{}^{2-}]$ ions. However, research shows that iron-group elements enable tungsten co-deposition through induced co-deposition mechanisms, facilitating its incorporation into alloy coatings [77]. Notably, anomalous co-deposition (where less noble metals deposit preferentially) dominates at high current densities, while normal co-deposition behavior occurs at lower current densities [8], [10]. Additionally, studies reveal that increasing the pH of the electrolyte enhances deposition rates and elevates the iron and tungsten content in the resulting coatings [75]

2.5 Factors Affecting Electroplating Process

In the development of coatings, factors such as current density, pH, temperature, and bath composition play an important role in the specification of their microstructure, phase composition, and surface properties. It is well-known that the growth of metastable crystal structures is caused by high current densities and the formation of the η phase in Zn-Fe coatings[74], [78]. A number of factors, such as pH and current density, play an important role

in determining the amount of Mo in a Zn-Co-Mo coating, and consequently the corrosion resistance of this coating [74], [78]. In alloy coatings, the composition of the plating bath is a basic deposition parameter since it affects the deposition process and decides the ionic species of metals [79]. There is, however, a specific molar concentration ratio that can result in a Ni mass fraction of about 13%, which is optimal for corrosion resistance[80]. It is important to maintain a concentration of Zn^{2+} and Ni^{2+} between 0.17 and 0.40 mol/L to achieve the desired coating characteristics for the coating[80]. Deposition potential is the determining factor for the electrodeposition process as well as composition and surface properties of Zn-Ni-Mn alloy coatings. In normal co-deposition, there is the potential range of −0.5 to −1.0 V, and more cathodic potentials lead to anomalous co-deposition[81].

The stability of the electrolyte solution throughout electrodeposition is crucial in playing a significant role in the overall coating process. Many studies utilized the citrate-sulphate bath for alloy coatings due to its ability to produce metal complexes [4], [74], [79], [82].As a result, it improves the solubility of the metals. In addition, citrate acts as a buffering agent since it is a weak polyprotic acid [83]. The induced co-deposition of nickel and molybdenum by citrate has also been reported to be beneficial [84]. Similar to citrate, ammonia is added to these electrolytes, which leads to the creation of metal complexes in the presence of ammonia [85]. Sodium sulphate and ammonium sulphate have a significant effect on the properties and quality of deposit metals, such as grain refinement. They can be used to change the conductivity, solubility, buffering capacity, voltage stability, throwing power, and stress relief of electrolytes. This study also finds important links between the two different galvanic baths, $(NH_4)_2SO_4$ and Na_2SO_4.

2.6 Corrosion

Corrosion has also been commonly referred to as "metallurgy in reverse," a term that rightly describes the process by which metals revert to their most stable chemical state. By reacting with the surrounding environment, corrosion transforms metals into a range of compounds, such as oxides or sulfides, through complex electrochemical processes[86], [87]. The chemical processes take place through complex oxidation and reduction processes, which gradually undermine the structural integrity of metallic materials over time[88]. Preventive strategies involve the application of corrosion inhibitors, protective coatings, and the formulation of self-healing rust films that can shield underlying metals [89], [90]. Furthermore, there is a necessity for sophisticated surface characterization methods to enhance the understanding of the initiation stages of corrosion and the efficiency of inhibitors [90].

There are several ways to protect steel from corrosion; one of them is by employing zinc coatings as a cathodic protection, where zinc acts as sacrificial anode, preferentially corroding instead of the steel over time. A zinc coating is particularly effective in environments where the zinc coating forms a stable oxide layer, which is capable of inhibiting the corrosion of the zinc underneath [45], [46]. The formation of corrosion products also influences the effectiveness of zinc coatings in corrosion resistance. In neutral environments, zinc responds to produce zinc hydroxide, which can further react with carbon dioxide, leading to the formation of a protective layer of zinc carbonate. In more aggressive environments, like those containing chlorides, the resulting corrosion products can include zinc chloride and zinc hydroxy chloride, which can provide additional protection[91], [92].

The corrosion behavior of zinc alloy coatings is mainly controlled by the phenomenon of selective dissolution, as well as by the specific alloying elements present in the coating composition. For example, in Zn-Al coatings, aluminium plays a significant role because it exists as a cathode and, in the process, catalyses the dissolution process of zinc [91].This process facilitates and promotes the formation of a protective layer composed of corrosion products that are capable of inhibiting further degradation. However, it must be noted that when selective dissolution occurs in excess, it contributes to the generation of corrosion cracks. The cracks are unwanted in coatings; they ultimately result in a reduction of the overall corrosion resistance of the coating system[91], [93]. The corrosion behavior of different Zn-based coatings is listed in Table 2.

Table 2. Corrosion rate of different types of Zinc coatings

Coating type	**Composition**	**EIS finding in NaCl Sol.**	**Key features**	**Citation**
Pure Zinc Coating	100% Zn	Initial $R_p \approx 3000\ \Omega\cdot cm^2$ (after 1 h immersion); R_p drops to ~$50\ \Omega\cdot cm^2$ after extended immersion (e.g. 48 days)	Rapid decrease in impedance; formation of non-protective $ZnO/Zn(OH)_2$ films leading to early substrate attack	[94]
Zn-Co Coating	Zn with ~0.5–1.5 wt.% Co	Rct ≈ 3× higher than pure Zn. Lifetime 3× longer; R_p values higher than for pure	Co enrichment reduces anodic dissolution; forms	[95]

		Zn; reported initial values may approach those of Zn–Ni; more stable impedance over time	dense $Zn(OH)_2/Co_3O_4$ barrier layers	
Zn-Mg Coating	5.1 wt.% to 15.5 wt.%, Mg	charge transfer resistance increased significantly with higher Mg content. from 162.1 Ω·cm² to 558.8 Ω·cm² as Mg content rose from 5.1 wt.% to 15.5 wt.%	Precipitation of protective Mg-rich oxides/hydroxides, which reinforce the protective corrosion	[96]
Zn-Fe Coating	Zn with ~0.5 wt.% Fe	R_p sometimes similar to pure Zn or modestly higher; results can be variable depending on Fe content	Fe-rich phases improve adhesion but reduce sacrificial protection over time.	[97]
Zn-Ni Coating	86 wt.% Zn / 14 wt.% Ni	Initial R_p typically in the range 4000-6000 Ω·cm²; slower decline with immersion compared to pure Zn	Ni improves the formation of a stable passive film, enhancing the barrier effect and slowing charge transfer	[98], [99]
Zn-Mo Coating	Zn with ~0.5 wt.% Mo	Moderate increase in initial R_p compared to pure Zn; improved stability during immersion	Superior corrosion resistance due to MoO_3 passivation; EIS impedance 3x higher than pure Zn.	[100]
Zn-Al-Mg Coatings	Zn + ~2 wt.% Al + ~1 wt.% Mg	Initial R_p values around 6000 Ω·cm²;after extended immersion (e.g., 48 days) R_p remains high (≈2700 Ω·cm²)	The alloying elements (Al and Mg) promote the formation of compact corrosion products (e.g. simonkolleite, Zn–Al	[94], [101]

			oxides) that provide a durable barrier	
Zn-Fe-Mo Coating	Zn with small additions of Fe and Mo	Exhibits higher and more stable R_p than pure Zn; the impedance remains elevated over longer immersion periods	The synergistic effect of Fe and Mo aids in the formation of a protective film that slows charge transfer and improves long-term corrosion resistance	[73]
Zn-Ni-Sn Coating	Zn–Ni alloy with minor Sn addition (~Zn–Ni–Sn)	Typically shows an increase in R_p compared to standard Zn–Ni coatings; better impedance stability during immersion	Compact morphology, Effective sacrificial corrosion protection	[102]
Zn-Ni-Mo Coating	Zn–Ni alloy with Mo addition	The reports indicate sustained high R_p values throughout the immersion testing, demonstrating excellent barrier characteristics	The combination of Ni and Mo promotes the formation of a dense, protective passive layer that resists degradation over time	[99]

Chapter 3

Materials and Methods

3.1 Materials

3.1.1 Material selection:

A number of practical and technical reasons lead to steel being a popular choice for testing electrodeposited coatings, including: Steel possesses very good electrical conductivity and is thus a very good substrate for electrodeposition. Having a uniform and conducting surface is important in ensuring that the electroplated layer forms and adheres in a uniform mode, a factor which plays a pivotal role in determining important characteristics such as adhesion and thickness. In this regard, S235JR carbon steel is used as a base material for coatings.

Most industrial components, such as fasteners, automotive parts, and construction materials, are commonly produced from steel as a starting material. Conducting tests on coatings deposited over steel substrates provides performance data that is based on real working conditions, and thus guarantees that such test data can easily be implemented in day-to-day practical application. A major majority of industry standards, like widely used specifications offered by ASTM and ISO, are particularly designed with steel substrates as the primary focus. The application of steel in testing procedures not only complies with such pre-established and known procedures, but also plays a crucial role in providing reliable and consistent quality assurance processes while making effective comparison feasible across various coatings. Steel is commonly recognized for providing a tough and reliable mechanical baseline that is needed in various applications. Its superior characteristics, such as strength, ductility, and thermal stability, enable the performance of rigorous testing procedures such as bend tests, adhesion tests, and wear tests without causing any serious interference due to deformation of the substrate itself. This particular technique is extremely effective in delaminating the coating and completely testing its performance in a highly detailed manner. The steel substrates are easily sourced and can effectively be prepared using standardized cleaning and pretreatment processes that are used commonly. These highly controlled processes are very important for reducing any potential variables that could affect the outcome and making test results much more reproducible across different batches and other experimental parameters.

In order to precisely define the elemental composition and phase structure of the Zn-Fe-Mo/W alloy coatings, high-purity copper discs of M1E grade were chosen as the substrate material for Scanning Electron Microscopy (SEM), Energy Dispersive X-ray Spectroscopy (EDXS), and X-ray Diffraction (XRD) investigations.

Copper was chosen to eliminate substrate material interferences during elemental and structural analyses. Since copper is not an iron-containing material, copper substrate material utilization ensures that iron in the coating originates solely from the deposited Zn-Fe-Mo/ Zn-Fe-W coating, and not from substrate diffusion or signal overlap. This choice is especially essential for EDXS, in which substrate signals can penetrate thin coatings and mislead compositional measurement.

In addition, the chemical stability and elevated electrical conductivity of M1E-grade copper provide stable and reproducible deposition conditions on the electrodes, allowing homogeneous growth of the coatings. The copper substrate surface, also smooth and homogeneous, provides high-resolution SEM observation, allowing for higher clarity in surface morphology studies.

3.1.2 Metal Treatment:

Before the electrodeposition process, the metal discs were carefully prepared to have a smooth and clean surface, as this is necessary for optimal adhesion of the coating. The surface preparation process started with mechanical polishing, which involved the use of 600 and 1200-grit abrasive papers. Initially, the 600-grit paper was used to extensively eliminate surface oxides, scratches, and other forms of imperfections that may have been present. Subsequently, the smoother 1200-grit paper was used to obtain a much finer and more uniform finish on the metal discs. Once the polishing process was completed, the disks underwent a thorough rinsing in acetone that served the critical purpose of removing any residual oils, greasy residue, or organic impurities present that would interfere with or impede the process of electrodeposition. To significantly increase the effectiveness of the cleaning process, the rinsing with acetone was conducted in an ultrasonic bath, a procedure well acclaimed for possessing high cleaning capacity. The ultrasonic vibrations developed in the bath caused the formation of many small cavitation bubbles in the acetone solution, effectively dislodging any remaining particles or residues from the polishing process. This not only ensured that the surfaces of the discs were adequately cleaned but also that even the most stubborn debris entrenched in micro-crevices was thoroughly removed, leaving behind an exceedingly clean surface for subsequent operations. The correct and entire surface preparation was absolutely

vital in order to have appropriate adhesion and also even deposition taking place throughout the whole process of electrodeposition.

Chemical cleaning and activation treatment were also conducted for the metal discs as a preliminary treatment in order to raise their surface reactivity and purity prior to undergoing electrodeposition process. The preliminary stage consisted of alkaline cleaning in SurTec 154 solution at 60 °C. The alkaline cleaner successfully removed all remaining organic substances and oils together with particulates that survived mechanical polishing and acetone cleaning. The samples received a complete deionized water rinse to eliminate all cleaning agents after their thorough cleaning process. The activation process consisted of placing the cleaned surfaces in a 10 wt % sulfuric acid (H_2SO_4) solution at room temperature for 10 seconds. The acid treatment removed surface oxides and passive layers, which led to increased reactivity and better electrodeposition adhesion. The samples received multiple deionized water rinses to eliminate all acid residue after activation. These procedures together created an active surface which was essential for obtaining uniform and adherent electrodeposit formation. container.

3.1.3 Electrolyte Bath Preparation:

The Zn-Fe-Mo/Zn-Fe-W alloy coatings were electrodeposited from two different citrate-sulphate electrolytic baths, with their compositions detailed in Table 3. All solutions were prepared using analytical-grade reagents and deionized water to ensure high purity and reduce the risk of contamination. The pH of each bath was carefully adjusted to 5.7 ± 0.05, in accordance with procedures outlined in previous studies [4], [74]. For sodium-based baths, pH adjustments were conducted using diluted sulfuric acid (H_2SO_4) and sodium hydroxide (NaOH). In the case of the ammonium sulphate-based bath, a 35% ammonia solution was used for pH adjustments.

Table 3. Plating bath compositions connected with the labelling of the samples

Types of Galvanic Bath	**$ZnSO_4$ · $7H_2O$**	**$Na_3C_6H_5O_7$** (trisodium citrate)	**Na_2SO_4**	**$(NH_4)_2SO_4$**	**$FeSO_4$ ·$7H_2O$**	**Na_2MoO_4 · $2H_2O$**	**Na_2WO_4 · $2H_2O$**
Zn-Fe-Mo_NaCit_Na_2SO_4	0.4M	0.4M	0.2M	---	0.4M	0.01M	---
Zn-Fe-Mo_NaCit_$(NH_4)_2SO_4$	0.4M	0.4M	---	0.2M	0.4M	0.01M	---
Zn-Fe-W_NaCit_Na_2SO_4	0.4M	0.4M	0.2M	---	0.4M	---	0.01M
Zn-Fe-W_NaCit_$(NH_4)_2SO_4$	0.4M	0.4M	---	0.2M	0.4M	---	0.01M

3.1.4 Electrodeposition:

Electrochemical experiments were carried out in a 100 cm^3 glass cell kept at a temperature of 25 ± 1°C. All depositions were performed under galvanostatic control in anode current (j_a) and cathode current density (j_c) set at 10, 15, 20 and 25 mA cm^{-2}, respectively. The substrate was positioned parallel to two PLATINODE® platinised titanium anodes (supplied by Umicore) of 70 mm × 30 mm dimensions. This arrangement ensured an excellent distribution of current, thus improving coating uniformity over the face of the cathode surface.

In an attempt to preserve homogeneity in the electrolyte and prevent localized ion depletion near the cathode, mechanical stirring was imposed during the entire deposition process, utilizing an IKA HS-4 magnetic stirrer. The deposition time was estimated based on the current efficiency of the system, which varied based on the composition of the bath and current density utilized. The efficiencies of the ammonium baths varied between 25% and 40%, whereas those of the sodium baths reached much higher efficiencies in the range 55% to 72%. These efficiencies significantly altered the deposition times necessary to deposit a coating thickness of ca. 8 µm (adopted arbitrarily, taking into account the time span). The coatings' thickness was measured by means of a Fischer FMP40 magnetic induction thickness gauge, and compared where possible with cross sections of the coatings. At optimal pH 5.7, the sodium bath presented current efficiency as high as 60%, in good correspondence to reported data in current literature[74]. The increased current efficiency positively boosted the coatings' density, adhesion, and homogeneity, being in this case appropriate for subsequent structure and electrochemical characterization studies.

3.2 Research Methodology

3.2.1 Electrochemical Characterization via Cyclic Voltammetry (CV):

Cyclic voltammetry (CV) was used for the investigation of the electrochemical behavior of citrate-sulphate baths for the electro deposits of the Zn-Fe-Mo and Zn-Fe-W alloys. The experiments were carried out for a standard three-electrode electrochemical cell, a typical set-up that ensures effective potential control and precise current response measurement during the electrochemical sweeps.

With this set up, the working electrode was a platinum (Pt) tip of diameter 3 mm corresponding to a geometric surface area of 0.071 cm^2. Platinum tip had been used because platinum electrochemically acts as an inert substance and provides very good conductivity, so obtained voltammograms were characteristic of inherent electrochemical character of the bath

constituents rather than the surface reaction onto the electrode. The platinum working electrode before each experiment was cleaned by an ultrasonic bath using acetone to remove any impurities or adsorbed organic species present, which would otherwise affect the reproducibility and the accuracy of the determinations.

The platinum wire used as a counter electrode offered a high and inert surface area for the facilitation of current flow through the circuit without involvement in the desired electrochemical reactions. The double junction silver/silver chloride (Ag|AgCl) double junction electrode was used as the reference electrode because it increased stability, and it reduced the contamination of the electrolyte from the reference compartment. The use of a double junction also decreases the potential for possible drift and junction potential, providing more accurate potential readings during the experiment.

Cyclic voltammetry was carried out using a 100 cm^3 bath of the same electrolyte undergoing electrodeposition. During experiment, remained stirring continuously at a speed of 800 revolutions per minute (rpm) by a magnetic stirrer. This helped distribute the ionic species homogeneously close to the surface of the electrode and reduced diffusion layer accumulation, thereby sustaining more regulated mass transport conditions. All the experiments were carried out at the same temperature, 25 °C, with the temperature regulated to prevent temperature-based variations in the kinetics of the reactions and conductivity of the electrolytes.

The first possible scan was begun from the open circuit potential (E_{OC}), which corresponds, naturally, to the established equilibrium potential of the working electrode when placed into the supporting electrolyte solution, without any pre-applied bias. The potential was subsequently made negative in the direction up to −1.4 V relative to Ag|AgCl, a value chosen from preliminary experiments as a condition for the onset of the specified cathodic reactions of interest for the metal ion reducing process. The scan was subsequently reversed into the positive direction up to +0.1 V relative to Ag|AgCl, in order to detect potential anodic activities, for instance, the deposits stripping of the metal or the bath component oxidation. The entire scan was carried out at a moderate sweep rate of 5 mV s^{-1}, a rate well adapted since it provides a fair compromise between the signal resolution and the perturbing effects due to the capacitive current, and which allows the investigation of slow electrochemical processes and the characterization of redox reactions.

The procedure employed for the CV test yielded significant insights into the redox behavior of metal ions present in the plating bath, including the reduction potentials of distinct species

and potential interactions between Zn^{2+}, Fe^{2+}, and Mo/W species within the electrolyte. The data collected were essential for refining the electrodeposition parameters and understanding the fundamental electrochemical mechanisms involved in the formation of Zn-Fe-Mo and Zn-Fe-W alloy coatings.

3.2.2 UV-Vis spectroscopy:

Spectroscopic analysis was conducted with a GENESYS 10S UV-vis spectrophotometer fitted with 1 cm pathlength quartz cuvettes. The following were the measurement conditions. Wavelength range: 200–1100 nm. Slit width: 1 nm. Scan speed: fast setting. Blank baseline: blank electrolyte solution containing only sodium citrate and sodium sulphate, made up at the same concentrations as in the working bath, see Table 3 on page 18. Each sample was scanned right after it was collected and spectra were stored in both raw and processed formats (CSV files of wavelength vs. absorbance).

At the beginning of every deposition run, the electrolyte was described by measurement of pH, temperature, and by the acquisition of the initial UV–Vis spectrum (t = 0). Electrodeposition was started at a constant current Operating parameters such as electrode area 70 mm × 30 mm dimensions, current density 20 mA cm^{-2}, and total deposition time was noted.

To monitor changes in electrolyte composition during deposition, aliquots (2–5 mL) were withdrawn from the bath every 10 minutes. The sampling continued until the end of the deposition.

3.2.3 Surface Morphology and Chemical Composition Analysis:

The surface morphology and semi-quantitative chemical composition of the Zn-Fe-Mo or Zn-Fe-W alloy coatings were analyzed using scanning electron microscopy (SEM) combined with energy-dispersive X-ray spectroscopy (EDS). These two complementary techniques provided detailed images of surface features and allowed for elemental analysis of the coated layers.

The morphological analysis was conducted with a Quanta 250 (FEI) scanning electron microscope, which includes a built-in X-ray microanalyzer for EDS measurements. Prior to analysis, the samples were cleaned and, if necessary, mounted on conductive carbon tape to ensure proper electrical contact and minimize surface charging during imaging.

SEM analysis was carried out with both secondary electron (SE) and backscattered electron (BSE) modes. SE imaging was used mostly to investigate the fine surface topography and microstructures of the coatings. With this method, high resolution images are obtained through

the detection of low-energy secondary electrons emitted from surface coatings. BSE imaging, on the other hand, was utilized as a means of checking compositional contrast. Backscattered electrons respond to variations in atomic number and therefore can distinguish regions of differing elemental composition or density of the coating. The microscope used high vacuum conditions of around 10^{-4} Pa as a requirement for the stability of the electron beam and high resolution imaging. The accelerating voltage used depended on the specific requirement of the analysis involved: 15 kV used for surface morphology analysis (in SE mode), while it minimizes beam penetration and helps retain surface detail; and 25 kV used for BSE imaging and energy-dispersive spectroscopy (EDS) analysis in order to achieve sufficient beam energy with deeper interaction volumes and effective generation of X-rays from heavier components. For chemical composition analysis, energy-dispersive X-ray spectroscopy (EDS) analysis was carried out with an EDAX microanalyzer with scanning electron microscope (SEM) integration. EDS enables semi-quantitative assessment of the elemental composition of coatings through the detection of characteristic X-rays emitted from a specimen as a result of interaction with the incoming electron beam. The measured data were corrected employing standard ZAF correction codes, compensating through atomic number effects of absorption and effects of fluorescence in order to ascertain the relative weight percent of the zinc, iron, and molybdenum, or tungsten, and others.

The combination of SEM and EDS facilitated detailed characterization of the coatings, providing high-resolution images of their morphology and accurate data on elemental distribution. These measurements were essential for correlating coating morphology, uniformity, and compositional homogeneity with electrodeposition conditions, which are crucial to define the functional properties of the Zn-Fe-Mo and Zn-Fe-W alloy coatings.

3.2.4 Surface Topography Characterization via Stylus Profilometry:

The surface topography and properties of the Zn-Fe-Mo and Zn-Fe-W alloy coatings at a micro-scale were determined from contact profilometry. With this method, a quantitative value of surface profile features and roughness can be obtained and are of fundamental significance to the knowledge of the coatings' functional properties, i.e., corrosion protection, wear resistance, and adhesion.

Surface profiling has also been done with a Bruker DektakXT stylus profiler, a high-accuracy device used to measure changes in surface height at a fixed scanning distance. Data acquisition involved a diamond-coated stylus that moved across the surface of the coating under controlled

conditions. With a resolution and wear resistance-balanced radius of the stylus tip of 2.5 µm, surface features at a micro-scale could be resolved without damaging the coating.

To realize a representative surface analysis, a number of line scans were carried out for each of the samples. These scans were parallel to the mechanical scratches deposited on the steel substrate and were designed to limit interference and isolate specifically the surface features of the films deposited through electrochemistry. Each of the line scans covered a distance of 2000 µm, sufficient to yield a statistically relevant area through which data regarding the coated surface could be obtained. During the process of measurement, the stylus was driven at a constant speed of 1000 µm/min under a vertical load of 3 mg onto the surface. Such a low loading condition suppressed any possible deformation of the surface while ensuring stable contact of the stylus with the coating. Along the path of the stylus traversing the surface, vertical displacement changes were measured with high sensitivity and consequently used to produce a surface profile that accurately portrays the roughness and texture of the sample.

These profilometric data were then utilized subsequently to estimate roughness parameters, i.e., Ra (arithmetical mean roughness). Of crucial significance while correlating the surface finish of coatings with the parameters of electrodeposition and assessing their appropriateness for practical applications, where surface integrity becomes a paramount consideration.

3.2.5 Microstructural Analysis via FIB/SEM Cross-Sectioning:

To study the internal microstructure of Zn-Fe-Mo and Zn-Fe-W alloy coatings with high spatial resolution and precision, we employed Focused Ion Beam/Scanning Electron Microscopy (FIB/SEM). This advanced technique allows site-specific cross-sectional preparation and provides in-depth examination of coating thickness, layering, interface quality, and structural features that are not visible through surface imaging alone.

Cross-sectional analysis was carried out using an FEI Helios NanoLab™ 600i dual-beam microscope system comprised of a high-resolution field-emission scanning electron microscope (FE-SEM) and a gallium (Ga^+) focused ion beam (FIB). This system enables the in situ preparation of a cross-section while enabling real-time observation of the same, making it especially suitable for investigating ultrathin films like Zn-Fe-Mo or Zn-Fe-W coatings' microstructural features. To minimize surface damage of the coating from exposure to the ion beam directly, an initial Pt protective coating was deposited onto the region of interest before carrying out the FIB milling process. A Pt protective layer of dimensions of 10 µm × 1 µm (rectangle size) was created through the sequential use of both Focused Electron Beam Induced Deposition (FEBID) and Focused Ion Beam Induced Deposition (FIBID). First used

were the facilities of FEBID to deposit a low-damage Pt cap of an ultra-thin thickness. Then, the use of FIBID helped to accelerate the build-up of the Pt protective coating. This two-step process ensures that the surface gets preserved while sufficient shielding is provided during the more aggressive process of ion milling. Ion etching was used once the protective Pt cap was deposited to dig out material from the region of interest. This was done with a Ga^+ ion beam utilizing an accelerating voltage of 30 kV, typical of successful milling with a FIB. To optimize the quality of the end surface and prevent redeposition and artefacts caused by the ion beam, the cross-section was polished continuously. This entailed reducing the current of the ion beam slowly until a minimum polishing current of 80 pA. This aspect is vital to obtain a flat and clean surface of the cross-section suitable for high-resolution imaging and accurate interpretation of the microstructures. Once the cross-section was prepared and buffed, imaging with the microscope's immersion mode was carried out. Increase resolution and signal-to-noise ratio through immersion of the sampling region in a magnetic circuit. The imaging used a low accelerating voltage of 2 kV, reducing the electron beam's penetration depth and increasing surface sensitivity. It offers high detail contrast and resolution of the microstructural features of interest, i.e., the grain boundaries, interlayer interfaces, and porosity.

The utilization of the FIB/SEM method in this study facilitated the accurate characterization of both the coating architecture and the interface connecting the Zn-Fe-Mo and Zn-Fe-W coatings to the steel substrate. Consequently, this offered significant understanding regarding the uniformity of deposition, management of thickness, and the presence of any possible imperfections within the coating structure.

3.2.6 STEM Analysis and Structure Characterization:

Scanning Transmission Electron Microscopy (STEM) was performed with the aim of obtaining a complete nanoscale analysis using a ThermoFisher Scientific Talos F200i instrument at an accelerating voltage of 200 kV. Specialized STEM assessment thin lamellae were carefully prepared from Zn-Fe-Mo coatings using an FEI Helios NanoLab™ 600i FIB/SEM system. A specially designed method of lamella preparation with specific interest point observation from prior SEM analysis was used as a method to optimize high-resolution transmission imaging.

STEM imaging used a high-angle annular dark field (HAADF) detector, allowing for Z-contrast imaging. In this method, atoms of high atomic numbers are visualized as brighter because of the high electron scattering effect. The HAADF images were subjected to digital

inversion and generated a contrast similar to that of bright-field imaging, thus further assisting the analysis of structural features such as grain boundaries and phase distribution. Crystallographic data were inferred from Selected Area Electron Diffraction (SAED) as per standard procedures of Transmission Electron Microscopy (TEM). SAED patterns were obtained using a CETA-M electron camera from ThermoFisher Scientific and used to identify crystalline phases and ascertain local ordering of the coating matrix. In addition to imaging methods, Energy Dispersive X-ray Spectroscopy (EDS) mapping was conducted under the Scanning Transmission Electron Microscopy (STEM) mode with a Bruker Xflash30 EDS detector. Using this method, spatially resolved elemental analysis of the lamella could be obtained, which helped to verify elemental distribution verification, phase segregation examination, and assessment of the homogeneity of Zn-Fe-Mo alloy coatings' at the nanoscale. Integration of Focused Ion Beam and Scanning Electron Microscopy (FIB/SEM) with Scanning Transmission Electron Microscopy (STEM) enabled a comprehensive characterization of the coatings, ranging from morphological evaluation at the micrometre scale through structural and compositional data at the atomic level. These methods significantly enhanced material performance and quality of deposition.

3.2.7 Phase Composition Analysis via X-ray Diffraction (XRD):

To investigate the phase composition and crystalline nature of Zn-Fe-Mo and Zn-Fe-W alloy coatings, we conducted an X-ray diffraction (XRD) analysis. It is a valuable method engaged in the recognition of crystalline phases, the assessment of crystallite size measurements, as well as an estimation of the structural ordering degree of deposited coatings.

X-ray diffraction (XRD) patterns were captured using a Siemens D 5000 diffractometer equipped with a CuKα radiation source (λ = 1.5406 Å). This device is commonly used for structural studies of metal and alloy systems because of its suitable wavelength and effective penetration capabilities. All measurements were carried out at ambient temperature, ensuring that the phase composition of the as-deposited state of the coatings remains without any heat alteration. The scanning angle was set from the zone of 10° to 85° of the 2θ region that covers common diffraction angles associated with metallic phases, solid solutions, intermetallic compounds and oxide species formed during or after the electrodeposition process. With this wide scanning angle, successful identification of both major and minor phases contained within the coating becomes easier. These diffraction data obtained were analyzed using the PDF-5+ 2024 database from the International Centre for Diffraction Data (ICDD). This extensive and up-to-date database provides standard reference patterns that facilitate phase

identification from the evaluation of peak positions and intensities. These diffraction peaks were compared with established crystalline structures to identify the phase composition. Special attention has been directed at ascertaining any possible binary and ternary intermetallic phases involving zinc, iron, molybdenum, and tungsten, and any possible oxidized species that could have resulted from exposure of the deposited coatings to air or moisture, or due to partial only reduction during electroplating.

These X-ray diffraction (XRD) patterns provided valuable data about the crystallographic structure of Zn-Fe-Mo and Zn-Fe-W coatings, indicating the presence of either amorphous or nanocrystalline structures, certain preferred crystallographic orientations (texture), and the formation of solid solutions. These are of much relevance while attempting at correlating the above structural features with the coatings' properties such as hardness, corrosion resistance, and their magneto behavior.

3.2.8 Electrochemical Corrosion Testing (DC and AC Polarization Methods):

To determine the corrosion resistance of Zn-Fe-Mo and Zn-Fe-W alloy coatings, both DC and AC electrochemical techniques were applied. All the experiments were conducted employing a Gamry Reference 3000 potentiostat, a very sensitive device that can perform both potentiodynamic and impedance tests. The corrosion studies utilized a 0.5 M solution of NaCl as the corrosive medium and were selected as a simulated saline environment. Before carrying out the tests, the electrolyte was carefully deaerated through argon gas purging, which consequently eliminated the effect of dissolved oxygen-corrosion behavior.

The experimental setup consisted of a three-electrode electrochemical cell, which included:

- A silver/silver chloride (Ag|AgCl) reference electrode (RL-100, Hydromet),
- A platinum plate as the counter electrode, and
- A coated steel sample serving as the working electrode, with a defined geometric area of 0.5 cm^2 immersed in the solution.

Linear Polarization Resistance (LPR) tests were utilized as a means of assessing major corrosion parameters, i.e., polarization resistance (R_p), corrosion current density (i_{corr}), and corrosion potential (E_{corr}) for a period of 24 hours of immersion. LPR scans were conducted under a restricted potential band of ±15 mV with reference to the open circuit potential (E_{OC}) at a scan rate of 0.125 mV/s, therefore ensuring minimal disruption of the system while accurately assessing sensitive corrosion processes. Following an exposure of 24 hours, the polarization plots were extracted under a potential window of −0.1 V to +0.1 V with reference

to E_{OC} using a scan rate of 0.167 mV/s. Such a measure facilitated a more reliable assessment of the electrochemical action and passivation behavior of the coatings. In addition to DC methods, electrochemical impedance spectroscopy (EIS) was also conducted with a view of assessing the barrier as well as the charge transfer resistance of the coating. EIS measurements were carried out at the end of constant immersion (E_{OC}) at an exposure of 24 hours using a sinus voltage stimulus of a root mean square amplitude of 10 mV. The frequency spectrum ranged from a high of 100 kHz through a low of 10 mHz with a resolution of 10 points per decade. Such a configuration facilitated a complex modelling of a high-frequency response (i.e., referring toward the behavior of coatings)and a low-frequency response (i.e., referring toward the kinetics of electrochemical reactions).

To eliminate electromagnetic interference, all measurements were conducted within a Faraday cage, ensuring high-precision data collection. The resulting impedance spectra were analyzed and fitted using Gamry Echem analyst software. Appropriate equivalent electrical circuit models were applied to derive meaningful corrosion-related parameters.

Chapter 4

Results and Discussion

4.1 The effect of plating bath composition on the cyclic voltammograms

Figure 1 shows the raw cyclic voltammograms (CVs) obtained in plating baths of different compositions, listed in Table 4. CV analysis provides useful information on alloying component behavior during electrodeposition and phase structure characteristics of the electrodeposited phase.

Table 4. Plating bath compositions connected with the Cyclic Voltammograms

Types of baths for CV	**$ZnSO_4 \cdot 7H_2O$**	**$Na_3C_6H_5O_7$** (trisodium citrate)	**Na_2SO_4**	**$(NH_4)_2SO_4$**	**$FeSO_4 \cdot 7H_2O$**	**$Na_2MoO_4 \cdot 2H_2O$**	**$Na_2WO_4 \cdot 2H_2O$**
Zn_Cit	0.4M	0.4M	---	---	---	---	---
Zn_Cit_Na_2SO_4	0.4M	0.4M	0.2M	---	---	---	---
Zn_Cit_$(NH_4)_2SO_4$	0.4M	0.4M	---	0.2M	---	---	---
Fe_Cit	---	0.4M	---	---	0.4M	---	---
Fe_Cit_Na_2SO_4	---	0.4M	0.2M	---	0.4M	---	---
Fe_Cit_$(NH_4)_2SO_4$	---	0.4M	---	0.2M	0.4M	---	---
Zn-Fe_NaCit	0.4M	0.4M	---	---	0.4M	---	---
Zn-Fe_NaCit_Na_2SO_4	0.4M	0.4M	0.2M	---	0.4M	---	---
Zn-Fe_NaCit_$(NH_4)_2SO_4$	0.4M	0.4M	---	0.2M	0.4M	---	---
Zn-Fe-Mo_NaCit	0.4M	0.4M	---	---	0.4M	0.01M	---
Zn-Fe-Mo_NaCit_Na_2SO_4	0.4M	0.4M	0.2M	---	0.4M	0.01M	---
Zn-Fe-Mo_NaCit_$(NH_4)_2SO_4$	0.4M	0.4M	---	0.2M	0.4M	0.01M	---
Zn-Fe-W_NaCit	0.4M	0.4M	---	---	0.4M	---	0.01M
Zn-Fe-W_NaCit_Na_2SO_4	0.4M	0.4M	0.2M	---	0.4M	---	0.01M
Zn-Fe-W_NaCit_$(NH_4)_2SO_4$	0.4M	0.4M	---	0.2M	0.4M	---	0.01M

Figure 1 (a) Cyclic voltammograms (CVs) of Zn deposited from various citrate solution systems. In the $ZnSO_4$ + citrate electrolyte solution, Zn^{2+} reduction is inhibited by strong citrate ligand complexation that stabilizes Zn^{2+} by moving its deposition potential negatively -1.12 V vs. Ag|AgCl . Stabilization of Zn^{2+} will increase the energy requirement that is necessary for Zn^{2+} release by decreasing cathodic current density. From -1.25 to -1.35 V, a plateau was

observed, which was possibly caused by the diffusion limitation of the Cit–Zn complex between these two voltages[76]. The introduction of ammonium sulphate strongly enhances the cathodic current and converts the reduction towards less negative potentials -1.2 V vs. Ag|AgCl, suggesting enhanced Zn deposition by ammonium ions. Such an effect is due to destabilizing Zn–citrate complexes and freeing Zn^{2+} ions. Adding sodium sulphate moderately enhances the result of that of citrate alone, and the reduction potential moves more negatively -1.25 V vs. Ag|AgCl. Na_2SO_4 substantially raises ionic strength and lowers resistance, improving conductivity and current response. The Zn-citrate complexation is not substantially altered by sodium ions; therefore, the deposition potential is comparable to that of the citrate-only bath.

In Figure 1 (b), In the $FeSO_4$ + citrate electrolyte, the deposition current density is relatively low, and the cathodic peak is shifted toward more negative potentials -0.4 V vs. Ag|AgCl . This effect can be explained by the strong affinity of citrate ligands for Fe^{2+}/Fe^{3+} ions, forming stable Fe–citrate complexes. Upon the addition of ammonium sulphate, a clear increase in cathodic current is observed, together with a shift of the reduction peak toward more negative potentials, and reduction start to begin at -0.8 V vs. Ag|AgCl. The anodic stripping peak is also more pronounced, suggesting enhanced reversibility of the Fe deposition–dissolution process. This improvement can be attributed to the role of NH_4^+ ions, which act as weak proton donors and modify the local pH near the electrode surface. In addition, with sodium sulphate bath, the reduction potential moves more negative, -1.25 V vs. Ag|AgCl, the presence of sodium sulphate produces only a moderate enhancement in deposition current compared to citrate alone. Sodium sulphate mainly increases the ionic strength of the solution and reduces solution resistance, which improves the conductivity.

In Figure 1 (c) the Zn-Fe plating bath curve indicates a stable electrochemical interaction between iron and zinc ions in the complexing medium. The addition of ammonium sulphate results in a notable shift towards more negatively cathodic potentials with a corresponding increase in current density, which reflects enhanced ionic conductivity and increased electrochemical activity due to additional ammonium ions facilitate charge transfer. Conversely, the solution with sodium sulphate exhibits slightly reduced cathodic current and more stable anodic activity. The increase in current density following the reduction potential is evident on all curves, with a notable increase corresponding to the onset of fast reduction and deposition processes. The highlighted region demonstrates the shift from charge-transfer control towards mass-transfer limitation, where the electroactive species is rapidly depleted in

the immediate proximity of the electrode surface and the diffusion rate dominates and becomes the central factor affecting the electrochemical process.

In Figure 1 (d) (e) Temporary peaks are seen as early as in the initial moments of the scans, which reflect the onset of nucleation events on the substrate surface itself or in the solution [74]. These observations imply that initial metal ion reduction and cluster formation take place at the very beginning of the potential sweep. In Figure 1b, the reduction potential of the Fe ions in the trisodium citrate-added $FeSO_4$ electrolyte is well indicated at −0.40 V vs. Ag|AgCl. The peak is due to the reduction of Fe^{2+} ions to iron metal. Furthermore, a distinct reduction peak at −0.6 V vs. Ag|AgCl is seen for the reduction of molybdenum (d) and tungsten (e) species. There may be a possibility of co-reduction of Fe-Mo or Fe-W around the potential of -0.6 V vs. Ag|AgCl. It should be noted that water-soluble molybdenum is mostly present in the form of molybdate ions, which are reduced through complicated multi-step reduction reactions. In accordance with earlier studies, total reduction of molybdate (MoO_4^{2-}) into elemental molybdenum does not involve a simple six-electron transfer in a single step [103]. Instead, intermediate Mo-oxide species will be created in the course of deposition and may affect the morphology and composition of the resulting coating. The onset of reduction at a less negative potential and the switching potential at a lower current density in the ammonium-free bath. This is possibly because the free MoO_4^{2-} ions are present in the bath or due to complex formation between citrate ions and ammonium ions. The ammonium ion base solution affects the potential with a high density of current from the bath that does not have ammonium ions. This is possibly because of complex formation between ammonium ions and the rest of the metal ions, or electrolyte composition change, or electrode surface property change with the deposition. In Fig.1(e), no significant changes in reduction were noticed with the addition of sodium tungstate.

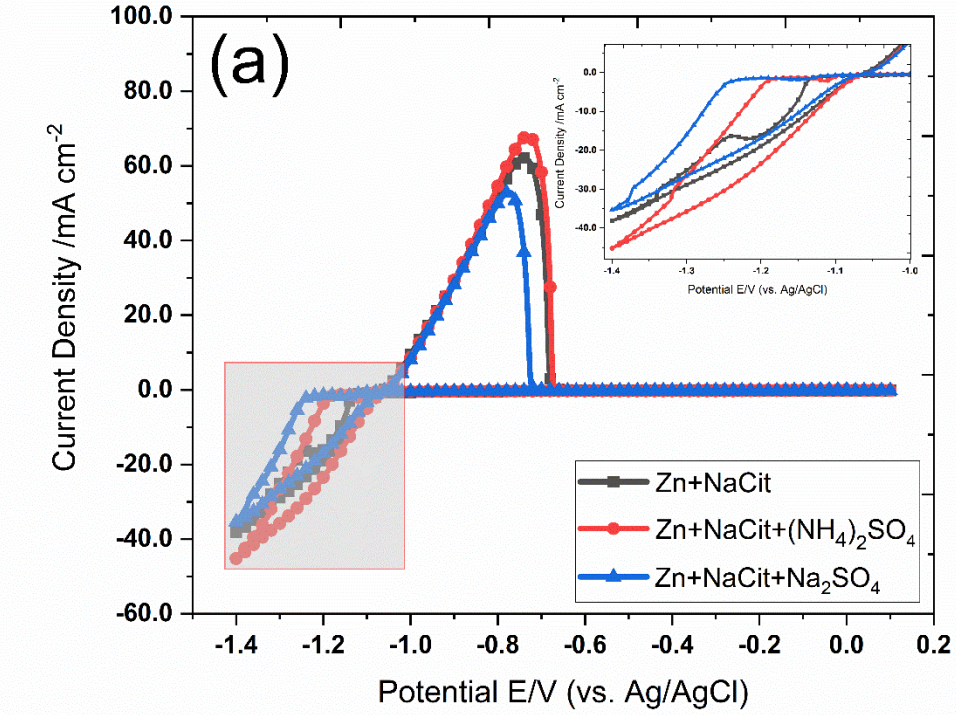
(a)
Current Density /mA cm-2
Potential E/V (vs. Ag/AgCl)
Zn+NaCit
Zn+NaCit+(NH4)2SO4
Zn+NaCit+Na2SO4

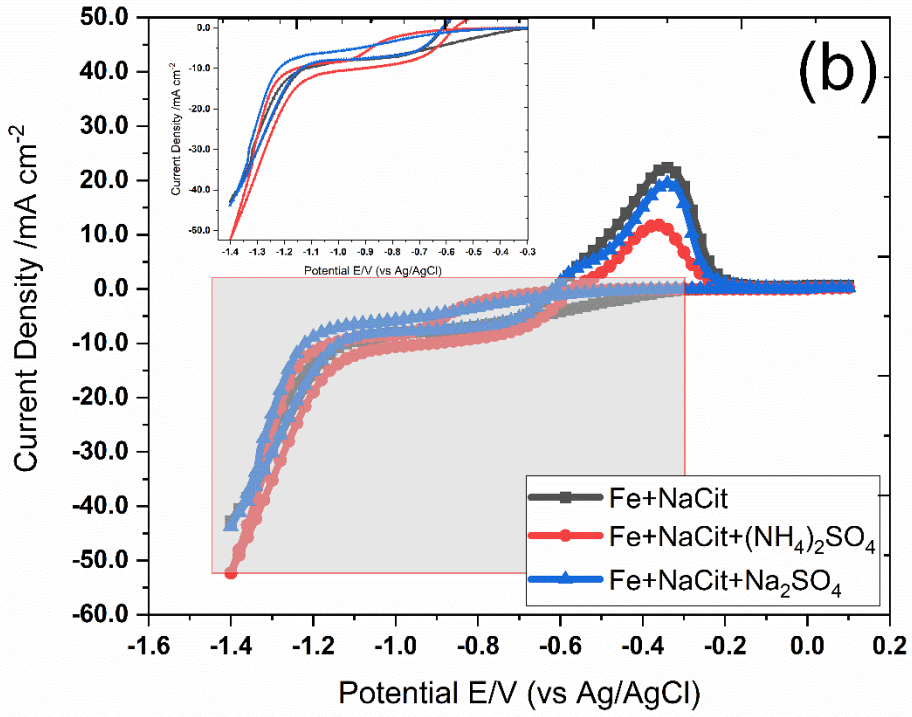
(b)
Current Density /mA cm-2
Potential E/V (vs Ag/AgCl)
Fe+NaCit
Fe+NaCit+(NH4)2SO4
Fe+NaCit+Na2SO4

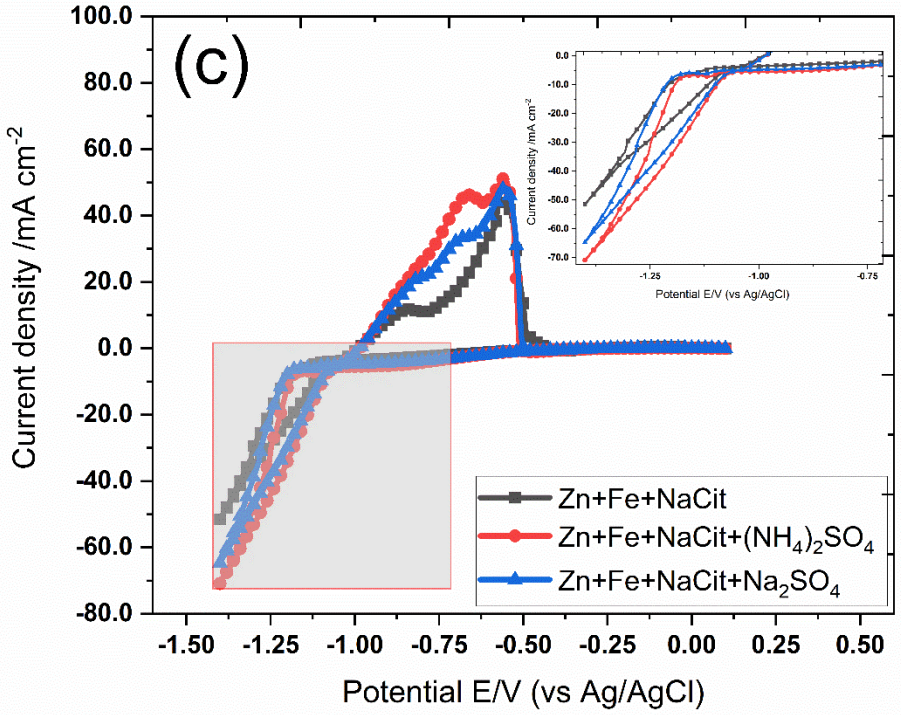
(c)
Current density /mA cm-2
Potential E/V (vs Ag/AgCl)
Zn+Fe+NaCit
Zn+Fe+NaCit+(NH4)2SO4
Zn+Fe+NaCit+Na2SO4

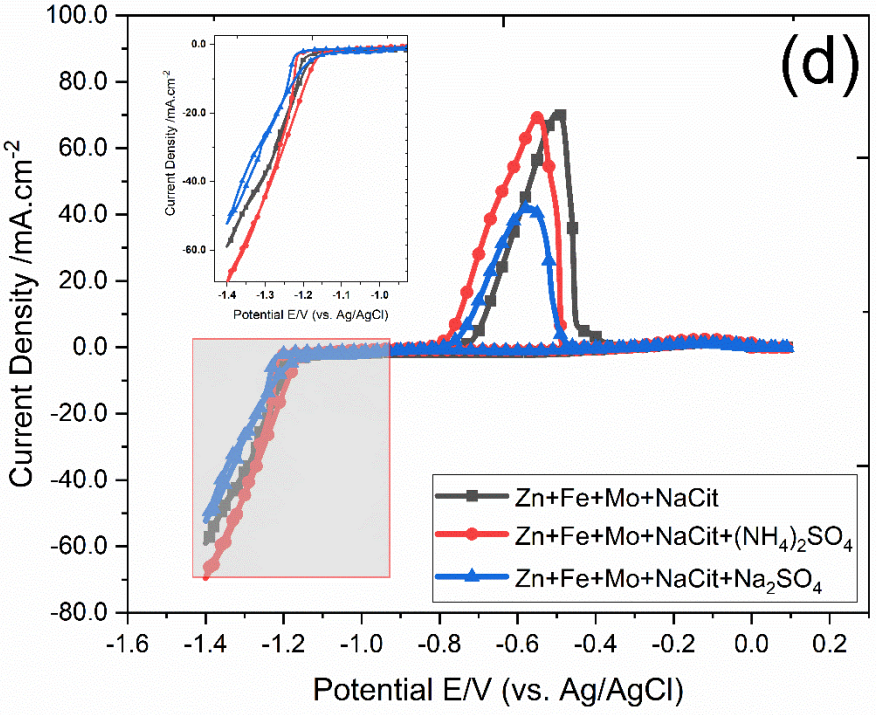
(d)
Current Density /mA.cm-2
Potential E/V (vs. Ag/AgCl)
Zn+Fe+Mo+NaCit
Zn+Fe+Mo+NaCit+(NH4)2SO4
Zn+Fe+Mo+NaCit+Na2SO4

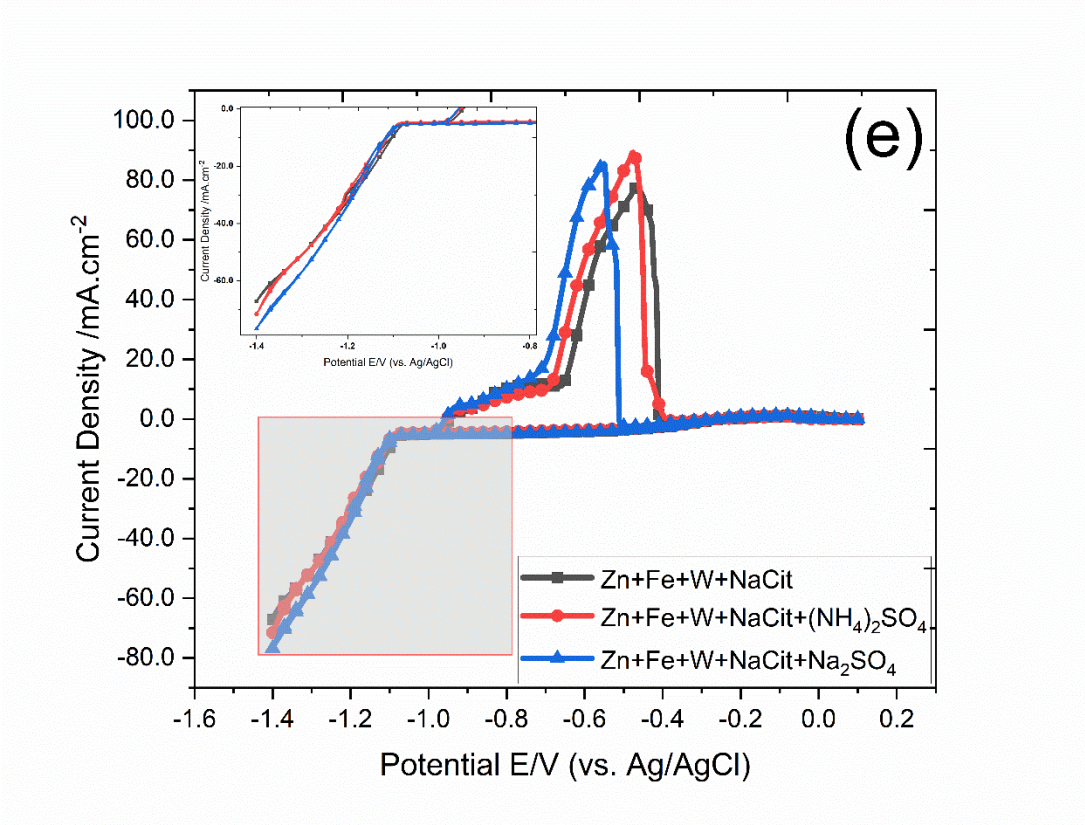

Fig. 1. Cyclic voltammograms registered on a Pt electrode in (a) Zn, (b) Fe,(c) Zn-Fe, (d) Zn-Fe-Mo and (e) Zn-Fe-W plating baths with different compositions specified in Table 4 at scan rate 5 mV s^{-1}, ω = 800 rpm, T = 25 ˚C and pH 5.7.

The anodic current response obtained in the "Zn-Fe_NaCit" bath demonstrates definite peaks of oxidation for zinc at a potential of −0.8 V vs. Ag|AgCl. The particular peak may indeed be associated with the process of Zn dissolution from η phase, which is known to be the zinc-rich phase of the material. A second peak of oxidation observed at −0.7 V vs. Ag|AgCl, associated with the oxidation of Zn, and another small bump is seen at −0.48 V vs. Ag|AgCl, and this peak may be associated with the Zn-Fe phase. By the addition of Mo or W to the system, the peak previously noticed for Zn dissolution from the η phase is no longer available, basically disappearing, while at the same time the peak for the dissolution phase of Zn-Fe presents a current density that is considerably lower. This is due to the fact that the metals of the alloy are dissolved by passing through different intermediate phases, resulting in the detection of multiple peaks in the electrochemical oxidation process of the alloys, as indicated in the source [[104]]. Furthermore, the variation in the composition of the electrolyte can have the ability to result in the decrease in the area under this anodic peak. This decrease in area typically indicates the reduction in the total charge that has been passed during the anodic process.

4.2 UV-Vis Spectra Study

In Figure 2 (a)(b)(c)(d), UV–Vis spectra of the electrodeposition bath containing Zn-Fe-Mo and Zn-Fe-W citrate sulphate were recorded at 10-min intervals for six spectra over 50 min. in Figure 2 show similar spectra for the Mo and W base electrolyte. Spectra exhibit strong absorption below 420 nm, as would be the case for citrate ligand $\pi \rightarrow \pi^*$ transitions, with a supporting structure in the visible region that seems to be assigned to metal–ligand charge transfers (LMCT) and d d transitions. There are significant amounts of Fe and Mo in the solution that are generating hydroxide and citrate complexes that scatter strongly near short wavelengths and flatten/distort absorbance below the scattering-dominated region[105]. Both mask weak Zn bands as well as cause data to be unusable due to "discontinuity".

Initially, the spectrum showed that there was a distinct absorption feature in the region of 470–490 nm, corresponding to ligand-metal charge transfer transitions of the type seen in Fe(III)–citrate complexes. The literature also supports that Fe(III) citrate complexes in aqueous solution have spectrally active LMCT transitions that range from 470 to 500 nm, with peaks shifting according to pH and ligand (citrate) concentration [105],[106].

The peak due to absorption at approximately 480 nm reduced stepwise with time. This is reflective of the stepwise reduction or consumption of Fe(III) species during electrodeposition. Since Fe^{2+} complexes are weakly absorbing in this region, the diminishing LMCT band is consistent with either (i) cathodic reduction of Fe^{3+} to Fe^{2+} or (ii) co-deposition of iron together with zinc and molybdenum.

A broad, parabolically shaped hump from 650 to 880 nm is most likely caused by intervalence/charge-transfer absorption of reduced molybdenum species / polyoxomolybdate or mixed-valence Mo clusters[107], [108]. This feature developed and intensified around 800 nm with a longer deposition time. This band can be assigned to partial reduction of the molybdate to Mo(V) species, which is expected to absorb broadly in the red–near-IR region (600–800 nm). The development of this band is diagnostic of the redox activity of molybdenum during electrodeposition and is consistent with the incorporation or partial reduction of molybdate ions on the cathode surface. The literature also supports that molybdenum absorption spectra were recorded at 865 nm[107] with a shoulder at 710 nm and also at 745 nm[108].

In the Zn-Fe-W case, it is likely that, during electrodeposition, some W(VI) from W-source is being reduced to W(V) or to a lower oxidation level, forming mixed valence or partially reduced tungsten oxide/bronze species. Typically, these processes result in intervalence charge transfer (IVCT) and/or polaronic absorption that extend to the visible and near-IR spectrums [109], [110]

It is likely that the bump, observed during Zn-Fe-W electrodeposition, is caused by mixed-valence W species (e.g. W^{5+}/W^{4+}, oxygen-deficient tungsten oxide), possibly in conjunction with other species. The literature indicates that mixed-valence tungsten (such as partially reduced WO_3, and WO_{3-x}) exhibits broad absorption in visible and near-infrared regions (such as 650-900 nm) [109], [111] .

There is a clear and consistent increase in the value of absorbance throughout the wavelength spectrum. However, the largest variations in values occur in the region from 420 to 500 nanometres. The consistent increase in the value of absorbance also indicates that the electrolyte is not in a chemically stable condition during the measurement period. Instead, the UV-reactive components increase in the system over time.

Iron species in the electrolyte mixture may undergo progressive iron oxidation ($Fe^{2+} \rightarrow Fe^{3+}$) or enter the formation of iron ligand complexes. Slow iron oxidation in the presence of an aerated electrolyte was previously observed to increase iron-related peaks in the spectrum [112]. Similarly, the iron-molybdenum system used in the study presents various iron-related processes by which the increase in the optical density in the spectrum becomes feasible.

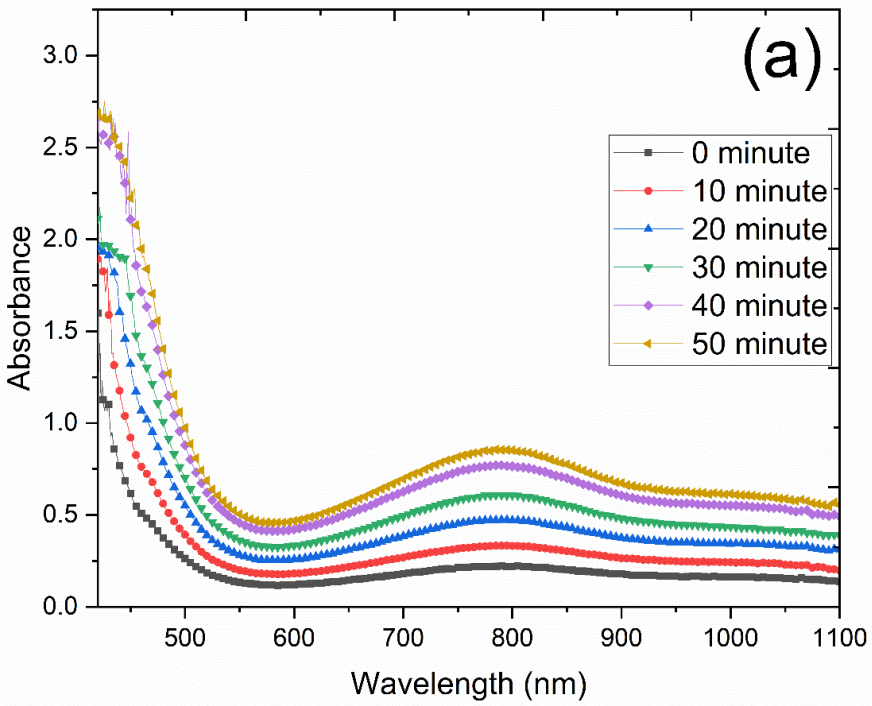
(a)
Absorbance
Wavelength (nm)
0 minute
10 minute
20 minute
30 minute
40 minute
50 minute
3.0
2.5
2.0
1.5
1.0
0.5
0.0
500
600
700
800
900
1000
1100

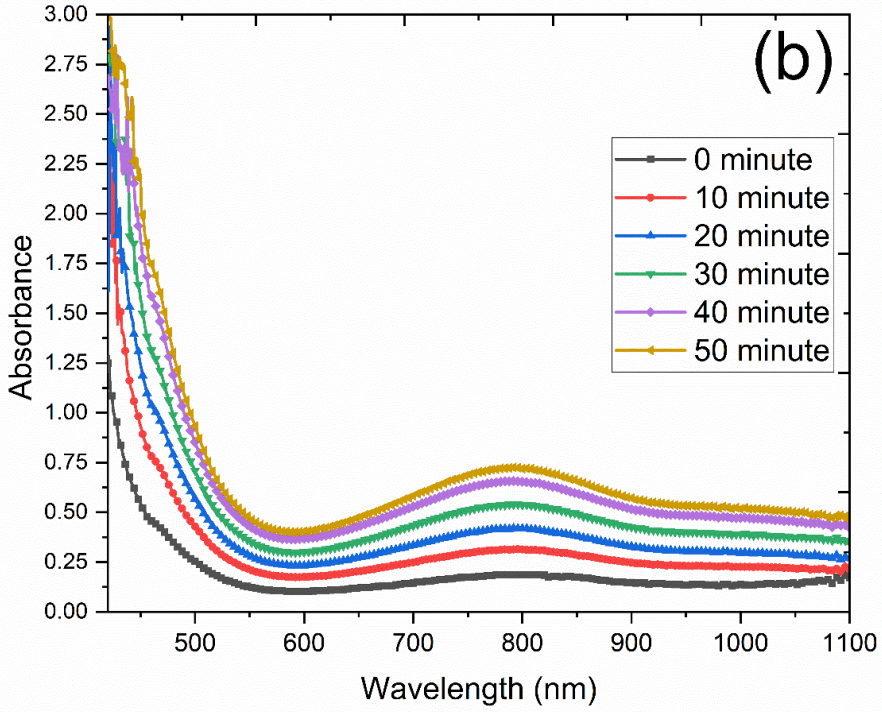
(b)
Absorbance
Wavelength (nm)
0 minute
10 minute
20 minute
30 minute
40 minute
50 minute
3.00
2.75
2.50
2.25
2.00
1.75
1.50
1.25
1.00
0.75
0.50
0.25
0.00
500
600
700
800
900
1000
1100

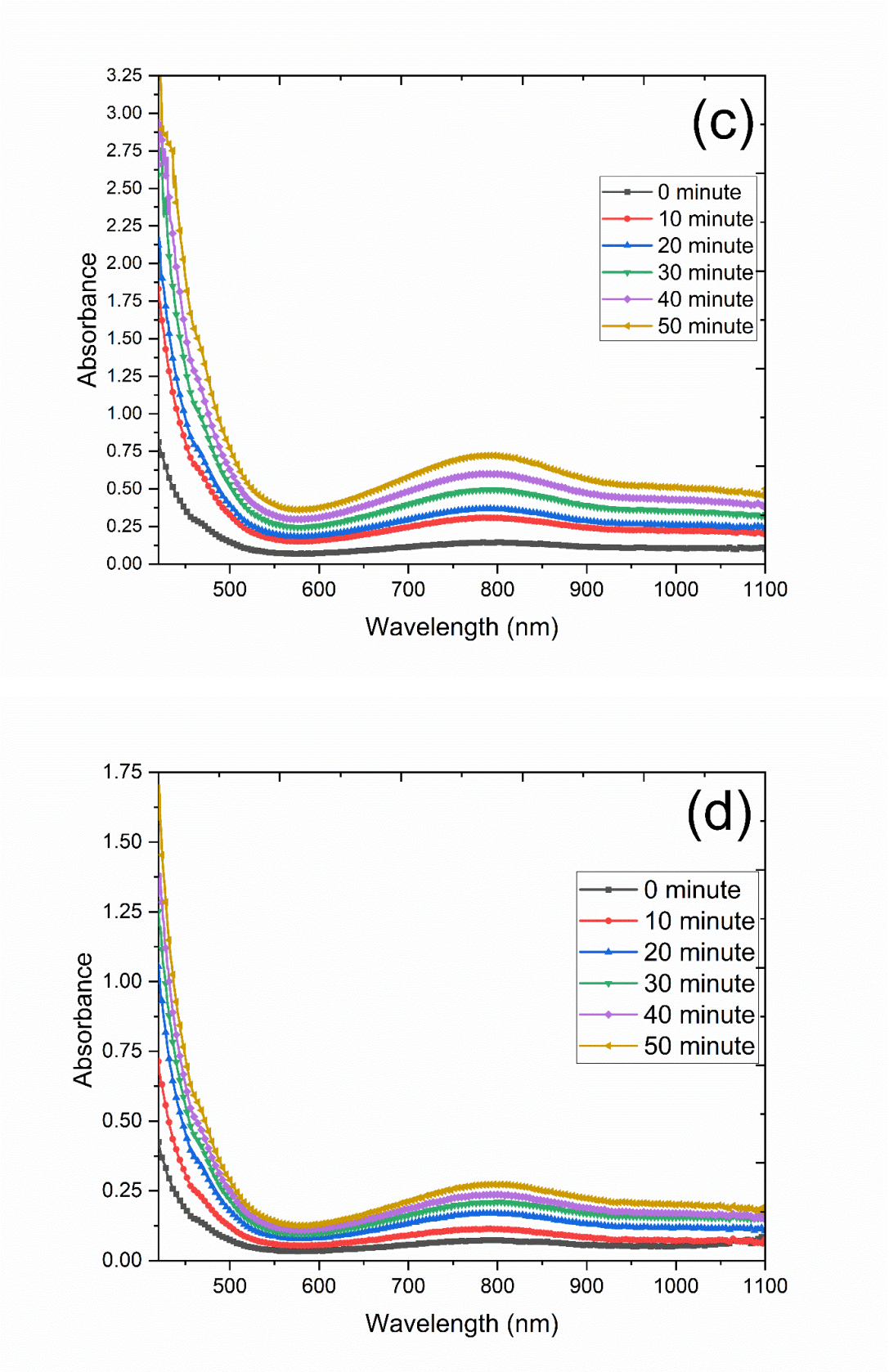

Fig. 2 The UV-Vis spectra observed from the electrolyte after every 10 minutes during the electrodeposition process of (a) Zn-Fe-Mo alloy in Na_2SO_4 base electrolyte (b) Zn-Fe-Mo alloy in $(NH_4)_2SO_4$ base electrolyte (c) Zn-Fe-W alloy in Na_2SO_4 base electrolyte (d) Zn-Fe-W alloy in $(NH_4)_2SO_4$ base electrolyte.

4.3 The influence of plating bath composition and current density on coating's morphology

4.3.1 Zn-Fe-Mo

The microstructural properties and surface morphology of the coatings formed from electrodeposition in baths including Na_2SO_4 or $(NH_4)_2SO_4$ salts with varying current densities are illustrated in Figures 3 and 4 using scanning electron microscopy (SEM) characterization. Physical and visual inspection of coatings shows clear differences in texture and quality according to used current density. At lower current densities (10 and 15 mA cm^{-2}), there is a loosely adherent powdery morphology with a greyish colour (noticeable during visual inspection) accompanied by the existence of a black precipitate upon electrodeposition exhibiting poor substrate adhesion. By contrast, if the current density is increased to 20 mA cm^{-2}, the metal coatings change considerably to being smoother, homogeneous and dense with greater structural integrity. Further increase of the current density to 25 mA cm^{-2} yields less defective deposits, such as powdery or charred residues on the edges. The higher edge quality is either caused by the higher current density leading to a more uniform deposition distribution or by process parameter limitations, e.g., poor agitation during the electrodeposition, which might influence local mass transfer. The trends identified underscore the critical role played by current density in regulating coating morphology, adhesion, and uniformity, with optimum deposition conditions being observed in the vicinity of the 20–25 mA cm^{-2} range under the experimental conditions explored.

The peculiar co-deposition phenomenon of the coatings produced from a Na_2SO_4 base electrodeposition bath showed typical microstructural features that depended on the current density applied. For low current densities of 10 and 15 mA cm^{-2}, the coatings consisted of small, rounded agglomerates with irregular distribution, resulting in heterogeneous surface morphologies as reflected from Figures 3a and 3b. However, increasing the current density up to 20 and 25 mA cm^{-2} generated much smoother, denser, and uniform coatings with flat surface topography (Figs. 3c and 3d). Although coatings formed at high current densities possessed a nodular-like morphology similar to deposits produced from a Na_2SO_4 including bath, close-up nanoscale observation unveiled stretched grain structures different from the characteristic equiaxed nanostructures typical of sulphate-containing baths. Such a morphological shift, i.e., from agglomerated pore-like particles at low current densities through continuous finer

deposits at high current densities, can be considered as proof of competition of deposition kinetics and bath chemistry as mechanisms of microstructural evolution. Volatilization of ammonium ions could impact nucleation kinetics and consequently yield stretched grains under high current conditions, indicative of possible elevated mechanical and functional coatings.

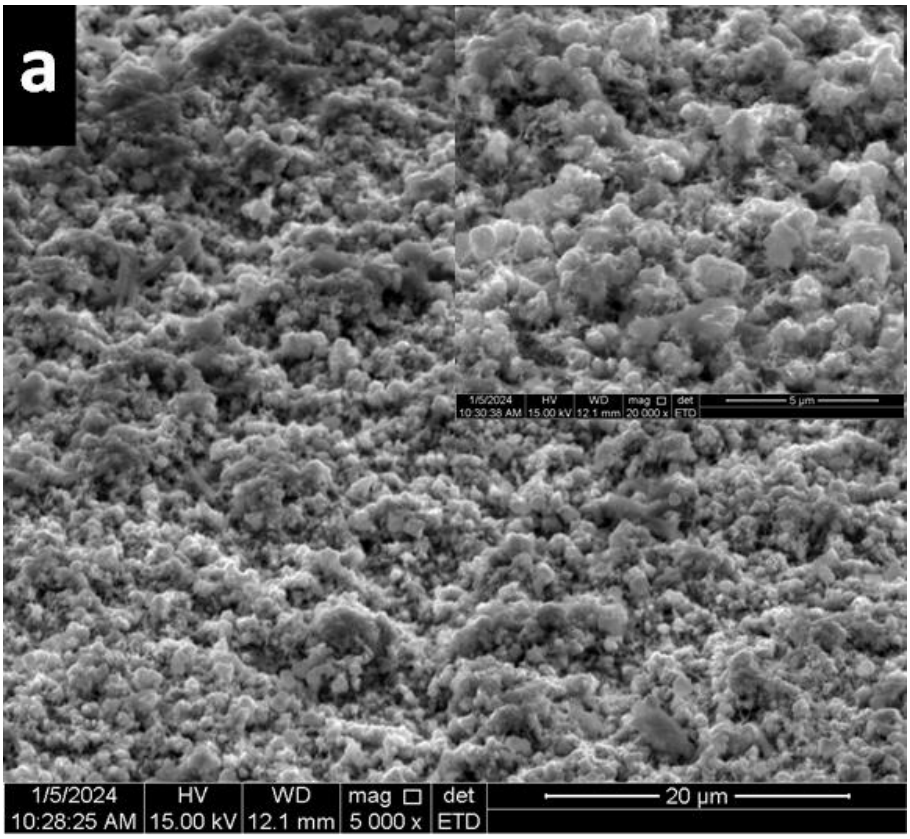

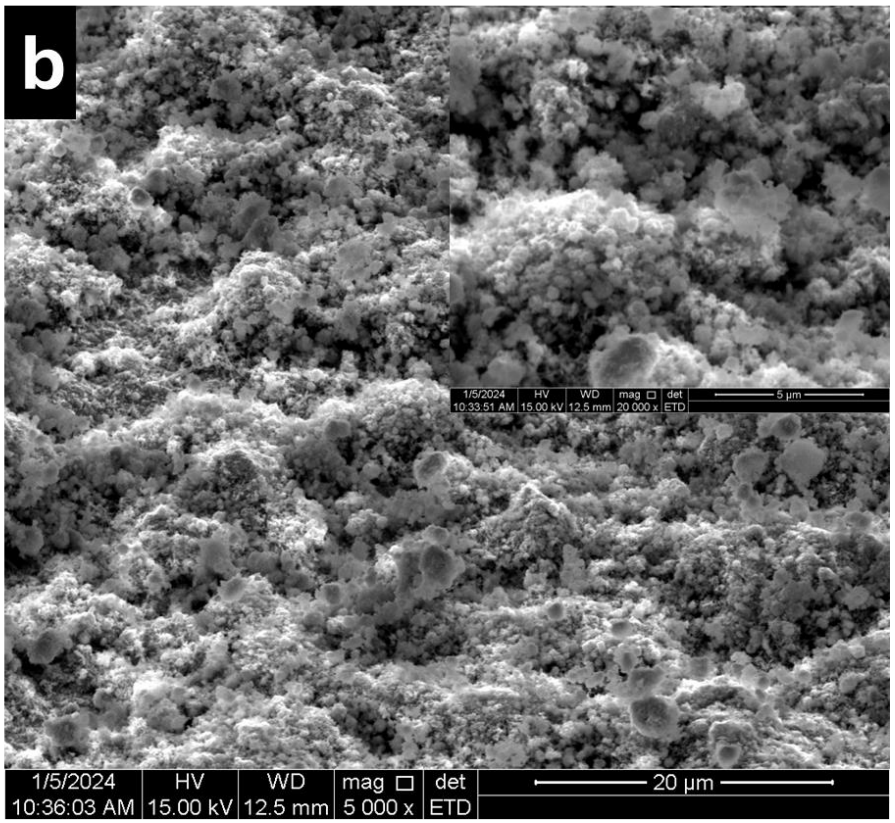
b
1/5/2024 10:33:51 AM
HV 15.00 kV
WD 12.5 mm
mag 20 000 x
det ETD
5 µm
1/5/2024 10:36:03 AM
HV 15.00 kV
WD 12.5 mm
mag 5 000 x
det ETD
20 µm

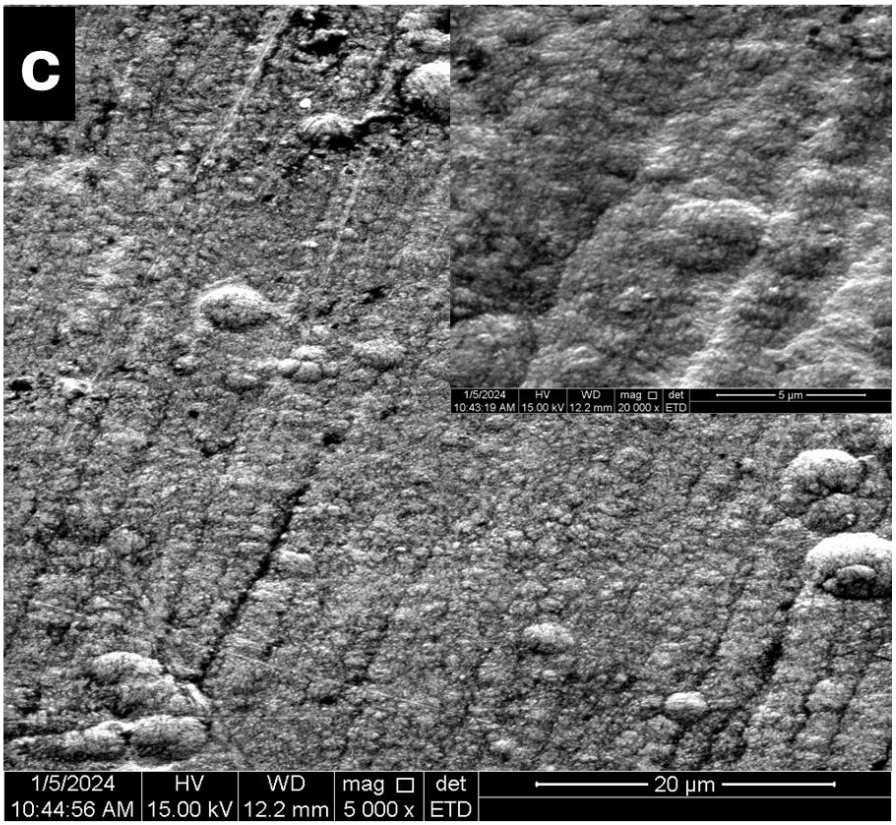
c
1/5/2024 10:43:19 AM
HV 15.00 kV
WD 12.2 mm
mag 20 000 x
det ETD
5 µm
1/5/2024 10:44:56 AM
HV 15.00 kV
WD 12.2 mm
mag 5 000 x
det ETD
20 µm

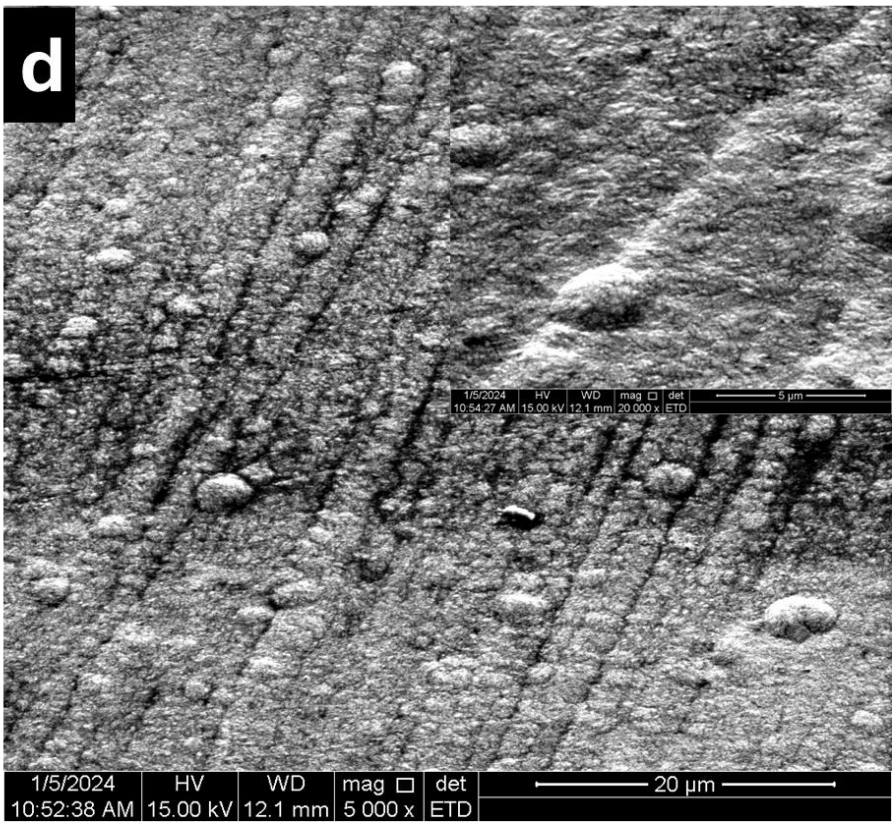

Fig. 3. Surface morphology of the Zn-Fe-Mo alloy coatings electrodeposited on the steel substrate with Na_2SO_4 base galvanic bath at: (a) 10; (b) 15; (c) 20 and (d) 25 mA cm^{-2}.

The coatings obtained from the $(NH_4)_2SO_4$ base (ammonium-ion-containing) bath exhibited varying structure development depending on the current density used. Under low current densities (10 and 15 mA cm^{-2}), the deposits exhibited well-developed fibrous surface morphology (Figs. 4a and 4b), which is consistent with Kosugi et al[9], where it was reported that alloy electrodeposition under low current conditions has a tendency to develop fibrous structures. When the current density was increased to 20 mA cm^{-2}, the surface topography was altered to that of a flaky, irregular texture (Fig. 4c). In comparison, coatings developed at 25 mA cm^{-2} assumed a smooth, fine-grained structure with a nodular morphology parallel to the substrate grinding marks (Fig. 4d). Comparative SEM observation of deposits from Na_2SO_4 or $(NH_4)_2SO_4$ baths helps to further highlight the drastic difference in final morphologies and demonstrates how bath composition and current density together exert a synergistic role in determining microstructural characteristics. These differences suggest that ammonium ions play a determining role in regulating nucleation and growth processes and, in particular, in mediating the transition between nodular and fibrous morphologies at high current densities.

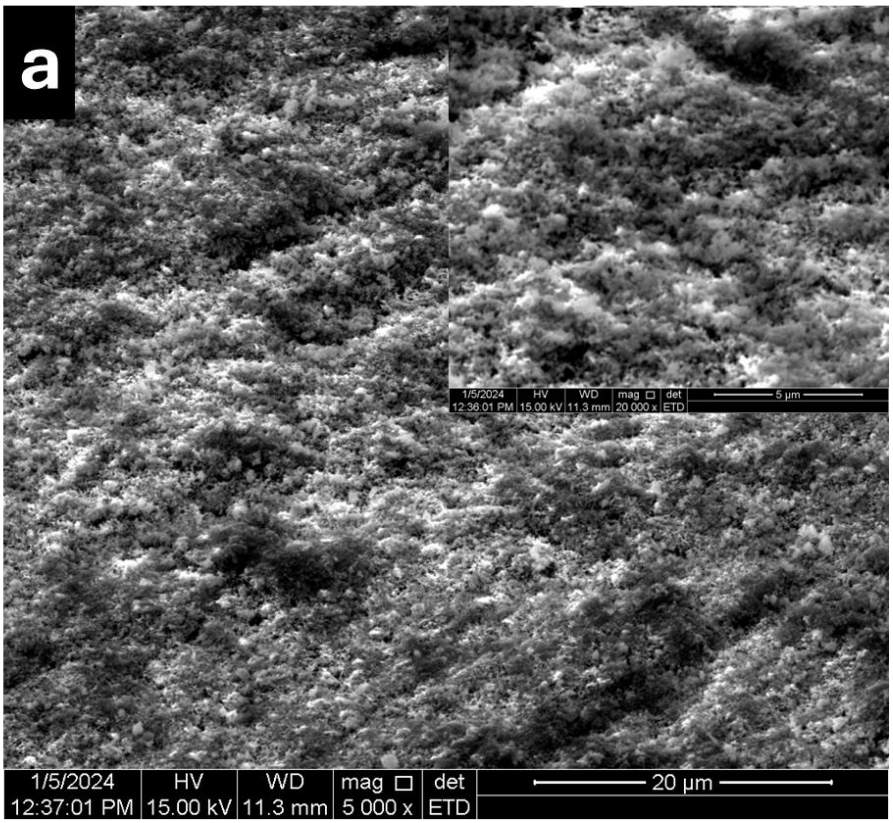
a
1/5/2024
12:36:01 PM
HV
15.00 kV
WD
11.3 mm
mag
20 000 x
det
ETD
5 µm
1/5/2024
12:37:01 PM
HV
15.00 kV
WD
11.3 mm
mag
5 000 x
det
ETD
20 µm

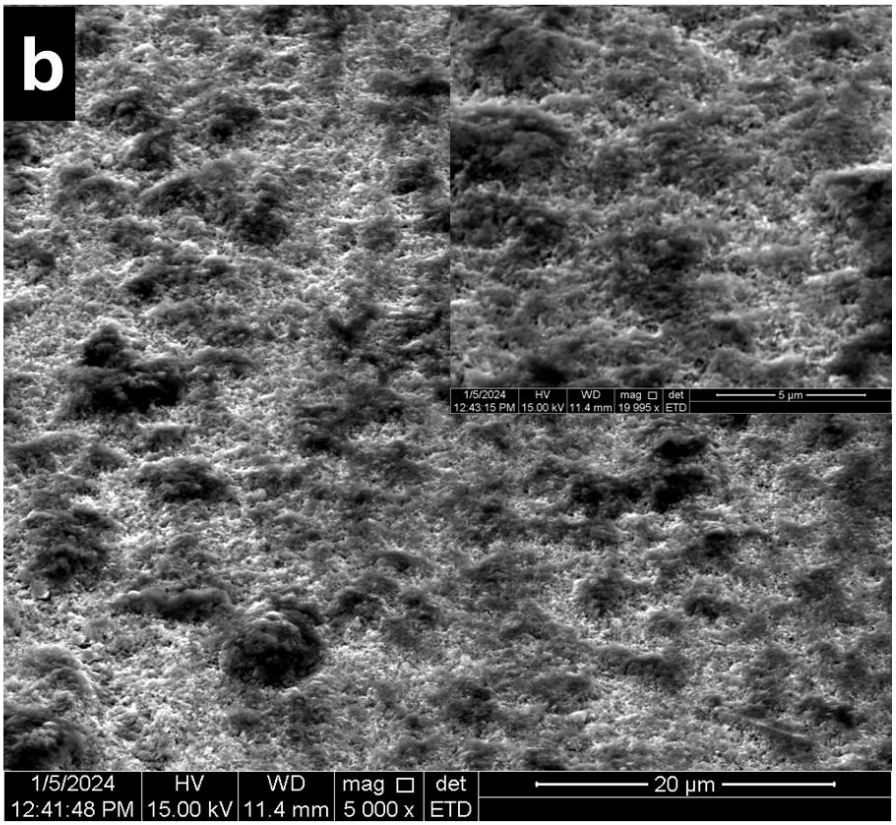
b
1/5/2024
12:43:15 PM
HV
15.00 kV
WD
11.4 mm
mag
19 995 x
det
ETD
5 µm
1/5/2024
12:41:48 PM
HV
15.00 kV
WD
11.4 mm
mag
5 000 x
det
ETD
20 µm

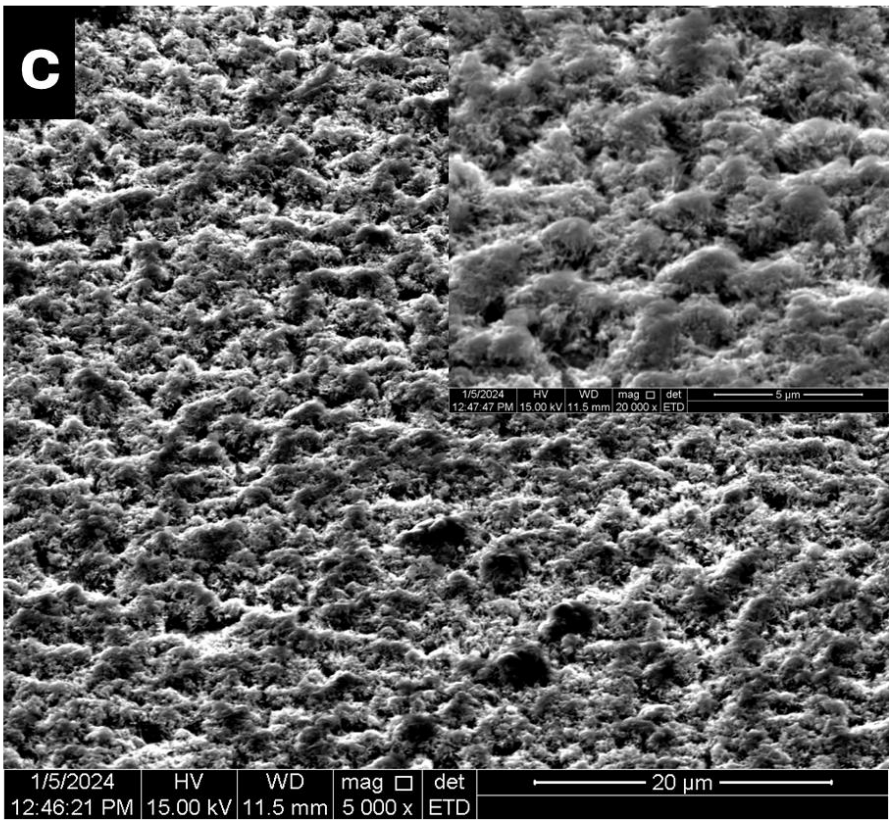
c
1/5/2024 12:47:47 PM
HV 15.00 kV
WD 11.5 mm
mag 20 000 x
det ETD
5 µm
1/5/2024 12:46:21 PM
HV 15.00 kV
WD 11.5 mm
mag 5 000 x
det ETD
20 µm

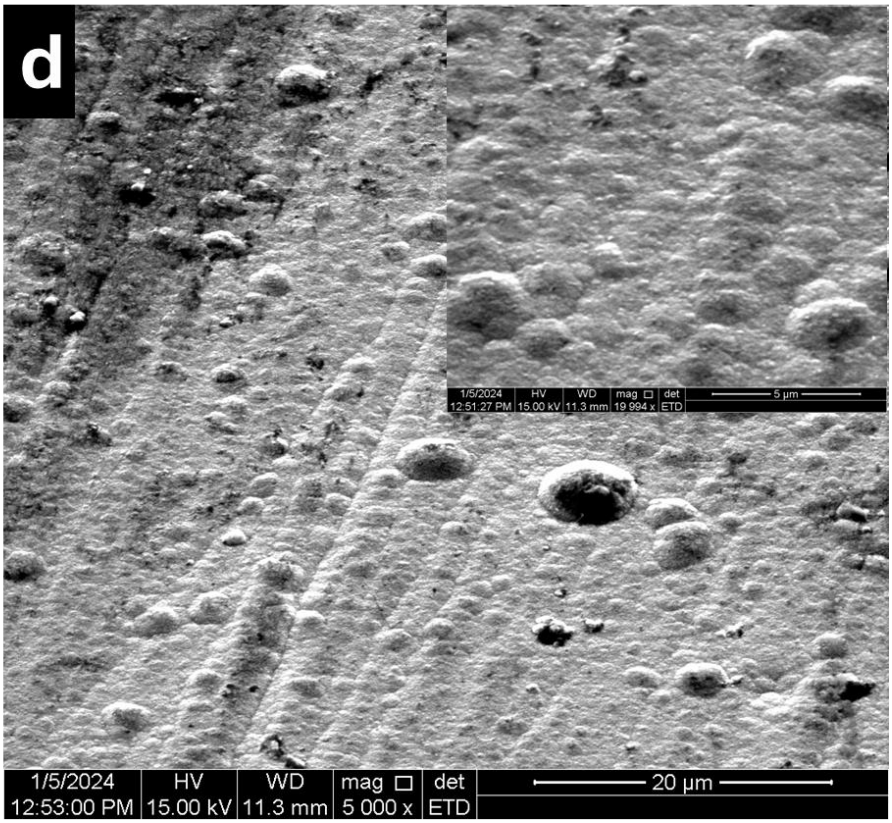
d
1/5/2024 12:51:27 PM
HV 15.00 kV
WD 11.3 mm
mag 19 994 x
det ETD
5 µm
1/5/2024 12:53:00 PM
HV 15.00 kV
WD 11.3 mm
mag 5 000 x
det ETD
20 µm

Fig. 4. Surface morphology of the Zn-Fe-Mo alloy coatings electrodeposited on the steel substrate with $(NH_4)_2SO_4$ base galvanic bath at: (a) 10; (b) 15; (c) 20 and (d) 25 mA cm^{-2}.

4.3.2 Zn-Fe-W

Figures 5 and 6 present SEM micrographs of coatings produced from plating baths containing either Na_2SO_4 or $(NH_4)_2SO_4$ at various applied current densities. By simple visual inspection of the as-deposited samples, it was possible to observe a significant change in surface appearance depending on the current density value. Indeed, at lower values of current density (i.e., 10 and 15 mA cm^{-2}), the coatings were greyish and powder-like, typical of low-energy depositions with limited efficiency of the reduction process of metal ions. The deposits obtained in this range were, in general, fragile and weakly adherent; in some cases, a black, loosely bound layer formed on the substrate, indicating incomplete nucleation and poor consolidation of the coating. On the contrary, at higher current densities, namely 20 and 25 mA cm^{-2}, the deposits became more metallic and formed thinner yet more compact layers. At 10 mA cm^{-2} (Fig. 5a), the relatively fine grains are uniformly distributed on the surface. The corresponding microstructure exhibits very low porosity and absence of microcracks, indicating that the low deposition rate promotes the process of nucleation under conditions of low growth rates. Such conditions typically favour the formation of dense films with a fine-grained structure. When the current density is increased to 15 mA cm^{-2}, the surface morphology becomes slightly rougher. The grains appear marginally larger, and the coating shows more pronounced nodular growth, likely due to increased availability of metal ions and higher localized deposition rates. Although the overall coating remains relatively uniform, minor powdery regions near the edges can be observed, indicating the onset of localized current concentration effects. The scanning electron micrographs obtained at the higher current densities of 20 and 25 mA cm^{-2} reveal, beyond a doubt, a different morphology of the deposits. The surface becomes less homogeneous, with coarser grains and regions developing a more irregular growth pattern. This may be due to rapid deposition kinetics under high currents that reduce controlled nucleation and favour competitive growth among crystallites, thereby tending to cause uneven grain size distribution and a more heterogeneous surface. This is consistent with literature data on Zn–Fe alloy coatings deposited under such conditions. The above results emphasize the marked influence of current density on coating compactness, grain refinement, and surface integrity[113].

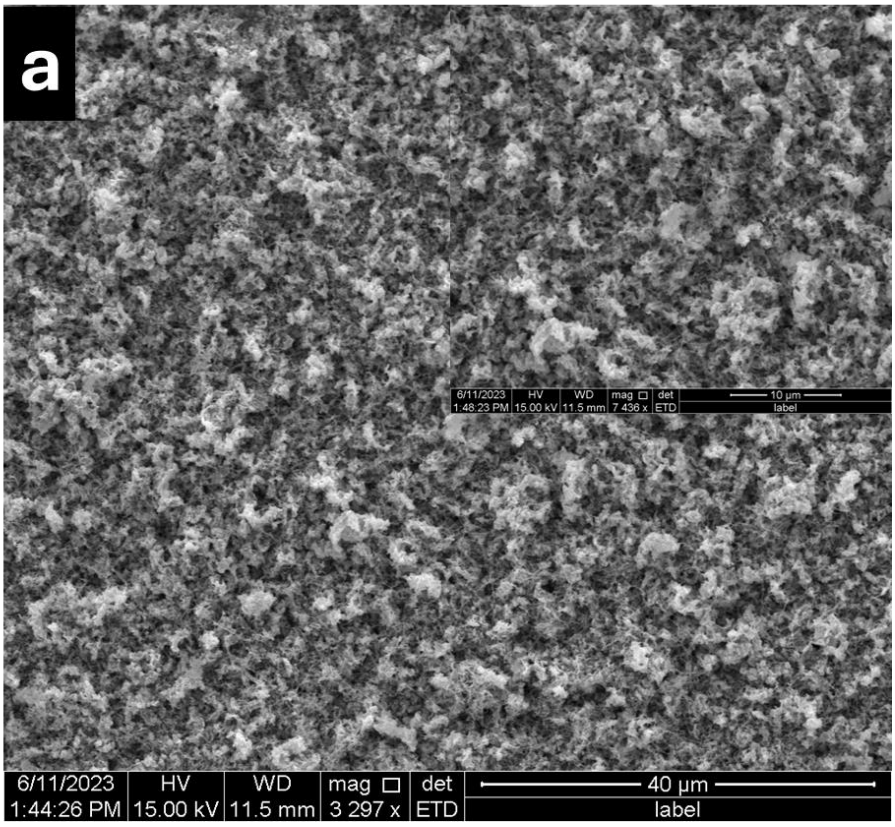
a
6/11/2023 | HV | WD | mag | det | 10 µm
1:48:23 PM | 15.00 kV | 11.5 mm | 7 436 x | ETD | label
6/11/2023 | HV | WD | mag | det | 40 µm
1:44:26 PM | 15.00 kV | 11.5 mm | 3 297 x | ETD | label

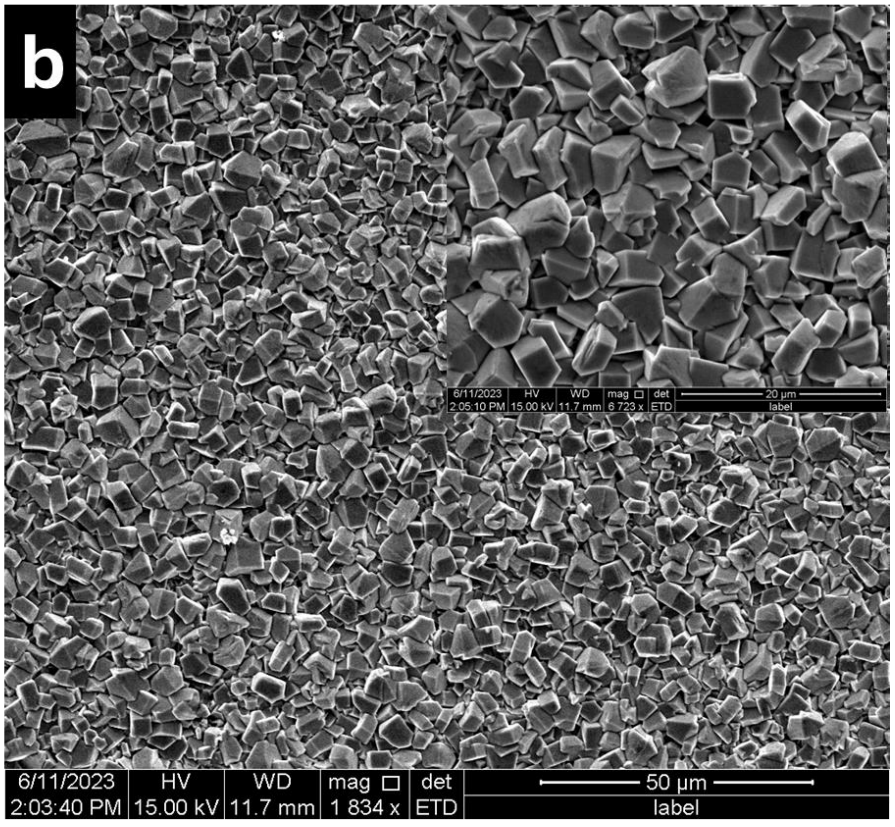
b
6/11/2023 | HV | WD | mag | det | 20 µm
2:05:10 PM | 15.00 kV | 11.7 mm | 6 723 x | ETD | label
6/11/2023 | HV | WD | mag | det | 50 µm
2:03:40 PM | 15.00 kV | 11.7 mm | 1 834 x | ETD | label

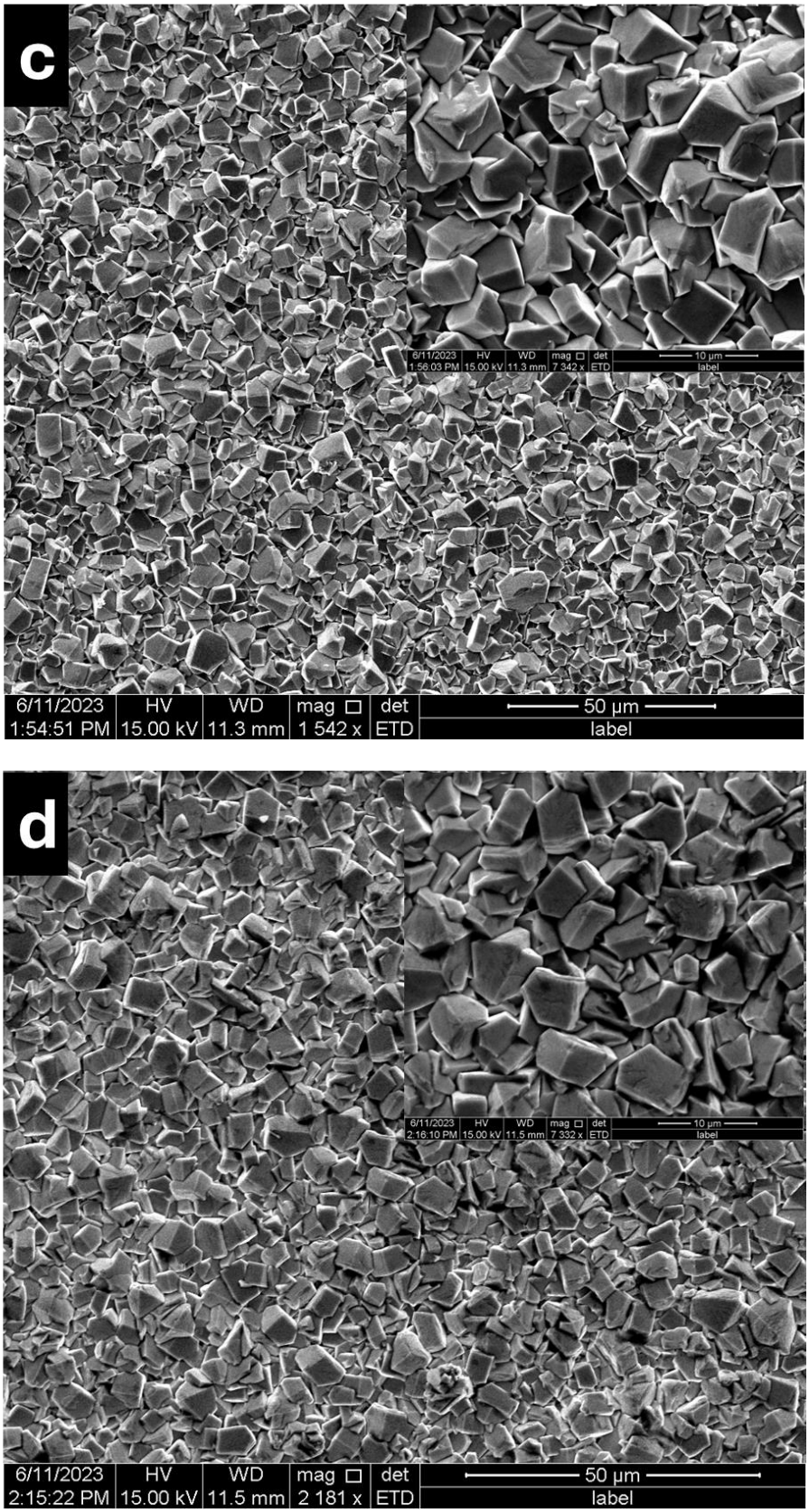

Fig. 5. Surface morphology of the Zn-Fe-W alloy coatings electrodeposited on the steel substrate with Na_2SO_4 base galvanic bath at: (a) 10; (b) 15; (c) 20 and (d) 25 mA cm^{-2}.

It is evident that the morphology of Zn–Fe–W coatings electrodeposited from the $(NH_4)_2SO_4$ (ammonium-containing) base bath depends on the applied current density. At low current densities (10–15 mA cm^{-2}), the coatings are rather rough, porous, and made up of relatively large grains. These deposits also exhibit considerably poor adherence to the substrate. The higher the current, the greater the roughness and porosity, which is indicative of insufficient nucleation density with irregular metal ion reduction. This could unfavorably impact the important mechanical properties of the coating, such as adhesion, hardness, and wear resistance. In contrast, the coatings obtained at 20 mA cm^{-2} demonstrate significantly better morphology. The deposits are uniform, dense, and fine grained, reflecting a more controlled nucleation and growth process promoted by the moderate current level. Small, rounded nodules characterize the surface, showing a consistent, rather smooth texture. This transition reflects an optimal balance between deposition rate and the structural control, which promotes the formation of compact, adherent coatings. The coating morphology again becomes nonuniform at the highest investigated current density of 25 mA cm^{-2}. Larger nodules and an uneven surface texture can be seen upon the rapid deposition rate, showing that controlled crystal formation at high current densities is suppressed by the accelerated growth. It often leads to structural irregularities that adversely affect the coating's mechanical performance. This behavior also parallels observations in other alloy systems, such as Ni-Mo electrodeposits, where increasing ammonium ion concentration induces a transition from amorphous to nanocrystalline structures due to modified nucleation dynamics [114].

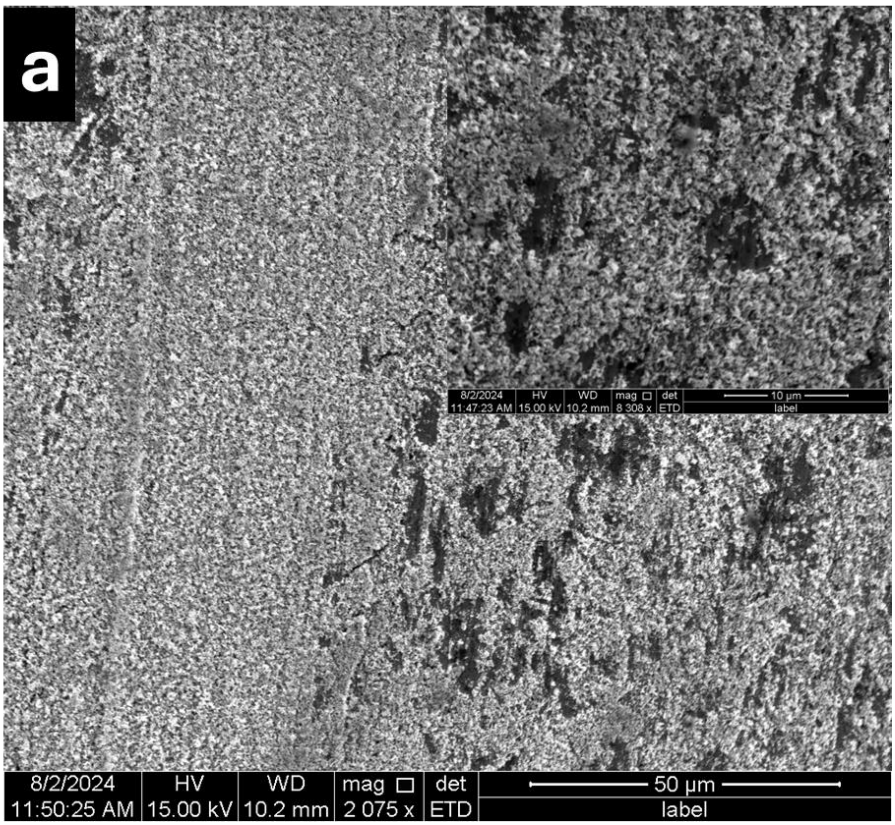
a
8/2/2024 HV WD mag det 50 µm
11:50:25 AM 15.00 kV 10.2 mm 2 075 x ETD label

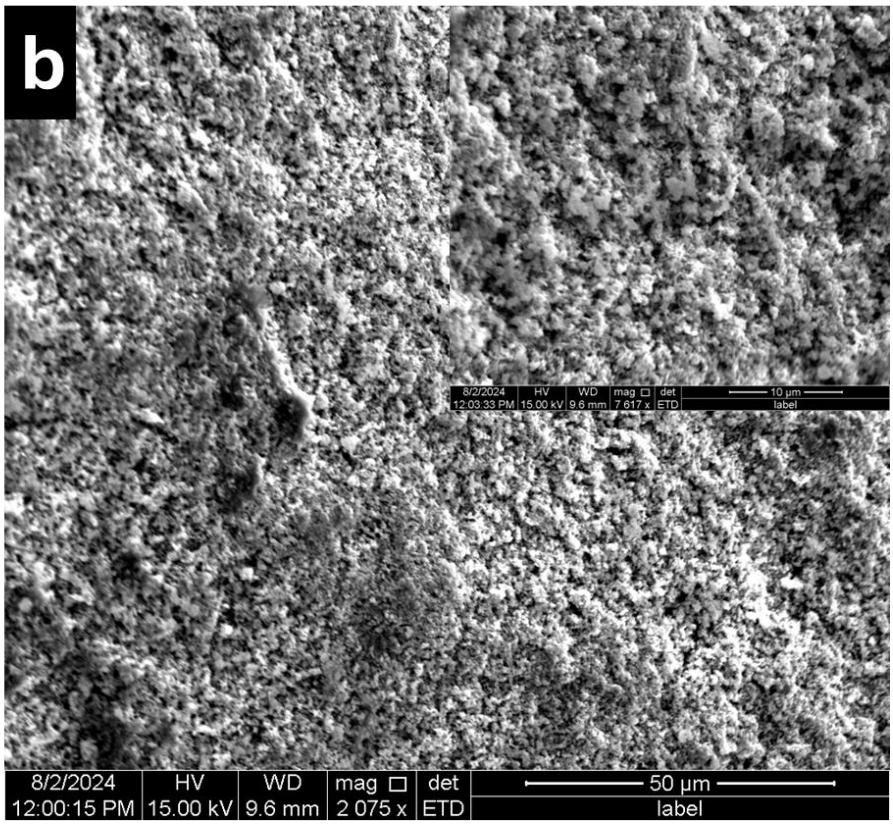
b
8/2/2024 HV WD mag det 50 µm
12:00:15 PM 15.00 kV 9.6 mm 2 075 x ETD label

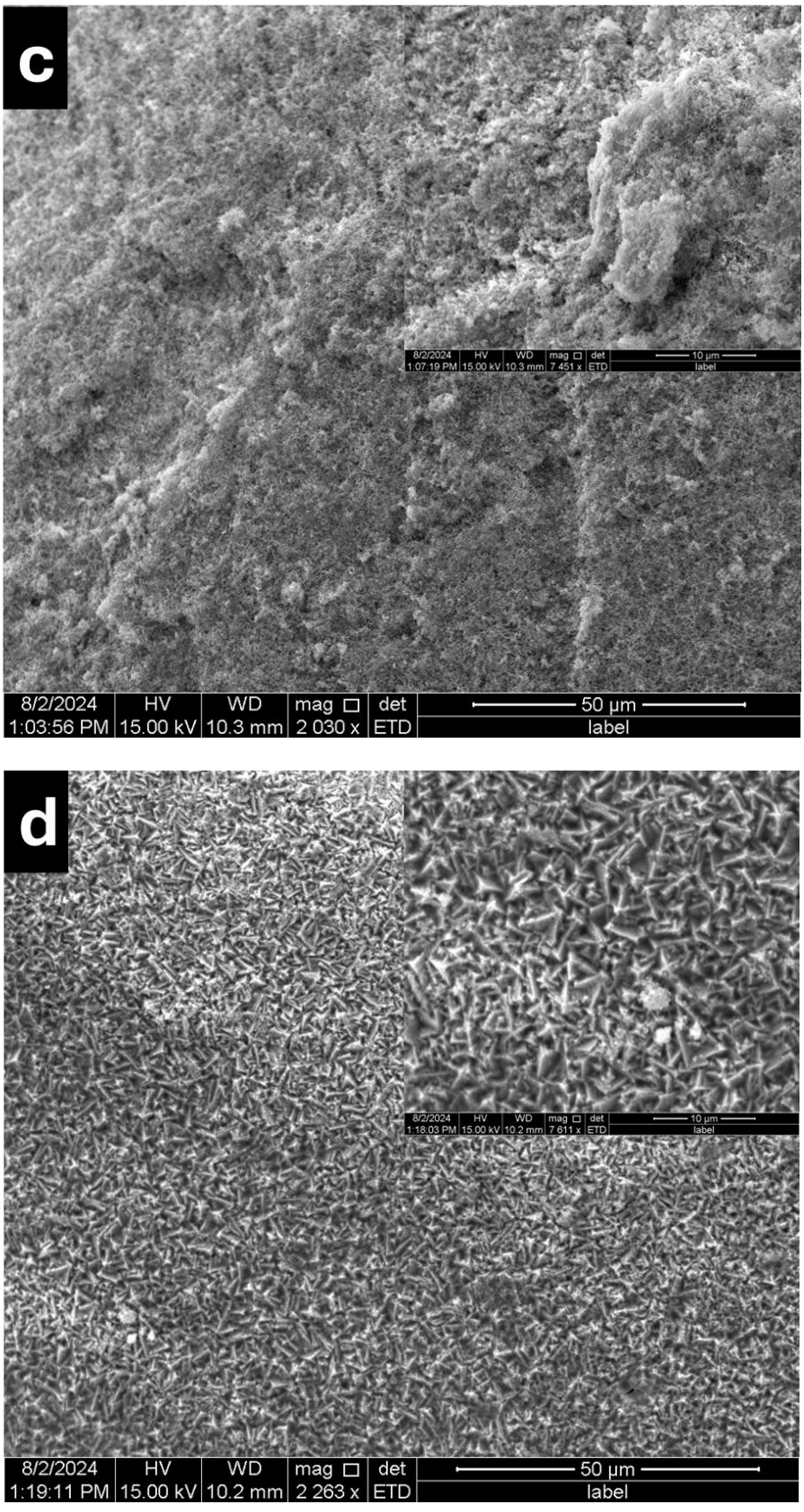

Fig. 6. Surface morphology of the Zn-Fe-W alloy coatings electrodeposited on the steel substrate with $(NH_4)_2SO_4$ base galvanic bath at: (a) 10; (b) 15; (c) 20 and (d) 25 mA cm^{-2}.

4.4 The influence of plating bath composition and current density on coating's composition

4.4.1 Zn-Fe-Mo

In Figure 7. Energy Dispersive X-ray Spectroscopy (EDXS) analysis quantified the average concentrations of iron and molybdenum across selected regions of the alloy surface. The results indicate that the electrodeposition of Zn-Fe-Mo alloys from a plating solution $(NH_4)_2SO_4$ base galvanic bath facilitates enhanced co-deposition of molybdenum. At applied current densities of 10 and 15 mA cm^{-2}, the deposits exhibited a molybdenum content ranging from 3 to 5 wt.%. However, increasing the current density to 20–25 mA cm^{-2} led to a marked decrease in molybdenum content to below 1 wt.%, accompanied by an increase in iron content, reaching approximately 12.2 wt.% at 25 mA cm^{-2}. This behavior is attributed to the pH-dependent speciation of molybdenum. At approximately pH 5.5, molybdenum primarily exists as mono-oxyanions, which possess a smaller ionic radius and thus exhibit enhanced electrodeposition kinetics[115]. The buffering capacity of ammonium ions (NH_4^+) maintains the bath pH near 5.7, thereby providing an optimal environment for the efficient reduction and incorporation of molybdenum into the alloy matrix. Furthermore, EDXS data reveal that the incorporation of both Fe and Mo is significantly higher in coatings derived from ammonium-containing electrolytes compared to those from ammonium-free solutions. This suggests the possible formation of electrochemically active complexes such as Fe–ammonia, Fe–citrate, Mo–ammonia, and Mo–citrate in the plating bath, which may undergo facile reduction at the cathode surface. In contrast, under similar electrodeposition conditions with a Na_2SO_4 base galvanic bath, the same compositional trend persists, although with substantially reduced molybdenum content of less than 1 wt.%. These findings underline the critical influence of electrolyte composition on the resulting alloy microstructure and elemental distribution.

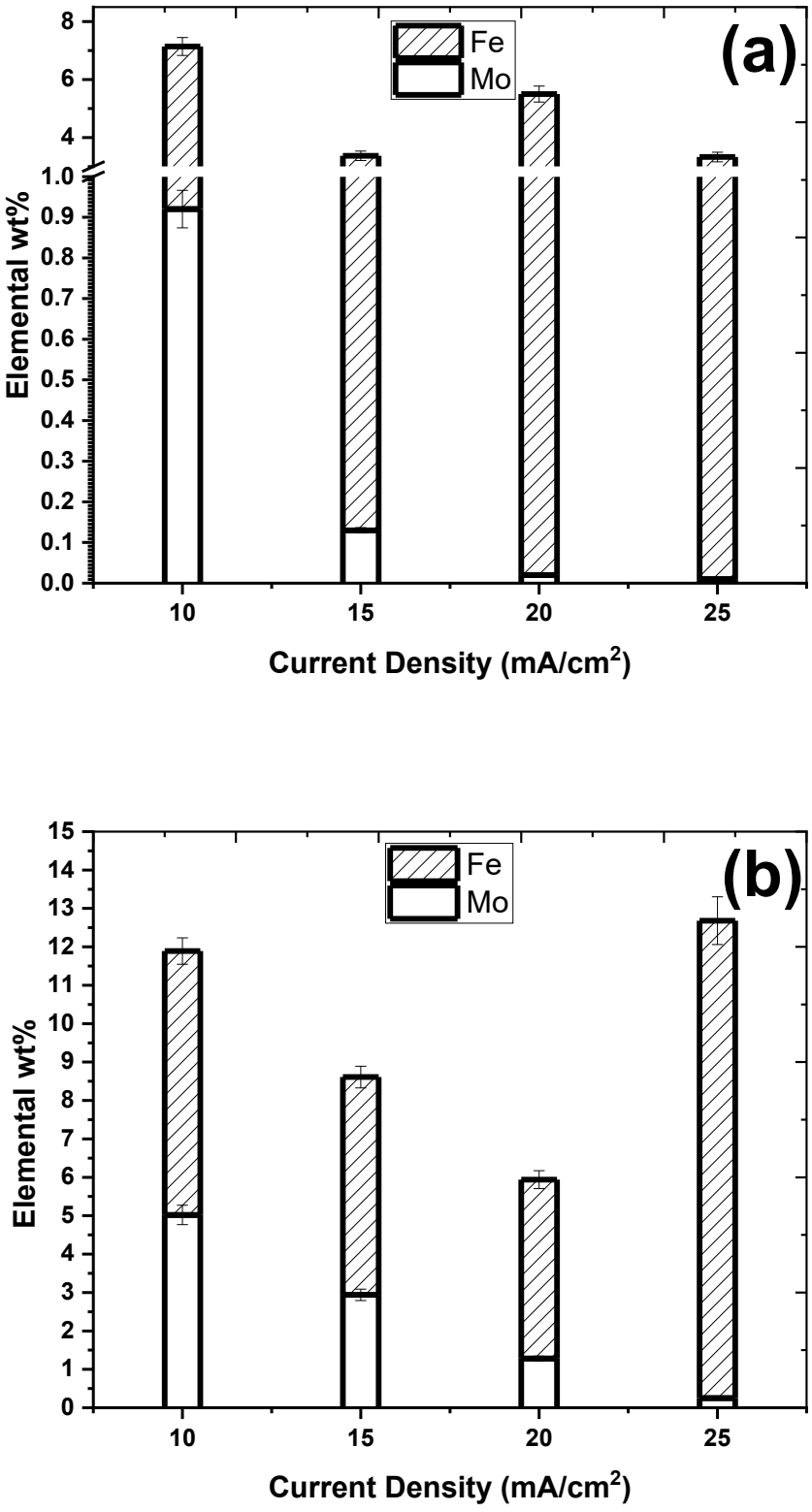

Fig. 7. Results of EDXS analysis of copper sample electroplated with Zn-Fe-Mo alloy coatings from (a) Na_2SO_4 and (b) $(NH_4)_2SO_4$ base galvanic baths at different current densities.

4.4.2 Zn-Fe-W

In Figure 8, the EDXS results yielded an average concentration of iron (Fe) and tungsten (W) on the surface of the Zn-Fe-W coatings, which helped to evaluate how current density and bath composition affect alloy incorporation. The results show that electrodeposition using the $(NH_4)_2SO_4$ base galvanic is indeed favorable to the incorporation of W (Fig. 8b). With an increase in current density values to 10, 15, and 20 mA cm^{-2}, an increase in W concentration is observed, which varied between 3 and 5 wt.%. However, with an increase in bath current density to 25 mA cm^{-2}, a sharp decrease is noted to about 1 wt.%, which is accompanied by an increase to about 11 wt.% Fe. This indicates an increase in preferential Fe reduction with respect to W at higher values of current density due to kinetic constraints during electrodeposition processes[116].

The role of ammonium ions (NH_4^+) present in the plating bath is very important in incorporating W into the deposit. The pH level of the bath remained relatively constant at 5.7 during the deposition, which is well known to favor W incorporation into Zn-based alloy deposits. This can particularly be justified on the basis of the preferential formation of reducible metal-ammine and metal citrate complexes such as Fe-NH_3, Fe-Citrate, W-NH_3, and W-Citrate species. The role of these species is to enhance metal availability on the electrode surface and their consequent electrochemical reduction, hence improving metal incorporation during electrodeposition[117] . As a result, Fe and W concentrations are significantly higher within films deposited using electrolytes containing ammonium ions compared to those deposited using electrolytes free from ammonium ions. A similar behavior concerning Fe and W incorporation is also observed in Na_2SO_4 base galvanic bath (Fig. 8a), although it should be noted that there is a significantly lower amount of W (less than 1 wt.%) present in this case, which is consistent with our hypothesis regarding the positive effect exerted by NH_4^+ on W incorporation. Taken together, these EDXS results show a clear dependence on electrolyte composition, particularly on ammonium ion incorporation, on Fe and W alloying element concentration within Zn-Fe-W films.

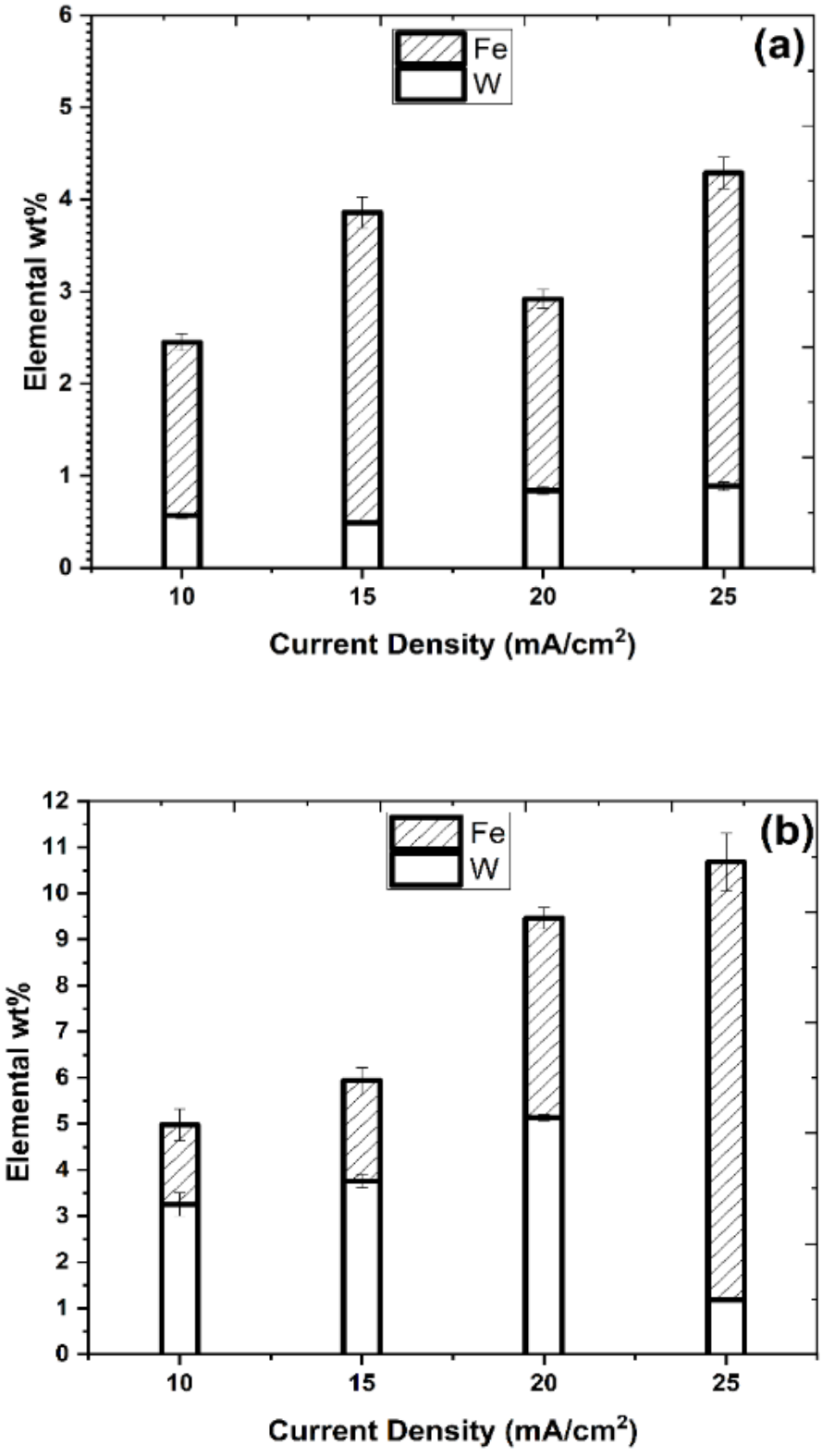

Fig. 8. Results of EDXS analysis of copper sample electroplated with Zn-Fe-W alloy coatings from (a) Na_2SO_4 and (b) $(NH_4)_2SO_4$ base galvanic baths at different current densities.

4.5 The influence of plating bath composition and current density on coating's topography

4.5.1 Zn-Fe-Mo

In Figure 9, the surface topography of the Zn-Fe-Mo alloy coatings is considerably affected by both the composition of the plating solution and the cathodic current density used in electrodeposition. Specifically, the presence or absence of ammonium ions in the electrolyte is of the most significance in developing the average surface roughness (Ra) of the coatings. The coatings developed from Na_2SO_4 base galvanic bath showed Ra values of 0.56 µm, 0.75 µm, 0.041 µm, and 0.035 µm at current densities of 10, 15, 20, and 25 mA cm^{-2}, respectively. On the other hand, the coatings obtained from solutions containing ammonium ions showed Ra values of 0.76 µm, 0.17 µm, 0.091 µm, and 0.048 µm under the same current densities. The findings exhibit a distinct trend for surface roughness to decline with current density irrespective of bath composition, with the highest changes being observed at lower current densities. Higher Ra values at lower current densities can be attributed to a variety of interrelated reasons. First and foremost, lower current densities tend to produce less uniform metal deposition and nucleation, hence resulting in rough surface topographies. The lack of good throwing power of the electrolyte under these conditions results in local deposition and hence enhances roughness. With further lowering of current densities often resulting in bigger grain size and therefore rough coatings, increasing current density to 20 and 25 mA cm^{-2} results in decreased surface roughness highly significantly, indicating a shift to finer-grained, denser, and homogeneous coatings. The enhancement in smoothness here can best be described by enhanced deposition kinetics and more uniform metal ion reduction at higher current densities. Furthermore, the plating bath containing ammonium ions $(NH_4)_2SO_4$ base had the tendency to produce smoother coatings in the mid-to high current density regime than the bath without ammonium. This effect can be attributed to ammonium ion's buffering ability, which has a tendency to keep the neighborhood pH near to that at the cathode steady. This steady pH value can promote deposition conditions by preventing sharp changes in the electrochemical environment, and thus promoting sustained nucleation and grain growth. In conclusion, this work asserts the role of electrolyte composition as well as deposition conditions in controlling the surface morphology of Zn-Fe-Mo coatings, as necessitated by optimum functionality in applications requiring smooth surfaces with minimum roughness.

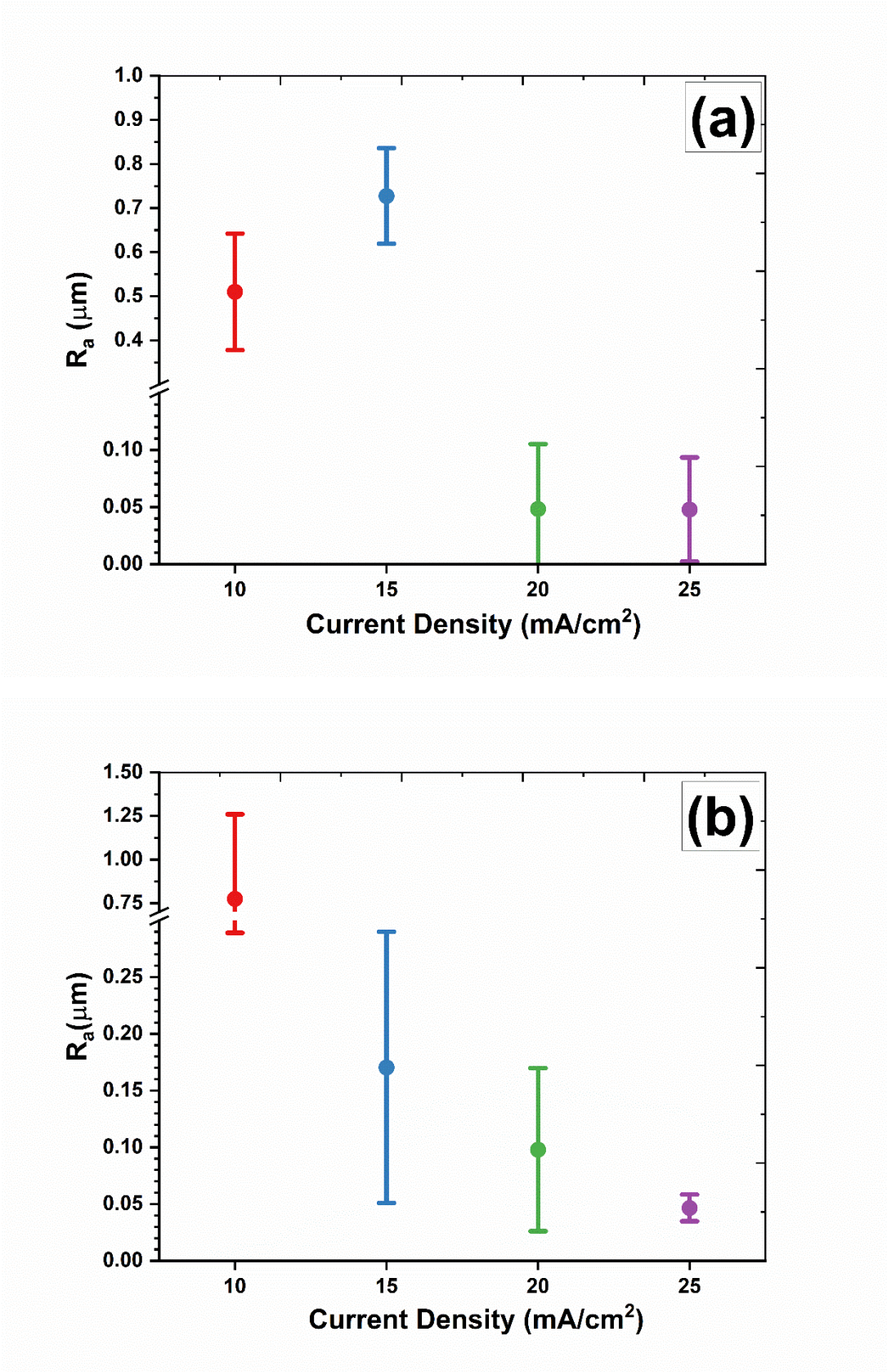

Fig. 9. Average roughness (Ra) of the steel sample electroplated with Zn-Fe-Mo alloy coatings of (a) Na_2SO_4 and (b) $(NH_4)_2SO_4$ base galvanic baths at different current densities.

4.5.2 Zn-Fe-W

In Figure 10, both the chemical composition of the plating bath and the cathodic current density applied during deposition strongly influence the morphology of the electrodeposited coatings. Coatings deposited from Na_2SO_4 base galvanic baths (Fig. 10a) had average surface roughness values of 1.25 µm, 1.18 µm, 0.28 µm, and 0.20 µm at current densities of 10, 15, 20, and 25 mA cm^{-2}, respectively. In comparison, the coatings deposited from the $(NH_4)_2SO_4$ ammonium-based baths (Fig. 10b) exhibited lower roughness with Ra values of 0.94 µm, 0.62 µm, 0.25 µm, and 0.15 µm at the respective same current densities mentioned above. Notably, at higher current densities, say at 20 and 25 mA cm^{-2}, the differences in roughness between the two types of baths become relatively very small, indicating convergence in their surface morphology as deposition becomes more kinetically driven.

The relatively high roughness of both electrolytes at the lower current densities (10–15 mA cm^{-2}) may be related to a number of interrelated factors, which include increased surface irregularities generated during nucleation at slower rates, reduced throwing power leading to non-uniform metal ion distribution, and non-uniform growth of deposit grains. All of these conditions favor the nucleation of coarse, porous, and structurally inconsistent coatings, which are reflected as high Ra values. When the current density increases, the deposition rate increases, and the nucleation becomes more uniform, thus yielding smoother and more compact coatings characterized by an Ra value that is significantly lower. This trend underlines the important contribution of deposition kinetics in determining the final surface characteristics of the alloy layers.

From a practical point of view, this higher roughness for lower current densities is very important, since such morphological features may introduce voids, microdefects, or sites of stress concentration within the coating. These defects can have a negative effect on the long-term performance of the coating by reducing adhesion, increasing susceptibility to wear, and generally diminishing durability. For this reason, optimization of the current density and bath chemistry is necessary to obtain coatings with desirable surface integrity and improved functional properties.

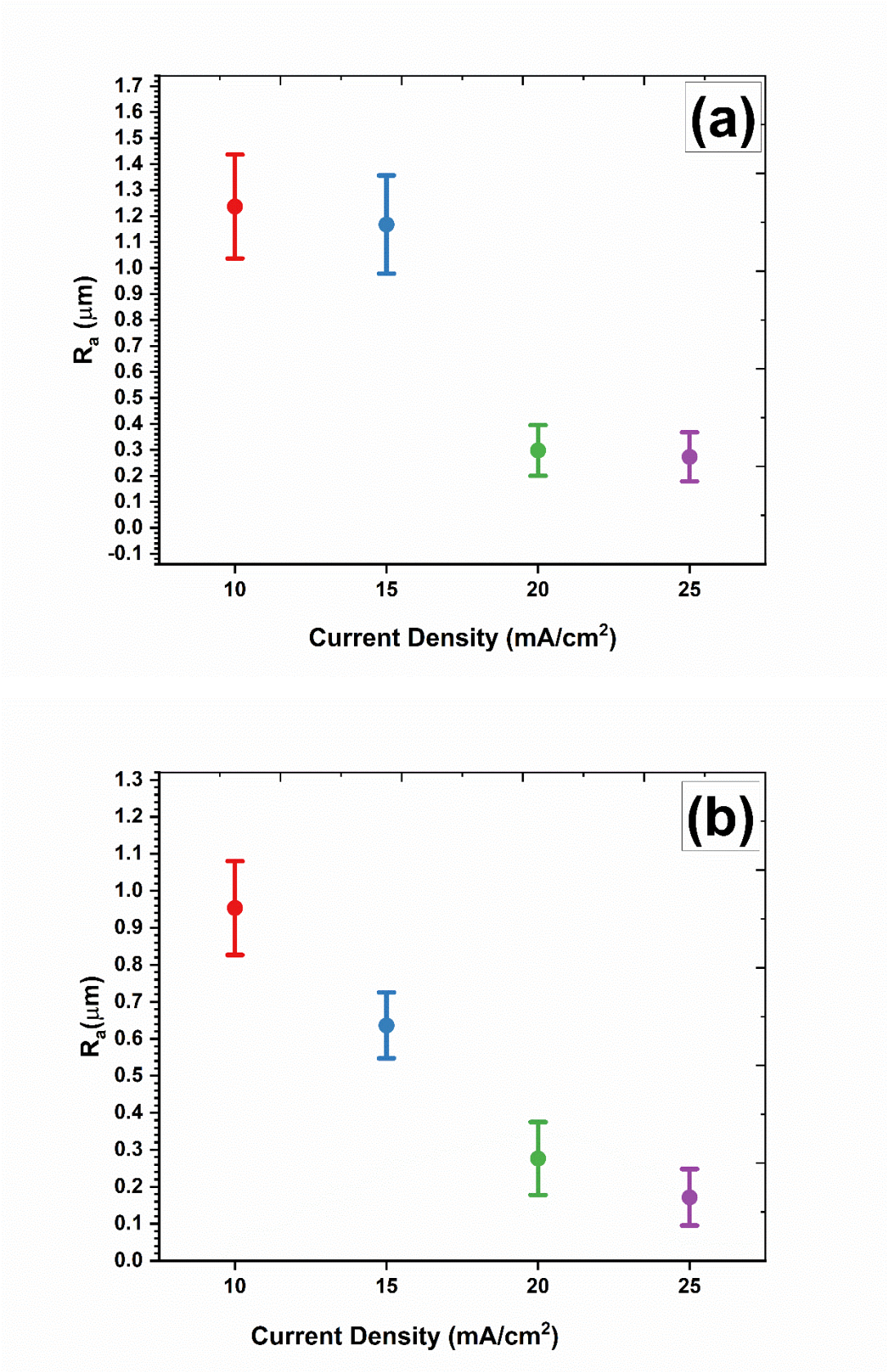

Fig. 10. Average roughness (Ra) of the steel sample electroplated with Zn-Fe-W alloy coatings of (a) Na_2SO_4 and (b) $(NH_4)_2SO_4$ base galvanic baths at different current densities.

4.6 The influence of plating bath composition on coating's structure

4.6.1 Zn-Fe-Mo

In Figure 11, to gain more understanding about the microstructure in the coatings, Transmission Electron Microscopy (TEM) was performed for some selected samples plated at 20 mA cm^{-2} from both of the two different types of plating baths the one containing Na_2SO_4 and the other one containing $(NH_4)_2SO_4$ as supporting electrolyte. For the coating plated from the Na_2SO_4 base bath, cross-sectional TEM imaging (Fig. 11a) exhibited sharp columnar growth pattern. This microstructure consisted of fiber-like or bead-like parallel arrangements of oval-shaped nanocrystallites between about 20 and 40 nm. The Selected Area Electron Diffraction (SAED) pattern (Fig. 11c) revealed the polycrystalline nature along with the absence of strong crystallographic texture, indicating that the crystallites are orientated in a random fashion.

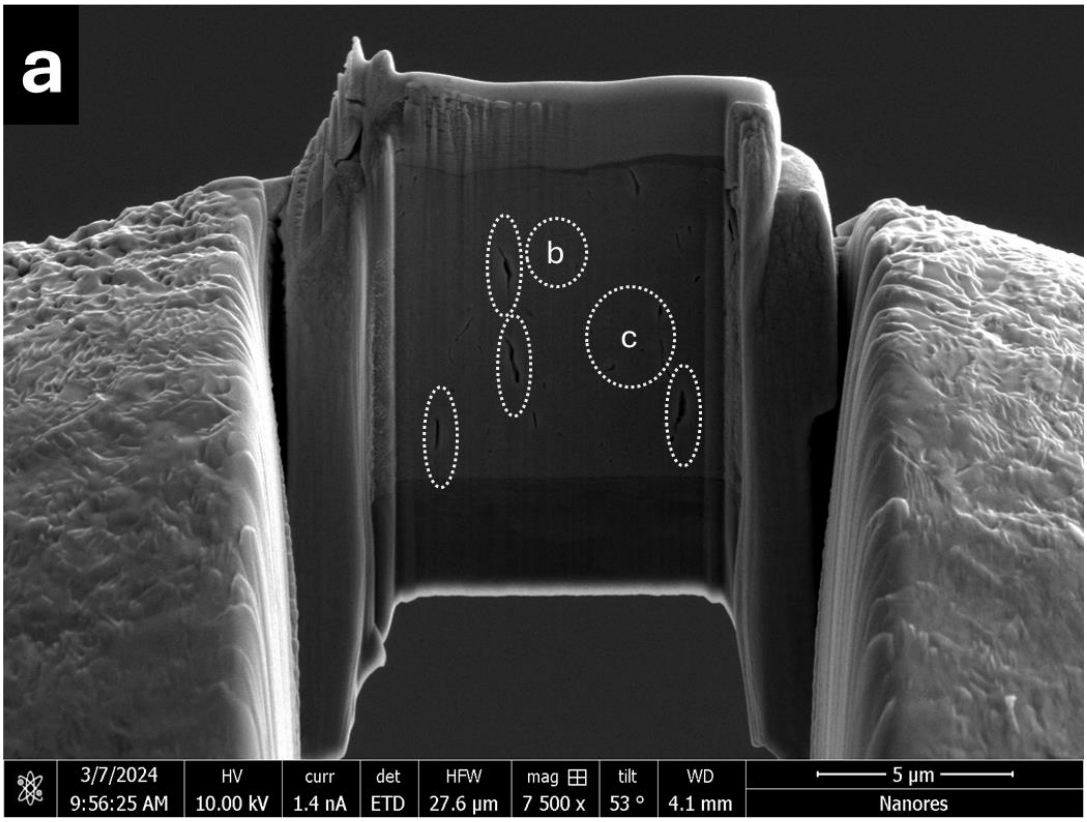

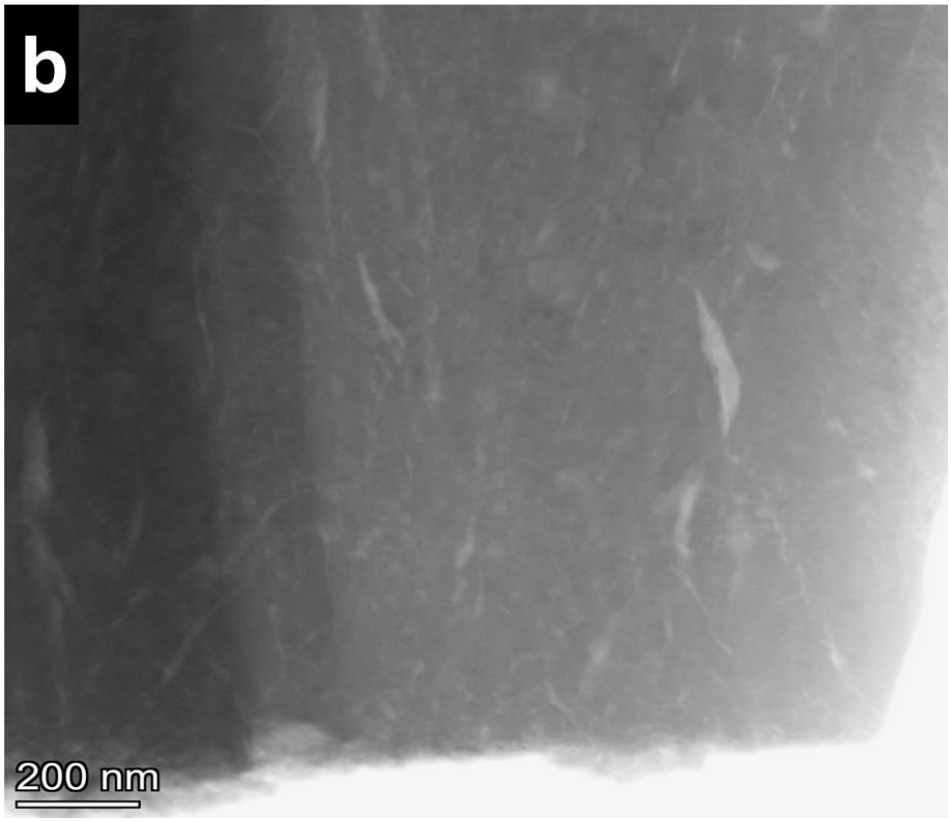
b
200 nm

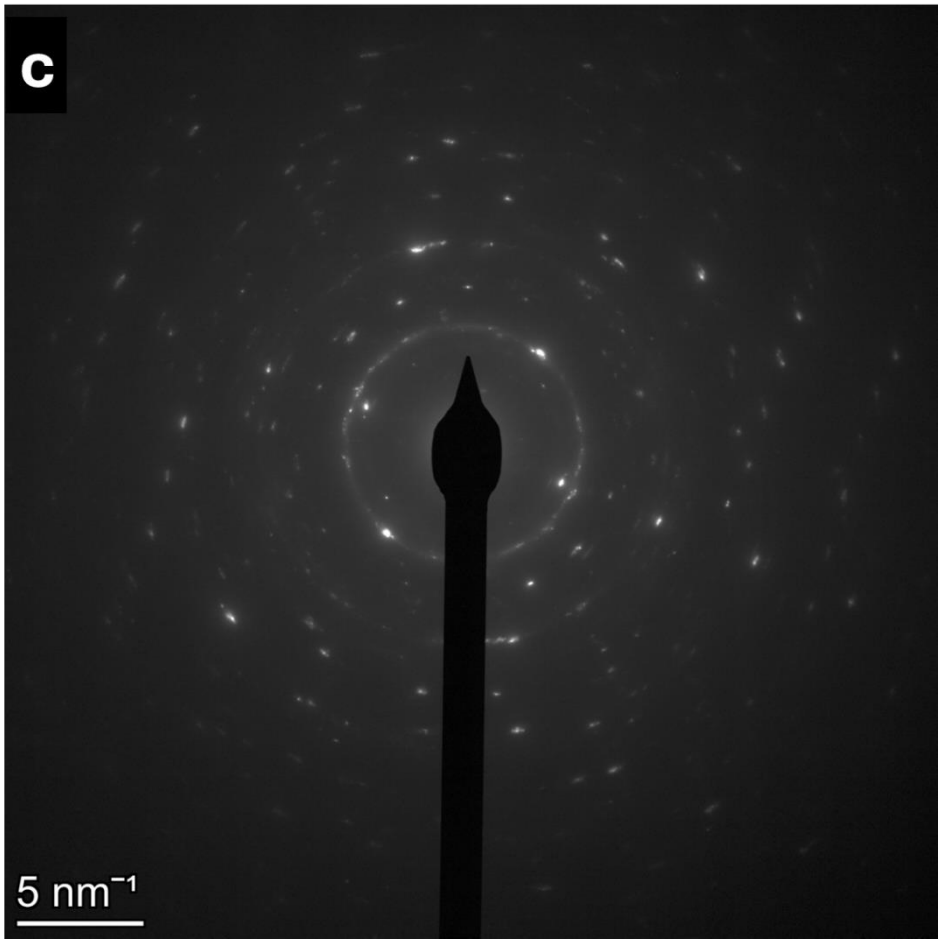
c
5 nm⁻¹

Fig. 11. Structure of Zn-Fe-Mo alloy coating deposited from plating bath containing Na_2SO_4 at 20 mA cm^{-2} at 25 °C. The appearance of the lamella with marked imaging and diffraction areas (a), STEM HAADF structure (b) and SAED diffraction pattern (c).

In contrast, the coating deposited from the ammonium sulfate bath exhibited a thickness of around 7 μm as in Fig. 12a, and a uniform nanocrystalline microstructure throughout the entire cross-section. TEM examination provided the same columnar mode of growth, with interpenetrating nanofibers of elliptical crystallites, again in the size range of 20–40 nm (Fig. 12b). Surprisingly, this sample exhibited bright, nanometric areas spread throughout the matrix of the TEM images. These areas are not pores, but can be accounted for by local electron density gradients, possibly as a result of microstructural heterogeneity or small compositional variations. Notably, the size and density of these areas decrease near the steel/coating interface, indicating a more dense structure towards the substrate. As shown in Fig. 12c, the SAED pattern (polycrystalline ring pattern) of the sample showed strong texturization, showing that grains formed in ammonium-rich conditions have preferred crystallographic orientations.

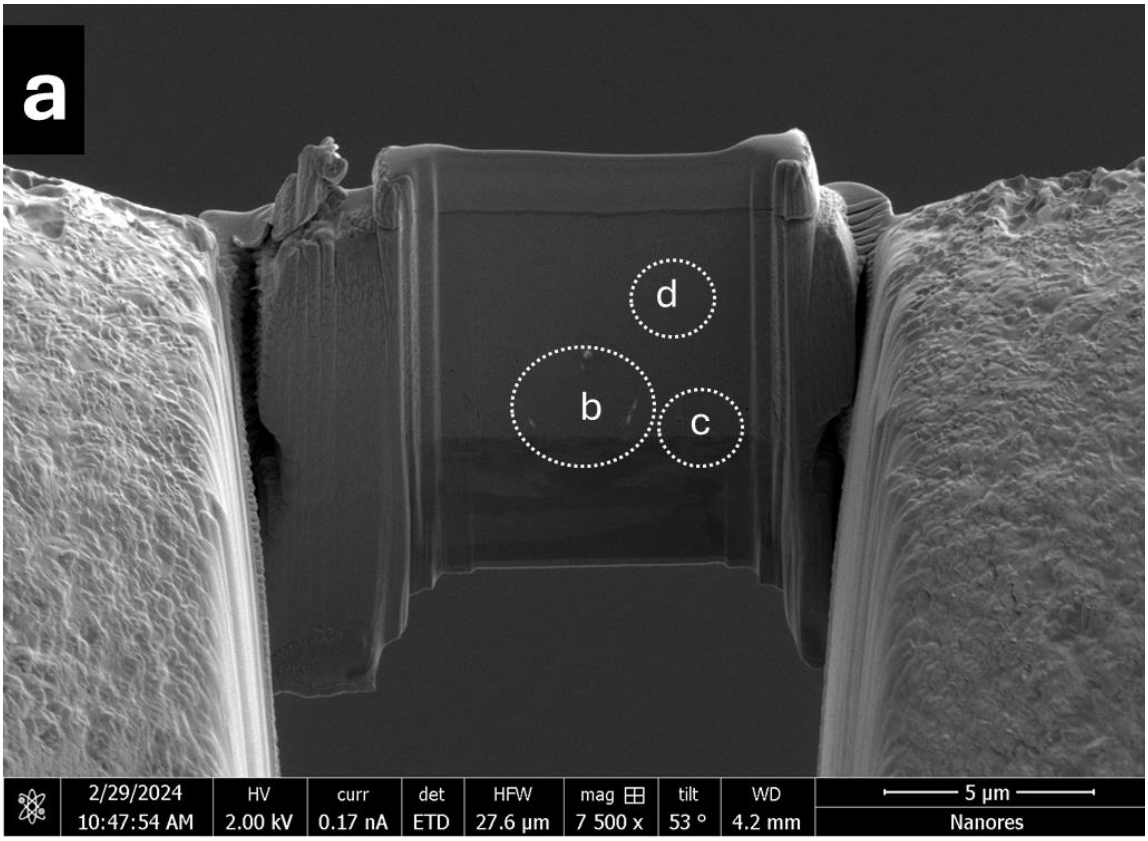

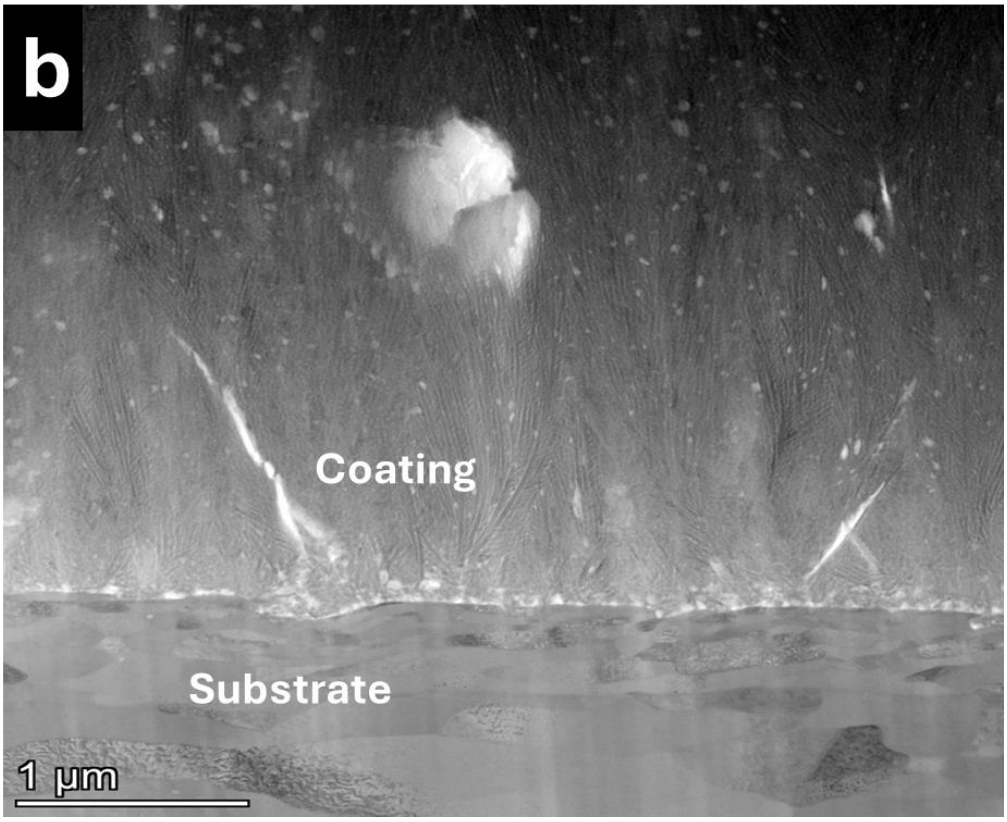
b
Coating
Substrate
1 µm

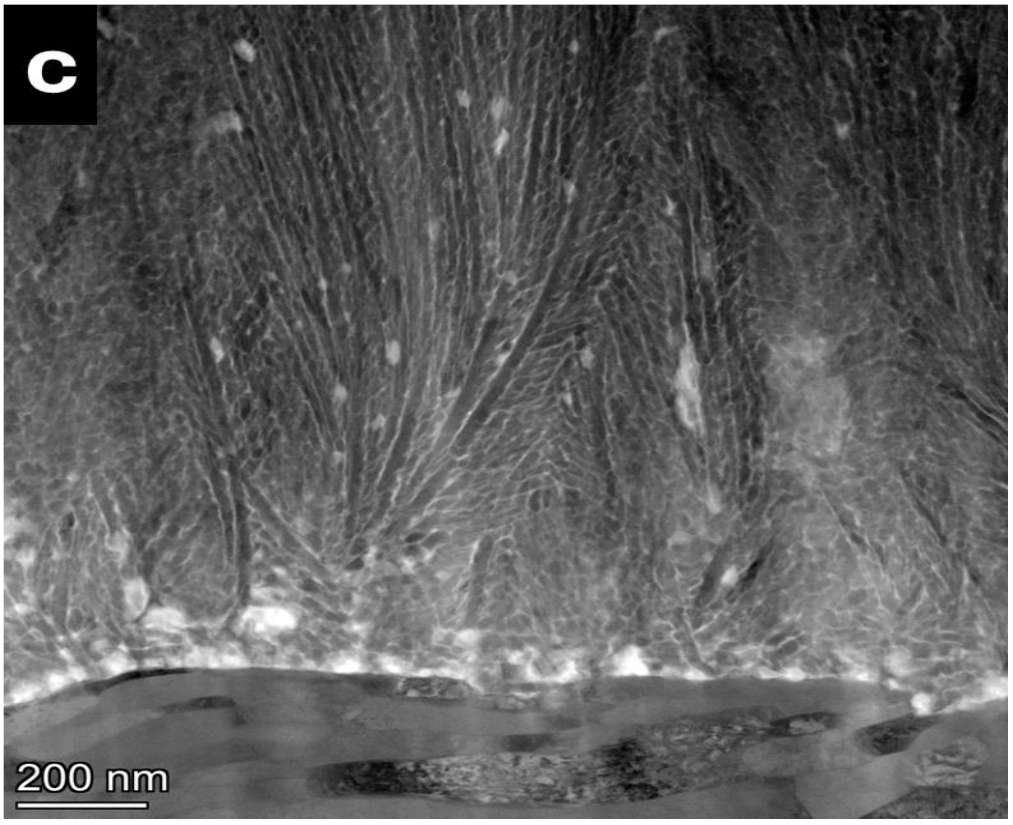
c
200 nm

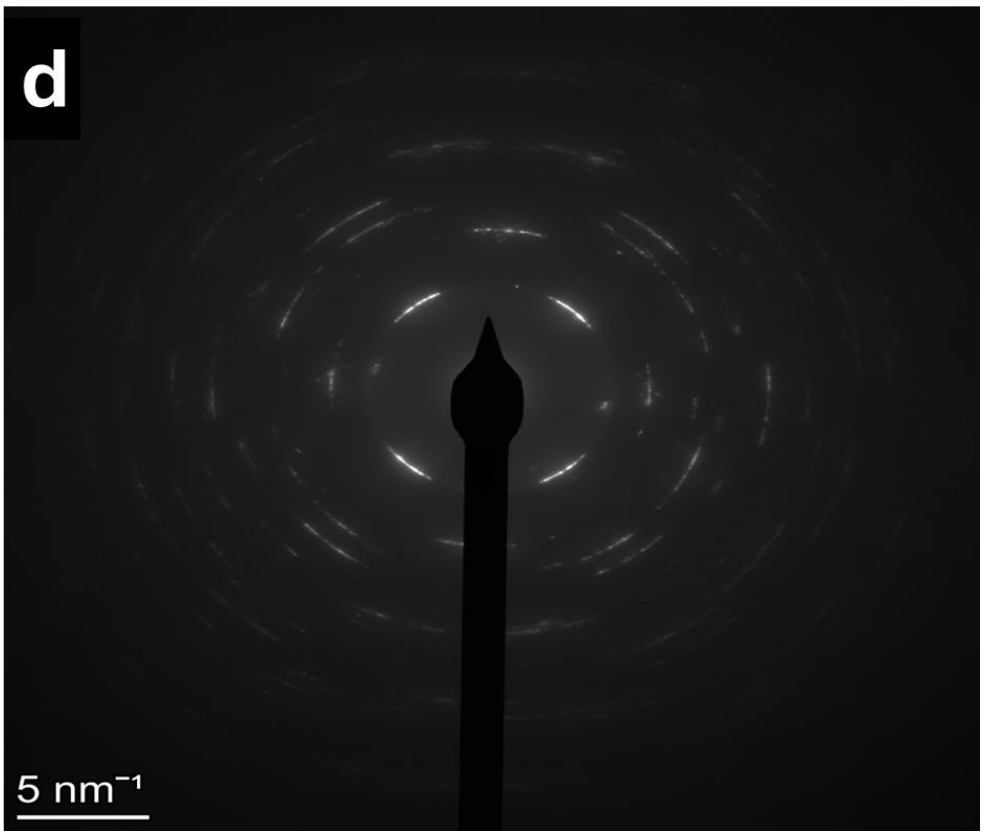

Fig. 12. Structure of the Zn-Fe-Mo alloy coating deposited from a plating bath containing $(NH_4)_2SO_4$ at 20 mA cm^{-2} at 25 °C. The appearance of the lamella with marked imaging and diffraction areas (a), STEM HAADF structure (b,c) and SAED diffraction pattern (d).

Additional information was obtained from Energy-Dispersive X-ray Spectroscopy (EDS) elemental mappings, which showed uniform distributions of the major alloying elements the zinc, iron, and molybdenum with increasing coating thickness (Fig. 13). The elemental mappings also showed microscopic compositional inhomogeneities. Specifically, areas relatively lean in zinc showed corresponding spikes in iron and molybdenum content, suggesting competitive co-deposition and the occurrence of a multiphase alloy structure. This elemental substitution is consistent with variable electrodeposition behavior among metals involved and suggests that galvanic and kinetic effects locally occurring upon the deposition process are accountable for phase separation or grain boundary enrichment in these sites.

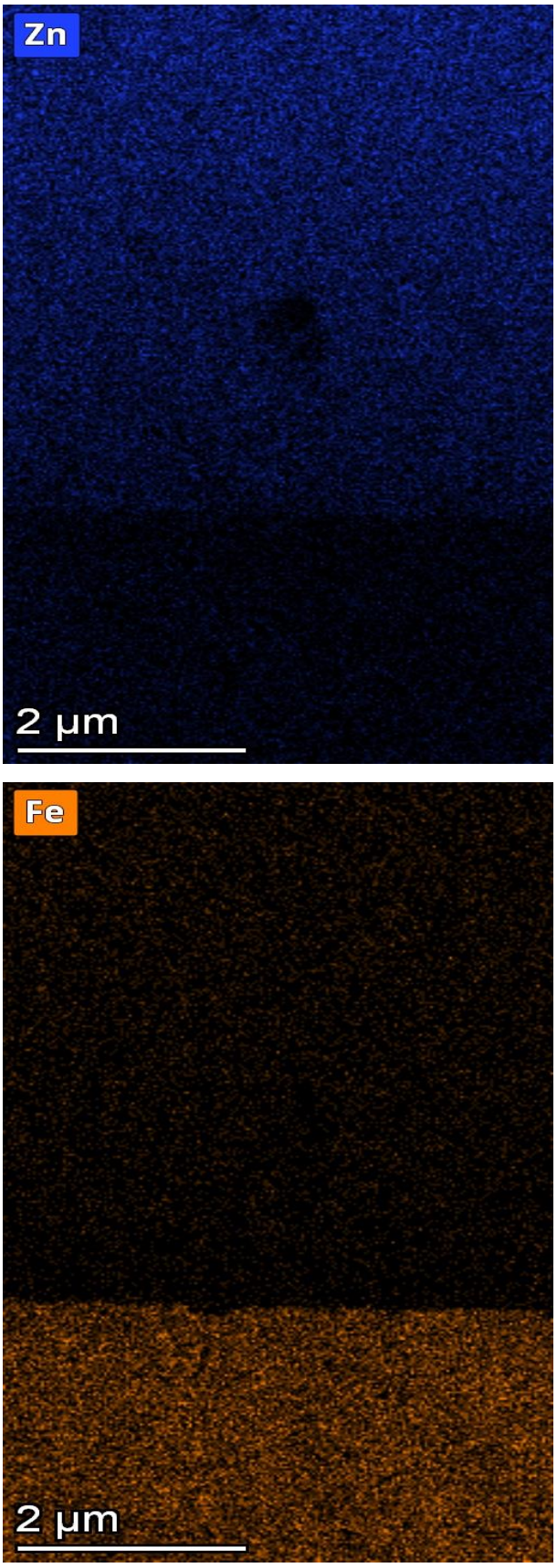
Zn
2 µm
Fe
2 µm

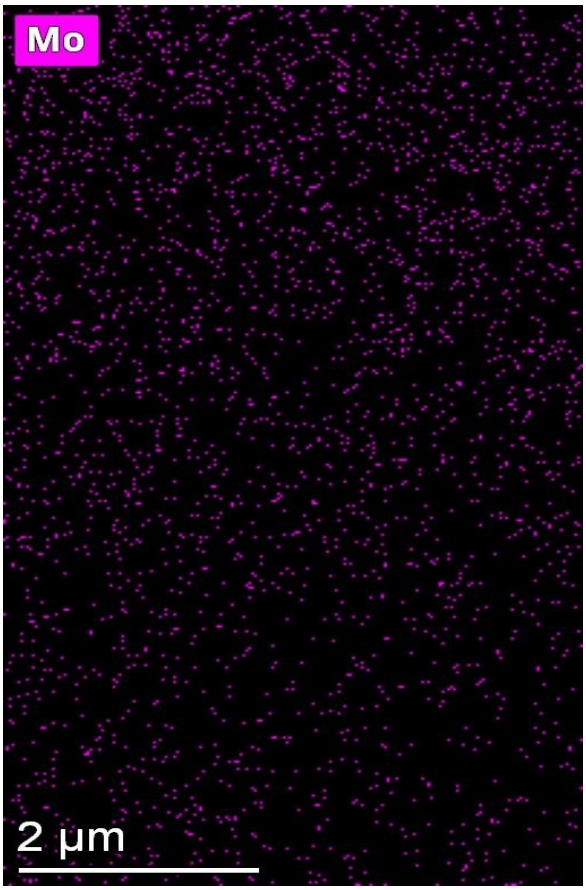

Fig. 13. Distribution of the alloying elements across the Zn-Fe-Mo alloy coating deposited from plating bath containing $(NH_4)_2SO_4$ at 20 mA cm^{-2} at 25 °C. Zn-poor areas corresponds to regions with more Fe and Mo.

Briefly, extensive microstructure and compositional analyses confirm that both the support electrolyte choice and the applied current density greatly affect not only the surface morphology but also the internal structure, phase distribution, and crystallographic orientation of the Zn-Fe-Mo alloy coatings. The introduction of ammonium ions into the electrolyte appears to induce more regular crystallite ordering and closer nanostructure development by buffering pH levels as well as stabilizing metal complexes by electrodeposition.

4.6.2 Zn-Fe-W

In Figure 14, for a better understanding of the microstructure within the layers deposited, Scanning Electron Microscopy (SEM) with Focused Ion Beam (FIB) sectioning was carried out on samples deposited at 20 mA cm^{-2} with a thickness of almost 14 µm using both electrolytes being investigated. The utilization of this analytical tool helps to ascertain information concerning coating density, grain orientation, interfaces, and defects within the layers that cannot otherwise be observed.

The FIB sectioning images show that, within the coating obtained from the Na_2SO_4 containing bath, there is a more or less continuously varying structure that transitions from a columnar grained structure close to the interface to a more equiaxed-grained structure further out into the coating thickness. A dark, irregular band is noted close to the coating interface, together with a number of smaller isolated dark regions that are both at the interface and slightly off into the coating thickness. These dark features could represent regions of microvoiding at/near interfaces due to initial stages of nucleation processes. Their sizes and numbers are more consistent with early nucleation features and initial metal layering rather than with any indication that there is considerable thickness delamination within these regions. This is also what one expects within Zn-Fe-type deposits obtained from sulphate-electrolyte solutions, which tend to grow more uniform films but can still contain small interface irregularities due to inhomogeneities during initial layering processes.

The presence of microcracks and small-scale voids within the Zn-based coating is also an indication of hydrogen incorporation during electrodeposition, which is well known to occur during this type of metal deposition. Hydrogen evolution on the surface of the cathode can result in hydrogen being trapped within the deposited metal matrix, causing internal stress that can finally result in microvoids and/or microcracks being introduced within this coating layer [45], [118]. These defects, though unavoidable to some extent, significantly influence the coating durability.

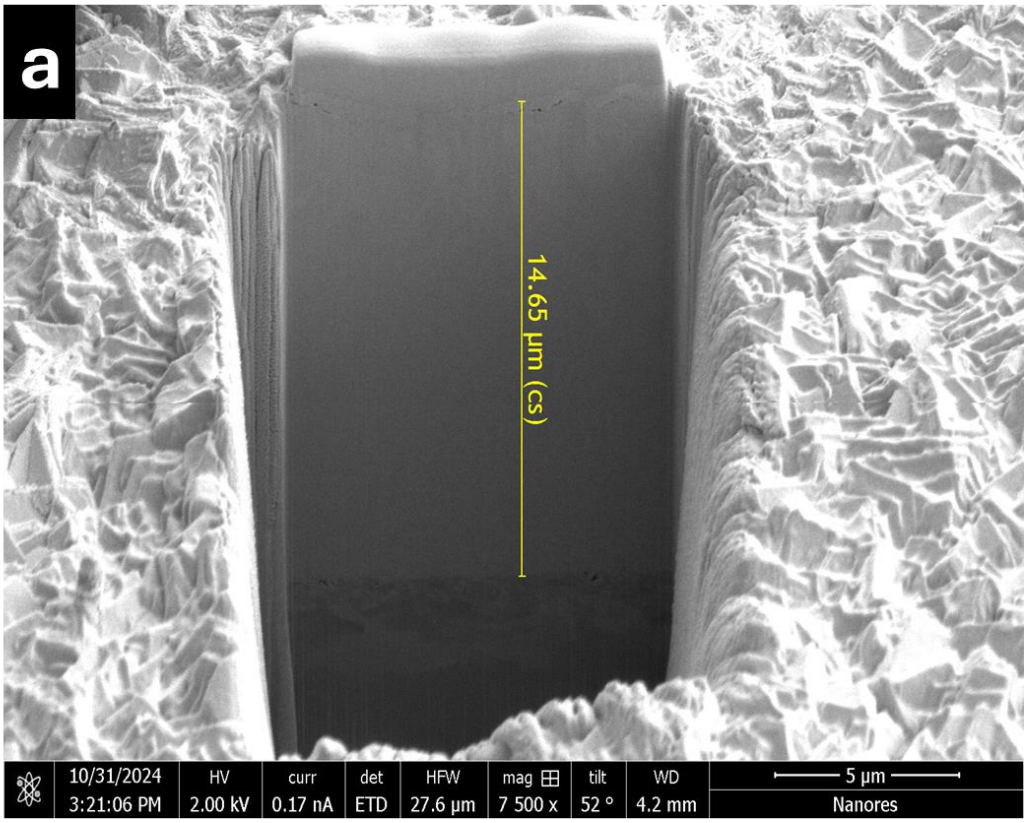
a
14.65 µm (cs)
10/31/2024
3:21:06 PM
HV
2.00 kV
curr
0.17 nA
det
ETD
HFW
27.6 µm
mag
7 500 x
tilt
52 °
WD
4.2 mm
5 µm
Nanores

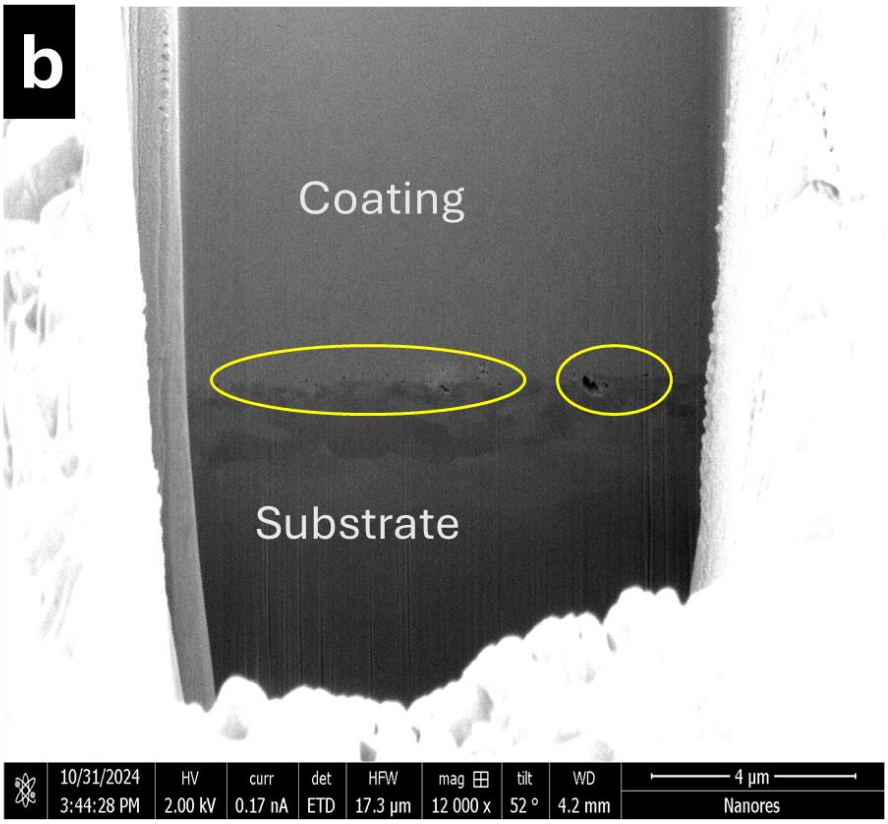
b
Coating
Substrate
10/31/2024
3:44:28 PM
HV
2.00 kV
curr
0.17 nA
det
ETD
HFW
17.3 µm
mag
12 000 x
tilt
52 °
WD
4.2 mm
4 µm
Nanores

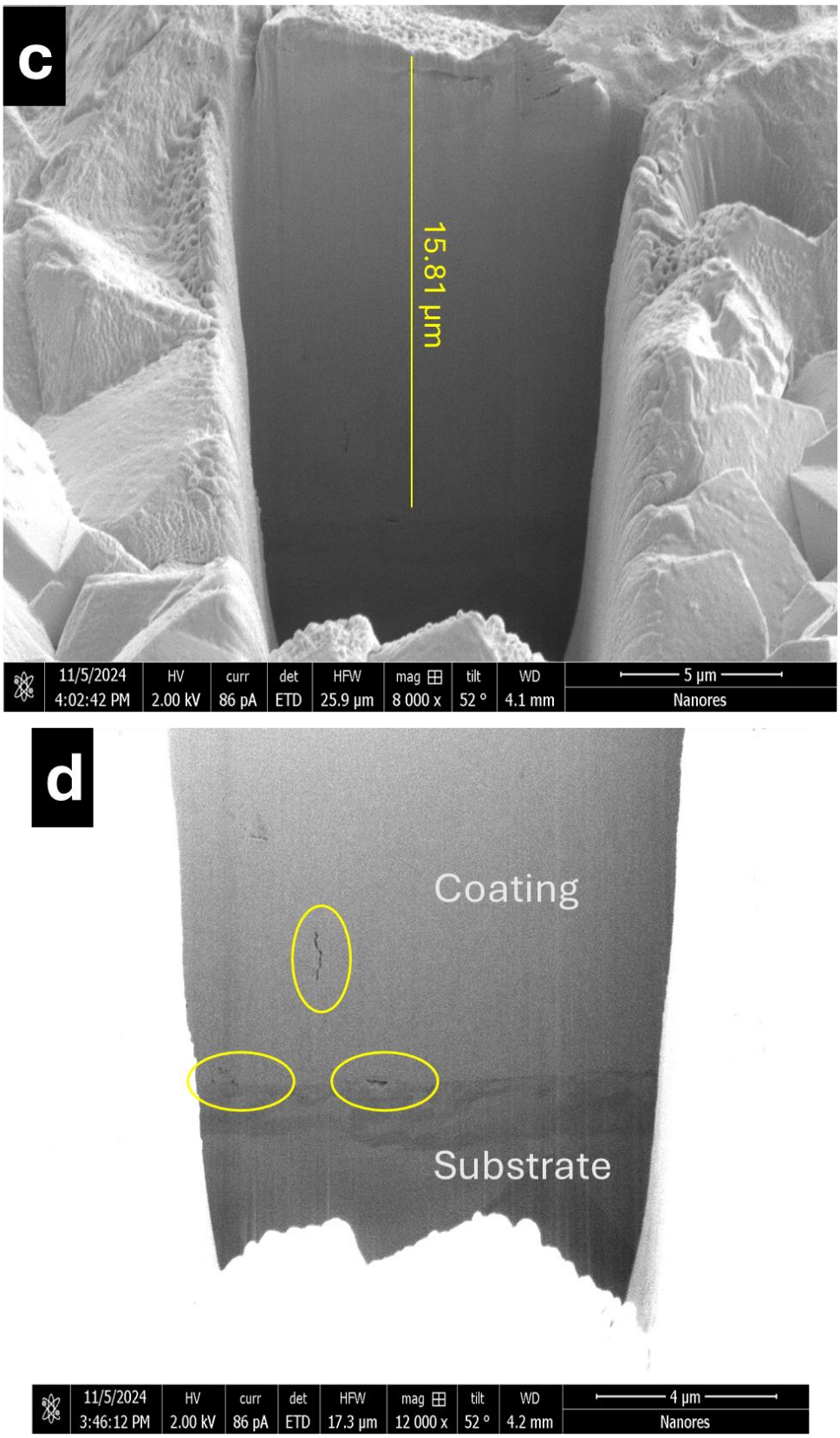

Fig. 14. Cross-sectional structure of the Zn-Fe-W alloy coating deposited from the plating bath containing (a) Na_2SO_4 (b) $(NH_4)_2SO_4$ at 20 mA cm^{-2} at 25 °C.

On the other hand, coating derived using the ammonium sulfate electrolyte $(NH_4)_2SO_4$ still remained at about 15.8 µm thick, indicated in this corresponding cross-sectional microscope image specific to the 20 mA cm^{-2} plated specimens. The micro-scale morphology generally presented uniformity across each coating layer, but featured a visible region within which there is localized porosity within close proximity to regions directly across from the interfaces to the substrate surface of each deposited layer. This localized porosity is visualized within irregular regions dispersed multifariously across regions where the said interfaces exist, and this particular morphology indicates that the said regions typically form because of hydrogen gas evolution within early-period electrodeposition processes specific to utilization within this electrolytic environment containing ammonium within said electrolytic medium.

The high level of porosity present at the interface is an indication that there is inefficient nucleation and/or wetting processes during the early stages of growth. This could serve to enhance microvoid formation, which can act as stress raisers, causing a possible degradation of adhesion, while simultaneously offering favored routes to diffusion, which could result in long-term failure of protection by the coating. Above this interface, the coating is relatively dense, having features that are both finely grained and showing strong columnar growth, typical of alloyed coatings deposited by electrodeposition.

The trapping of gas pockets and microvoids during the early stages of deposition is well-supported by hydrogen evolution mechanisms reported for ammonium-based electrolytes [119]. The hydrogen gas produced at the cathode can become trapped underneath the forming metal layer, resulting in isolated voids during the early stages of coating formation. The agglomerated and discontinuous dark pores present at the interface between the coating layer and the substrate confirm this hydrogen evolution mechanism, which is sensitive to electrolyte type and early-stage kinetics during metal coating deposition.

4.7 The influence of plating bath composition and current density on coating's phase composition

4.7.1 Zn-Fe-Mo

To study the crystallographic structure and phase composition of ternary Zn-Fe-Mo alloy coatings, X-ray diffraction (XRD) analysis was conducted on specimens synthesized at various current densities and bath chemistries. The diffractograms obtained as a result and presented in Figures 15 and 16 contain information on the influence of the deposition parameters on the microstructure of the coatings. For all the analyzed samples regardless of

deposition from Na_2SO_4 or $(NH_4)_2SO_4$ type plating baths well distinguished diffraction peaks that were related to the copper substrate were found consistently at 2θ angles of 43.2°, 50.4°, and 74.1°, compared with PDF Card No. 00-004-0836.

Phase composition of the coatings varied substantially with current density and bath composition. For deposited samples from the Na_2SO_4 containing electrolyte at lower current densities (10 and 15 mA cm^{-2}), the XRD patterns showed sharp and well-defined peaks corresponding to pure zinc and iron phases, as testified by their close similarity with PDF database cards 01-078-9363 (Zn), 01-076-6587 (Fe), and 01-071-4649 (Fe cubic). These sharp, well-defined peaks indicate relatively larger crystallite sizes and a more crystalline structure at lower deposition currents.

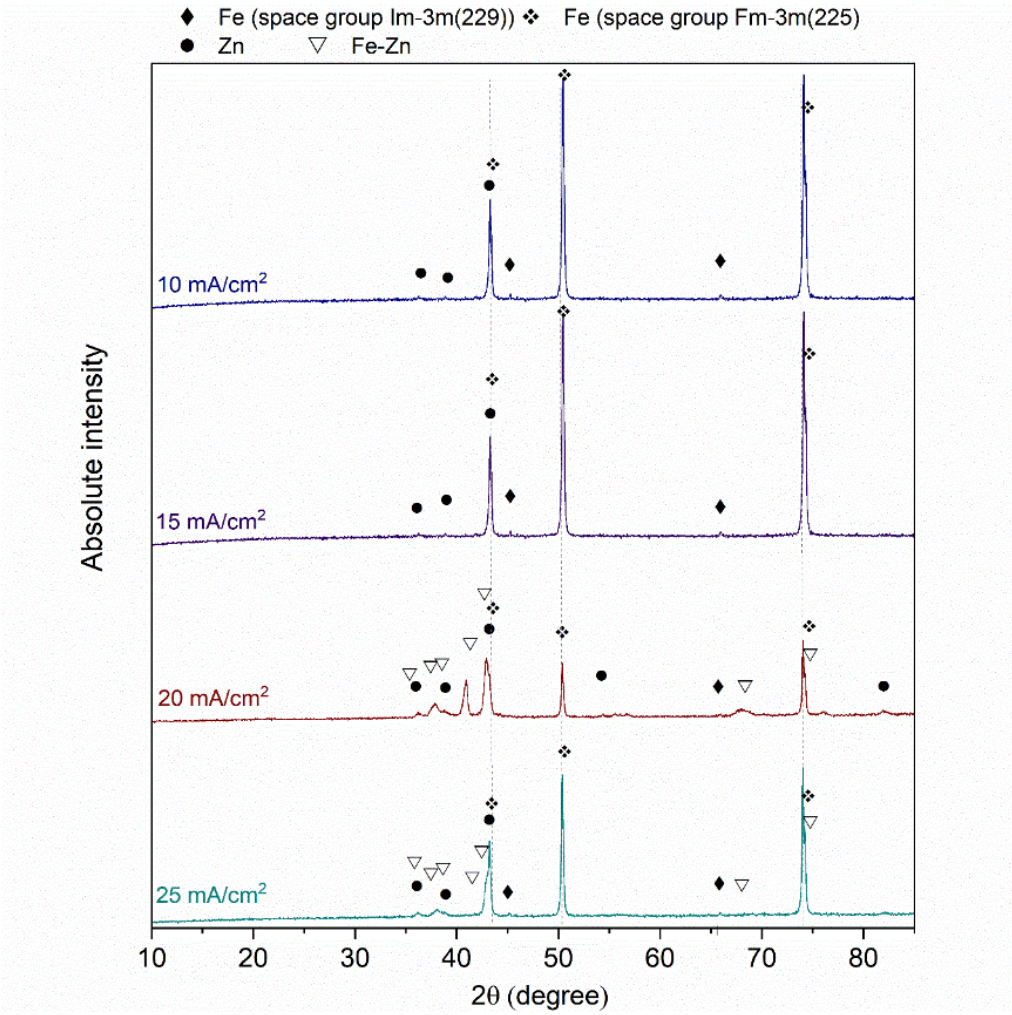

Fig. 15. Diffractograms of the samples with Zn-Fe-Mo alloy coatings deposited at different current density values with Na_2SO_4.

However, when the current density was increased to 20 and 25 mA cm^{-2}, there were significant changes in the diffraction patterns. The peaks of zinc and iron became weaker and wider, which is characteristic of nanocrystalline structures formed as a result of higher nucleation rates and reduced grain sizes under high current conditions. At such higher current densities, new peaks emerged corresponding to intermetallic Fe-Zn phases, reflecting the formation of complex alloyed structures. These were identified as $Fe_{22}Zn_{78}$ (PDF Card No. 01-071-8477), $Fe_{11}Zn_{40}$ (PDF Card No. 00-032-0478), and possibly $FeZn_{10.98}$ with hexagonal structure (PDF Card No. 00-045-1184). This transition from simple elemental phases to complex intermetallics is characteristic of increased metal ion co-deposition and solid-state diffusion at higher deposition rates.

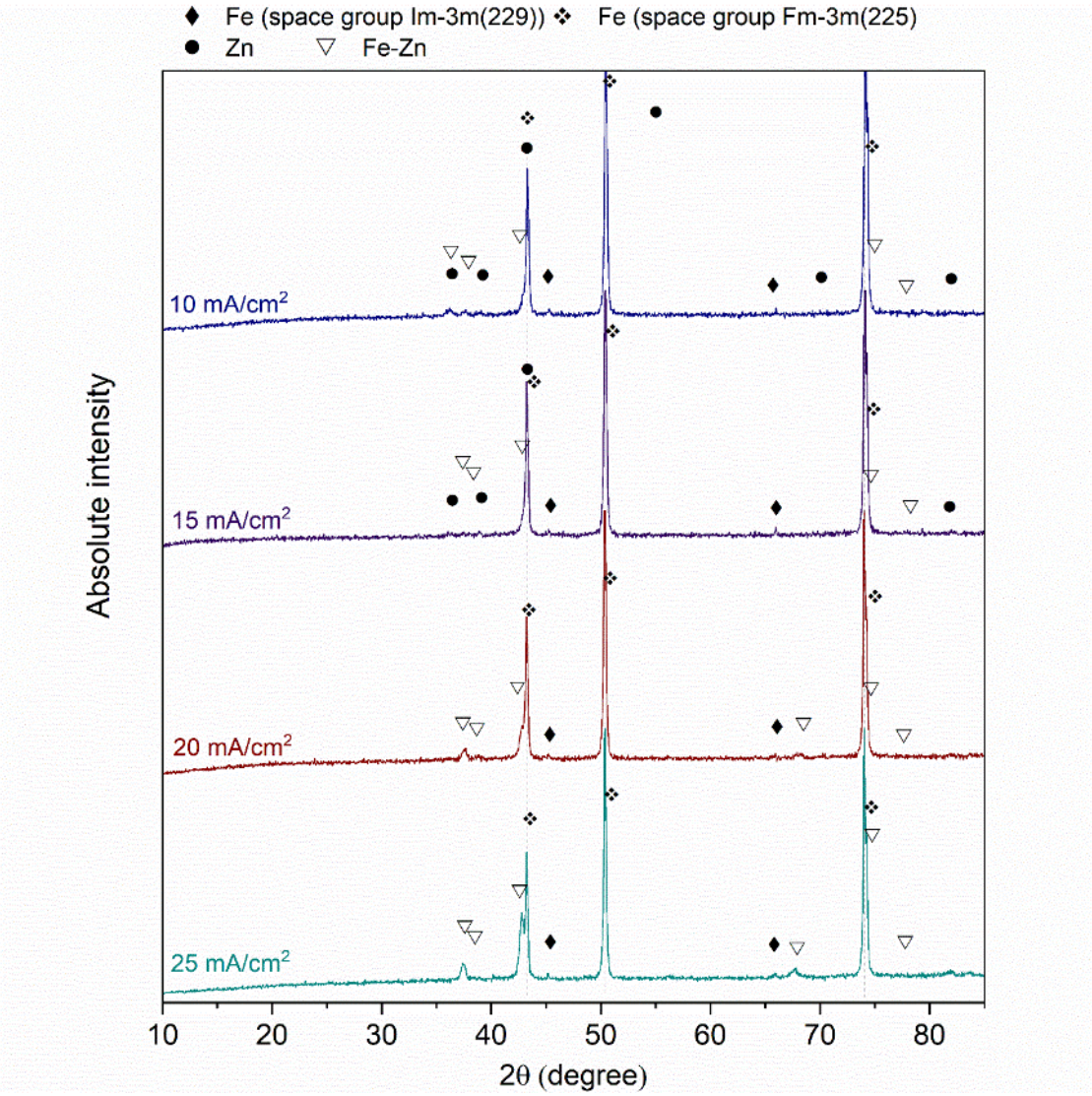

Fig. 16. Diffractograms of the samples with Zn-Fe-Mo alloy coatings deposited at different current density values with $(NH_4)_2SO_4$.

For the case of $(NH_4)_2SO_4$ based coatings, XRD patterns for samples prepared at 10 and 15 mA cm^{-2} also showed high-intensity peaks for zinc, accompanied by lesser intensity peaks for iron at 2θ values of 45.2° and 65.7°, respectively, corresponding to hexagonal Zn (space group $P6_3/mmc$) and cubic Fe (space group Im-3m).). There is also potential for the existence of cubic Fm-3m (225) symmetry iron, though this is hard to establish due to peak overlap with the copper substrate, particularly near the 2θ positions shared by the two phases. However, the PDF-5+ database card 01-071-4649 supports a tentative identification of this phase.

When the current density increased to 20 and 25 mA cm^{-2}, noticeable changes were evident in the coatings obtained from the ammonium-containing bath. The intermetallic Fe-Zn phases became more intense, as evidenced by the increasing intensity of their respective diffraction peaks. Meanwhile, the pure zinc peaks dissolved or disappeared, suggesting that zinc is increasingly involved in the development of Fe-Zn intermetallic compounds rather than as an independent phase. Such behavior is also in line with the evolution of the alloy's microstructure to a more chemically complex multiphase system, as also confirmed in the literature [120].

Specifically, zinc can still be detected in all coatings for any current density and bath composition combination, a clear sign of its dominant role within the alloy matrix. Therefore, the molybdenum content, as measured by EDXS, was fairly low overall, never more than 5 wt.% in $(NH_4)_2SO_4$ bath derived coatings and presently less than 1 wt.% in Na_2SO_4 bath-deposited coatings. Further, in all cases, the molybdenum content decreased with a rise in current density, in line with previously reported challenges in co-depositing Mo at higher cathodic polarization regimes. Due to the low concentration, no separate diffraction peaks for molybdenum or Fe-Mo intermetallic phases were observed in any of the XRD patterns obtained, as per the determined XRD detection limits for secondary phases in nanostructured systems.

Together, these findings confirm that both electrolyte composition and deposition current density play important roles in the phase evolution, crystallinity, and alloy complexity of Zn-Fe-Mo coatings. The noticed transition from pure metals to intermetallic compounds, along with peak broadening at elevated current densities, indicates the tendency toward multiphase and nanocrystalline coatings, which are typically more desirable in applications requiring enhanced mechanical and corrosion-resistant properties.

4.7.2 Zn-Fe-W

XRD analyses were performed to determine the phase composition of the alloy coatings obtained at different current densities. The analysis results and the phases assigned to the peaks are summarized in Figures 17 (for the bath with Na_2SO_4) and 18 for the bath with $(NH_4)_2SO_4$. All samples show peaks characteristic of copper, which is the substrate for the obtained alloy coatings. These peaks are located at the 43.2, 50.4, 74.1 2-theta, which coincide well with the peaks for copper reference PDF Cart No. 00-004-0836. Peaks corresponding to zinc, iron and intermetallic phases are also observed, depending on the deposition conditions, such as current density and bath composition.

Coatings obtained at a current density of 10 mA cm^{-2} consist primarily of metallic zinc (reference PDF Cart No. 01-078-9363). The diffraction pattern shows small iron peaks (reference PDF Cart No. 01-081-8769) that disappear when deposition is performed at 15 mA cm^{-2}. This increase in current density causes a significant change in the phase composition of the Zn-Fe-W alloy coating. When peaks characteristic for metallic Zn and Fe disappear, a new intermetallic phase similar to the $Fe_{22}Zn_{78}$ type phase appears, which is well described by the file from the database PDF Cart No. 01-081-876901-071-8477. Further increasing the current density during deposition no longer significantly changes the phase composition of the formed alloy coatings.

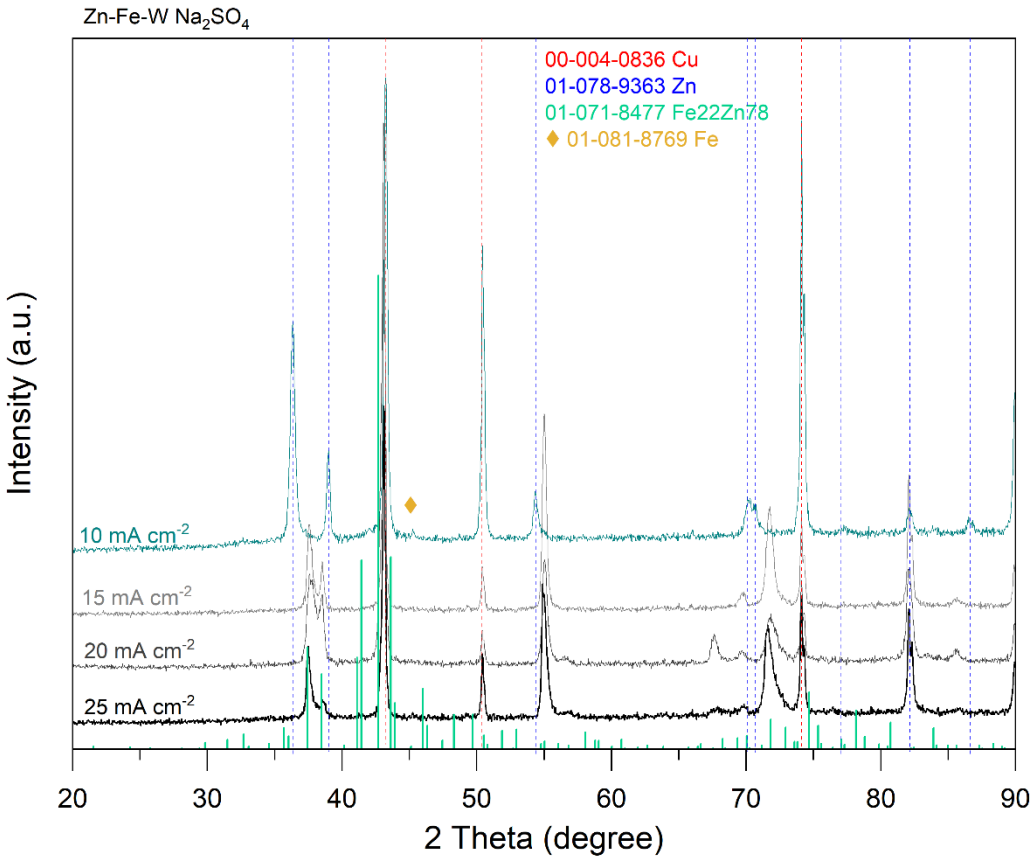

Fig. 17. Diffractograms of the samples with Zn-Fe-W alloy coatings deposited at different current density values with Na_2SO_4.

Fig.18. shows diffractograms for samples obtained from a bath containing $(NH_4)_2SO_4$. The diffraction patterns of the samples obtained at the current density of 10 and 15 mA cm^{-2} show the peaks for zinc (PDF Cart No. 01-078-9363) and the most intense peak for iron at the angle 2θ 45.2° (PDF Cart No. 01-081-8769). When the current density increased to 20 and 25 mA cm^{-2}, the peaks characteristic of zinc and iron disappeared, but the type of intermetallic $Fe_{22}Zn_{78}$ phase appeared. The formation of Fe-Zn intermetallic phases at higher deposition densities of alloy coatings was also observed in an earlier work in which Zn-Fe-Mo type coatings were investigated. However, the diffraction patterns do not show peaks for metallic tungsten or intermetallic W phases due to the sensitivity of the XRD method (components in the amount of 3-5 wt.% provide an insufficiently strong signal). EDXS analysis confirms that the Zn-Fe-W alloy coatings contain up to 1.5% and 5.5% wt.% of W for coatings from Na_2SO_4 and $(NH_4)_2SO_4$ base galvanic baths, respectively.

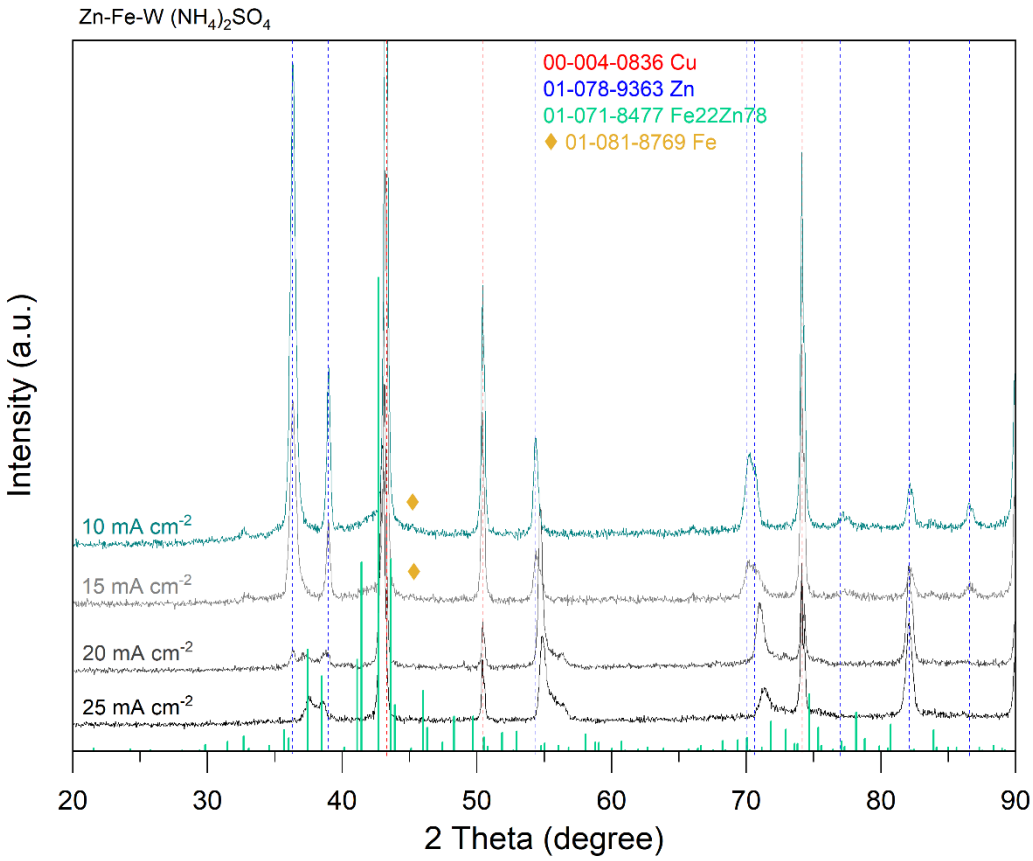

Fig. 18. Diffractograms of the samples with Zn-Fe-W alloy coatings deposited at different current density values with $(NH_4)_2SO_4$.

4.8 The influence of plating bath composition and current density on coating's corrosion resistance

4.8.1 Zn-Fe-Mo

Figure 19 illustrates the evolution of the corrosion potential (E) over 24 hours, determined from a series of linear polarization measurements. These electrochemical measurements as a function of time provided a perception of the corrosion behavior and stability of the surface of Zn-Fe-Mo alloy coatings electrodeposited under different conditions. In Figure 19a, it is possible to notice one specific pattern in terms of coatings made from a Na_2SO_4 base galvanic bath; the specimens coated at high current densities, namely at 20 and 25 mA cm^{-2}, initially have more positive corrosion potentials of about −910 and −890 mV vs. Ag|AgCl, respectively. Such a finding indicates an improvement in initial corrosion resistance by virtue of the

increased current densities. Of particular notice is that the specimen coated at 20 mA cm^{-2} maintains a relatively steady E over the entire period of the 24-hour test with minimal deviation from its initial value. Such steadiness provides evidence for probable attainment of a more protective and uniform surface coat, possibly resulting from either suitable microstructural properties or suitable alloy composition balance at this specific current density.

On the other hand, Figure 19b shows results for coatings from a solution with ammonium ions. Here, specimens coated at current densities of 20 and 25 mA cm^{-2} exhibit even more noble corrosion potentials initially, achieving −825 and −850 mV with reference to Ag|AgCl, respectively, suggesting good initial resistance to corrosion. However, after some time, a significant change in behavior is observed. For the time period between 4 and 16 hours, a significant drop in the corrosion potential is observed, which would most likely reflect the breakdown or loss of the initially protective films. After about 18 hours, the E values begin to stabilize, indicating the formation of a new passive film that, although stable, provides less coverage. Towards the end of the 24-hour period, a steady drop in corrosion potential continues to trend, implying sustained though slower corrosion reactions.

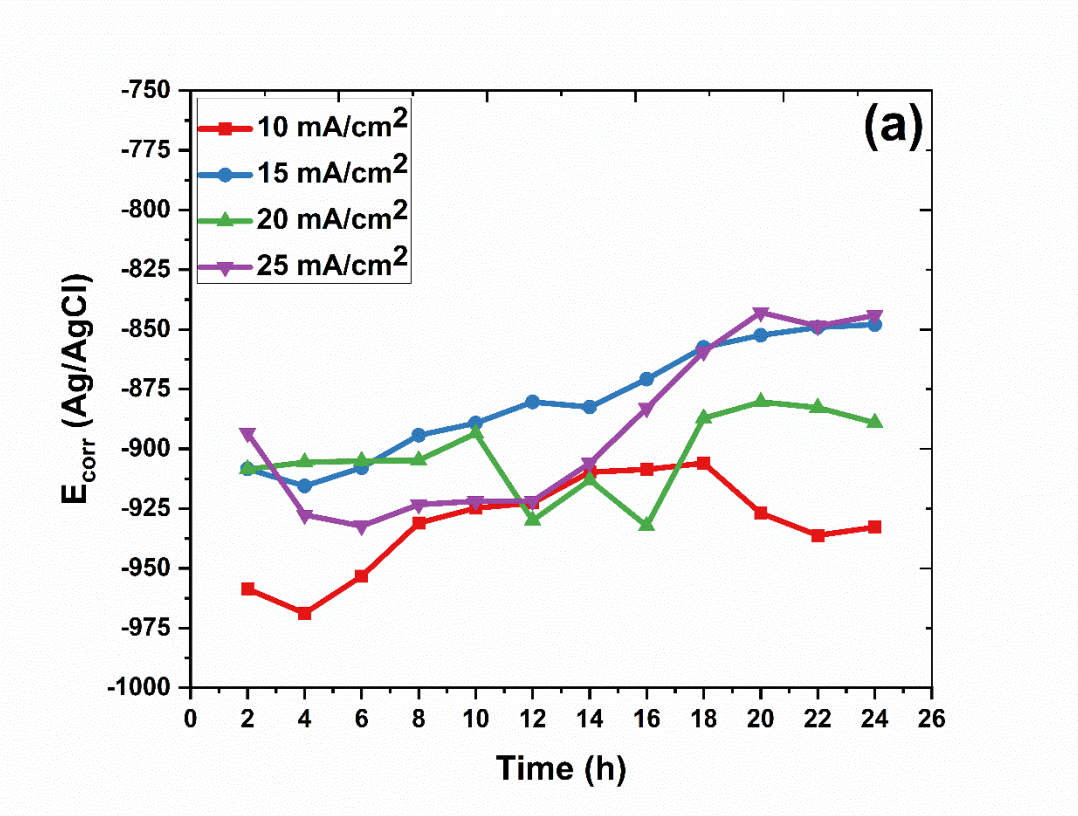

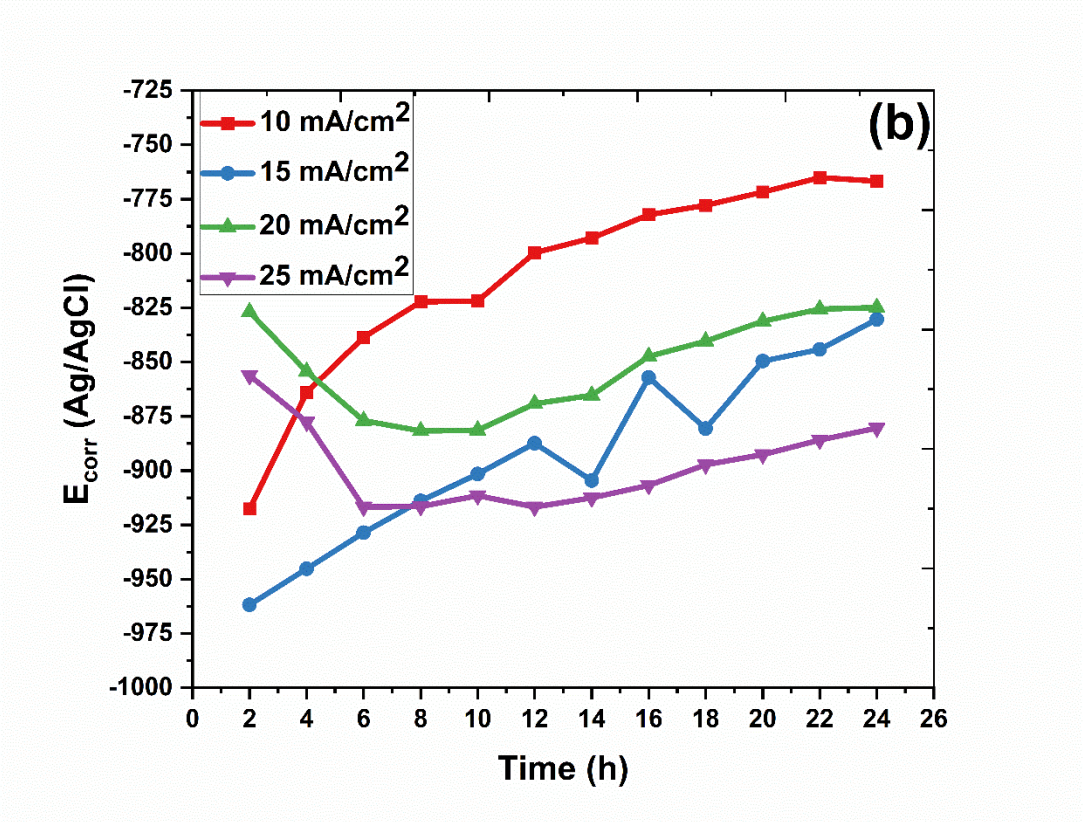

Fig. 19. Evolution of E_{corr} determined from LPR measurements in 0.5M NaCl solution for 24 hours exposure of steel samples electrodeposited with Zn-Fe-Mo alloy coatings of (a) Na_2SO_4 and (b) $(NH_4)_2SO_4$ base galvanic baths at different current densities.

Not surprisingly, coatings with lower current densities using the ammonium-containing bath demonstrate the reverse effect. Their *E* values increase over time, probably through some form of surface passivation, likely due to the development of an oxide surface. This is not unusual for coatings with greater amounts of molybdenum, whose metal is recognized to generate passivity and inhibit corrosion. Indeed, previous EDXS analysis indicates that the Mo levels are greater in coatings with lower current densities, consistent with greater corrosion resistance over time. The shifts in corrosion potential for these specimens may be attributed to the shifting surface chemistry such that the development of metal oxynitrides or mixed oxides enhances the coating's barrier properties and corrosion-operational capabilities.

Fig. 20 illustrates the time-dependent evolution of polarization resistance (R_p) of Zn-Fe-Mo alloy coatings electrodeposited at different cathodic current densities. These are an important indicator of corrosion resistance, with increasing R_p generally indicating improved resistance to corrosive environments. For the coatings formed without ammonium ions in the plating bath and deposited at the lower current densities (10 and 15 mA cm^{-2}) in Fig. 20a, there is a

relatively stable R_p trend for the 24-hour test period. The stability shows that the coatings form a uniform passive layer even at the lower current density, which is not broken over the immersion period.

However, a noticeable difference in the values of R_p is observed for the sample plated at 20 mA cm^{-2} from the same ammonium-free electrolyte. These discrepancies can be attributed to the increased content of iron (wt.%) in the coating since iron tends to influence the electrochemical activity of the surface and may introduce microstructural inhomogeneities, which consequently reflect on the electrochemical stability. Despite these differences, after the 24-hour test, the coatings obtained at the larger current densities (20 and 25 mA cm^{-2}) display significantly larger R_p values, showing enhanced corrosion resistance compared to those formed at lower current densities.

In contrast, Figure 20b shows the results of the coatings achieved from a plating bath containing $(NH_4)_2SO_4$ (ammonium ions). Here, the coatings plated at lower current densities (10 and 15 mA cm^{-2}) have lower R_p values, indicating comparatively lower corrosion resistance, possibly due to less compact microstructure or lower iron incorporation. Interestingly, the sample deposited at 20 mA cm^{-2} exhibits a high polarization resistance of approximately 27 kΩ cm^2 in the beginning, suggesting good initial corrosion protection. Over time, however, the R value drops steadily, eventually to around 10 kΩ cm^2 by the 24-hour mark. The decline signifies degradation of the protective surface layer through surface reactions, such as oxide breakdown or dissolution of the less stable phases.

In addition, the deposit with 25 mA cm^{-2} deposited from the ammonium-containing bath again shows a relatively higher R_p, which can be attributed to a higher iron content in the coating. As established in the literature [120] the corrosion resistance of iron-alloy coatings is significantly influenced by the iron weight percentage (wt.%). An optimal Fe content can optimize passivity and structure integrity, while excessive content may enhance galvanic effects or phase imbalance, so it is one of the most important factors to influence electrochemical performance.

In conclusion, these findings point to the paramount effect of both bath composition and current density on the electrochemical response of Zn-Fe-Mo coatings. These results show that, while higher current densities can be used to improve corrosion resistance through beneficial microstructure development and alloy composition, such advantages also depend

significantly on the plating bath's chemical nature, i.e., the presence or absence of complexing agents such as ammonium ions.

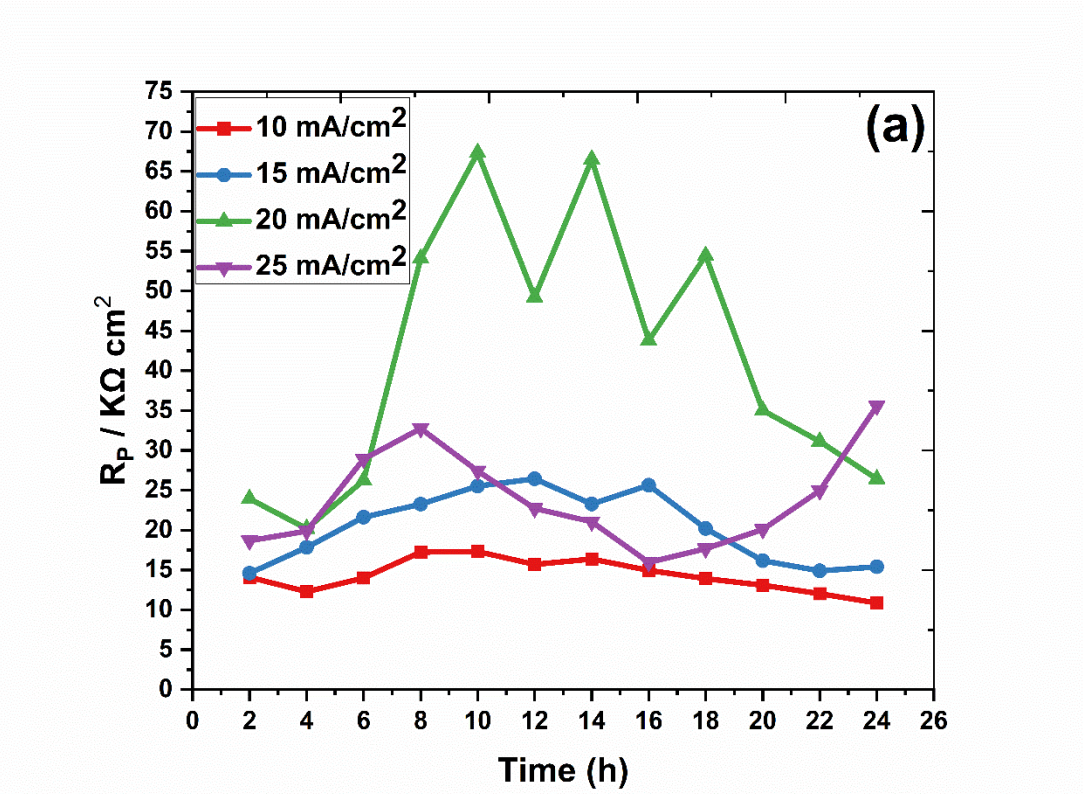

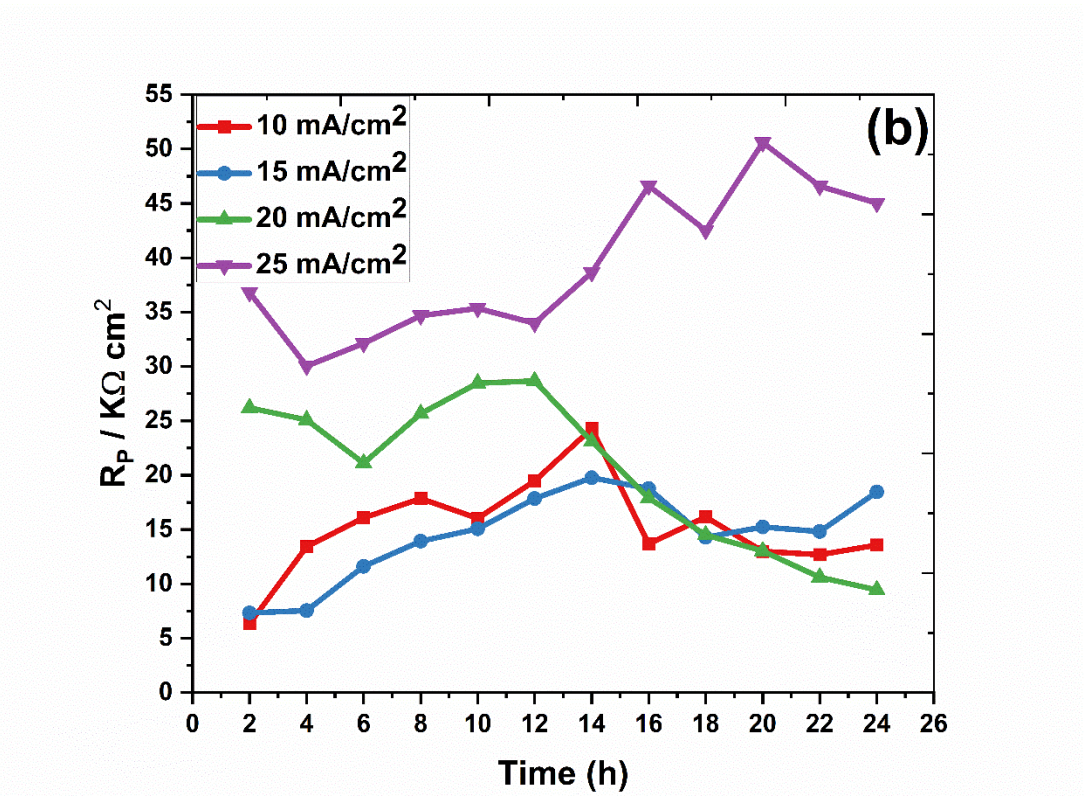

Fig. 20. Evolution of the polarisation resistance R_p of LPR in a 0.5M NaCl solution during 24 hours exposure of the steel samples electroplated with Zn-Fe-Mo alloy coatings from (a) Na_2SO_4 and (b) $(NH_4)_2SO_4$ base galvanic baths at different current densities.

Polarization curves were recorded after 24 hours of exposure in a sodium chloride (NaCl) solution, as shown in Figure 21. The data reveal that regardless of whether ammonium ions were present in the electrodeposition bath, increasing the current density during electrodeposition (up to 25 mA cm^{-2}) resulted in a lower current density in both the anodic and cathodic regions of the polarization curves. This indicates an overall improvement in the corrosion resistance of the coatings at higher deposition currents. Moreover, significant shifts in the transition potentials between the cathodic and anodic regions were observed. These shifts can be attributed to several interrelated factors, including changes in the alloy composition caused by variations in deposition conditions, differences in surface homogeneity due to morphological changes at higher current densities, and alterations in surface chemistry, such as the formation of different passive films or oxides. Together, these factors influence the electrochemical behavior of the coatings and highlight the impact of deposition parameters on their corrosion performance.

The analysis of the slopes of the polarization curves provided a quantitative understanding of the corrosion behavior of the examined Zn-Fe alloy coatings, as summarized in Table 5. The corrosion current densities (i_{corr}) determined for all samples were relatively low, generally falling within the range of 0.3 to 1 μA cm^{-2}, indicating good corrosion resistance. For the first group of coatings, a clear trend was observed: increasing the electrodeposition current density led to a decrease in i_{corr} values, suggesting improved corrosion resistance. Simultaneously, the slopes of both the cathodic (β_c) and anodic (β_a) branches of the polarization curves became steeper, indicating a more pronounced electrochemical behavior. These changes were also associated with a positive shift in the corrosion potential (E_{corr}), pointing to a more noble corrosion behavior as the current density increased.

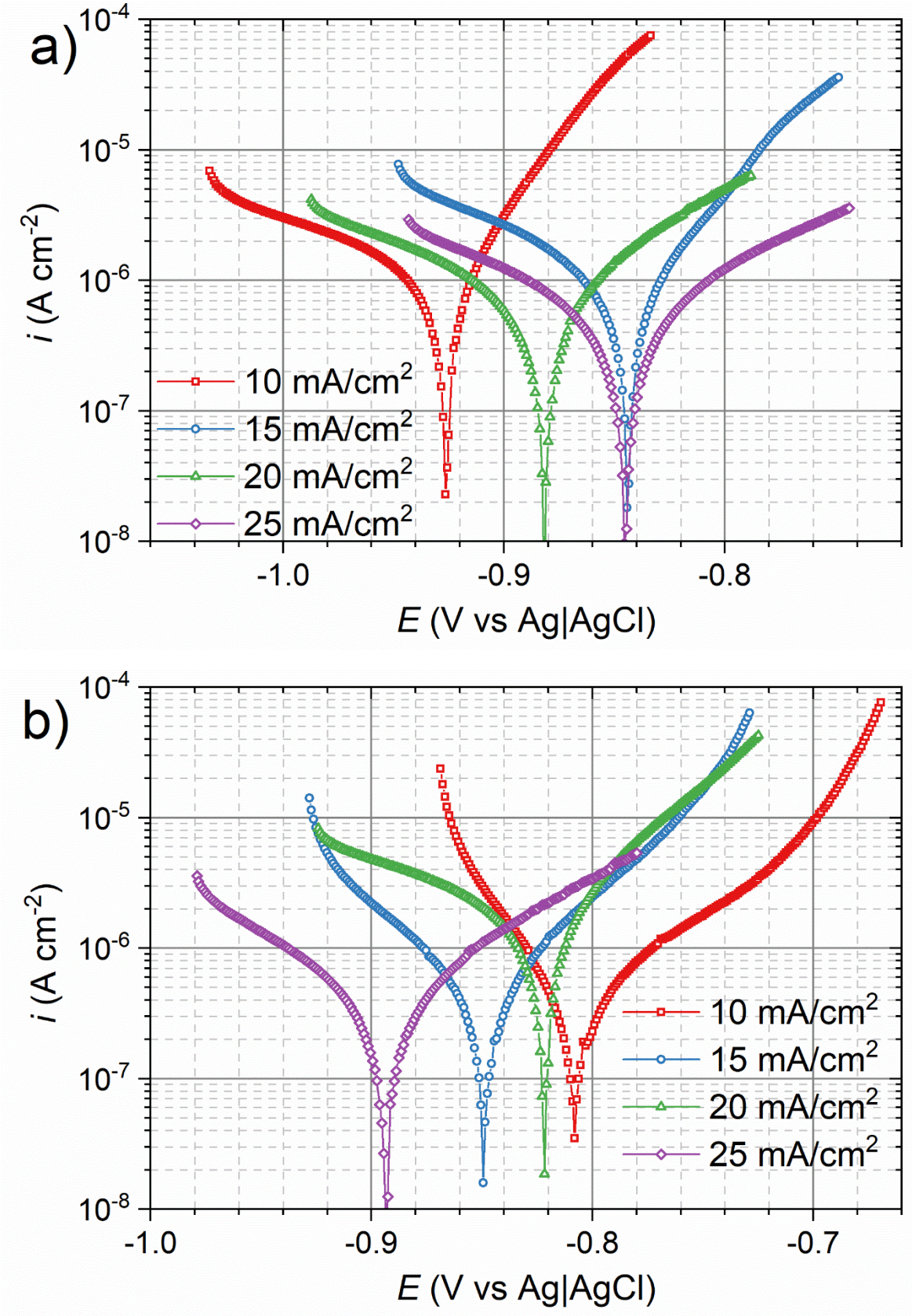

Fig. 21. Polarization curves of Zn-Fe-Mo alloy coatings deposited at different current densities from plating baths containing (a) Na_2SO_4 and (b) $(NH_4)_2SO_4$ salt, recorded after 24 hours of exposure of the samples in 0.5 M solution of NaCl.

This electrochemical improvement was correlated with noticeable morphological changes in the coatings. Specifically, coatings deposited at lower current densities of 10 and 15 mA cm^{-2} exhibited uneven and non-homogeneous surfaces. In contrast, those produced at higher current densities of 20 and 25 mA cm^{-2} displayed smoother and more uniform surface morphologies. These morphological differences likely contribute to the observed variations in corrosion resistance. Furthermore, the iron content (Fe wt.%) and the distinct phase structures present within the Zn-Fe alloy are additional factors that can significantly affect the corrosion performance of the coatings, as supported by previous studies[121].

For the second group of coatings, the corrosion current densities (i_{corr}) were generally lower compared to the first group, indicating improved corrosion resistance overall. However, a notable exception was observed in the coating deposited at a current density of 20 mA cm^{-2} in the presence of ammonium ions. This particular sample exhibited the highest i_{corr} value among all coatings in this group, as shown in Table 5. This deviation is not coincidental and can be explained by the results of linear polarization resistance (LPR) measurements. Although the coating initially showed high polarization resistance (R_p), indicating good corrosion resistance, its performance deteriorated significantly over time. After 12 hours of exposure, the R_p values began to decline, and by the 24-hour mark, this coating demonstrated the lowest corrosion resistance of all samples.

This pronounced degradation in performance suggests that the coating's initial protection was not stable over extended exposure. One possible explanation for this behavior could be the relatively high iron content (Fe wt.%) in the alloy, which may have contributed to accelerated corrosion processes. A higher Fe content can alter the microstructure and phase distribution within the coating, potentially leading to less stable corrosion-resistant phases or galvanic interactions that promote localized corrosion. Therefore, the combination of deposition conditions and compositional factors appears to play a crucial role in the long-term corrosion behavior of these coatings.

Table 5. Corrosion parameters estimated from potentiodynamic polarization curves recorded for Zn-Fe-Mo alloy coatings deposited at different current densities from plating baths containing Na_2SO_4 or $(NH_4)_2SO_4$

Parameter	Na_2SO_4 plating bath current density (mA cm^{-2})	$(NH_4)_2SO_4$ plating bath current density (mA cm^{-2})

	10	15	20	25	10	15	20	25
β_a (mV dec^{-1})	40	50	85	80	62	60	51	80
β_c (mV dec^{-1})	103	83	135	120	42	69	100	85
i_{corr} (μA cm^{-2})	0.93	0.63	0.60	0.56	0.27	0.37	1.0	0.30
E_{corr} (mV vs Ag|AgCl)	−926	−844	−882	−846	−808	−849	−822	−894

Electrochemical Impedance Spectroscopy (EIS) was utilized to investigate the corrosion response of electrodeposited coatings in a corrosive environment with high chloride content, with particular focus on the influence of different sulphate salts utilized in the plating baths. Nyquist and Bode plots were constructed to comprehensively illustrate changes in corrosion resistance under altered conditions. Specifically, for the sodium sulphate (Na_2SO_4) plating bath, the raise of cathodic current density from 10 to 25 mA cm^{-2} caused a drastic increase of the real part of the impedance, as shown in Figure 23a. Although the overall shape of the impedance spectra was similar, characteristic flattening of the semicircles at mid-frequency regions was observed, reflecting changes in the electrochemical characteristics of the coating. At still greater current densities, the impedance amplitude increased significantly high, from 70–80 kΩ cm² (Figure 23b), indicating improved barrier characteristics of the deposits. Even the phase angle (θ) in the Bode plot (Figure 23c) exhibited two distinct separated maxima, indicating the presence of two electrochemical processes. This answer required the use of a two-time constant electrical equivalent circuit (EEC) model in order to adequately fit the experimentally gained data, as illustrated in Figure 22a.

The electrical elements of the equivalent circuit model shown in Figure 22a can be described as follows. The element R_1 is the bulk electrolytic solution resistance, a measure of ionic medium conductivity. CPE1 (Constant Phase Element) and R_2 account for the capacitive and resistive behavior of the surface layer, including those resulting from oxide or hydroxide films and exterior metallic surface porosity. CPE2 and R_3 describe the capacitive and resistive responses associated with the corrosion process occurring at the electrolyte/metal interface. Such an equivalent circuit is utilized to model the electrochemical behavior of metal coatings, particularly for zinc and zinc alloy systems, since it can handle both the corrosion mechanism and the surface film characteristics.

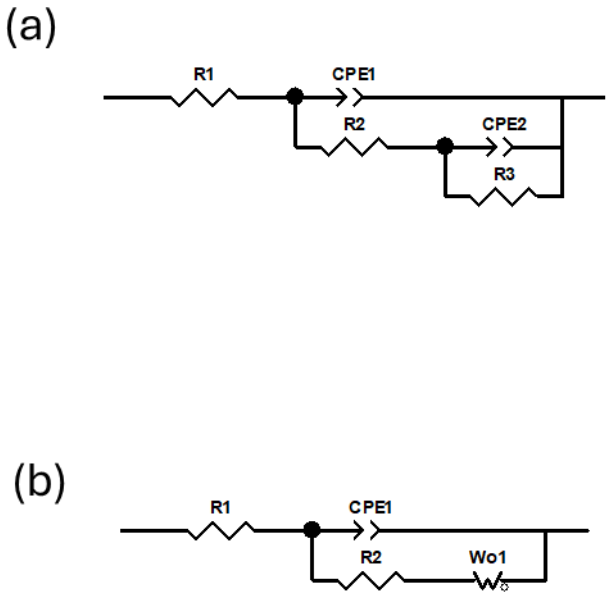

Fig. 22. Electric equivalent circuits used to fitting the impedance spectra recorded for the Zn-Fe-Mo alloy coatings after 24 hours of exposure of the samples in 0.5 M solution of NaCl.

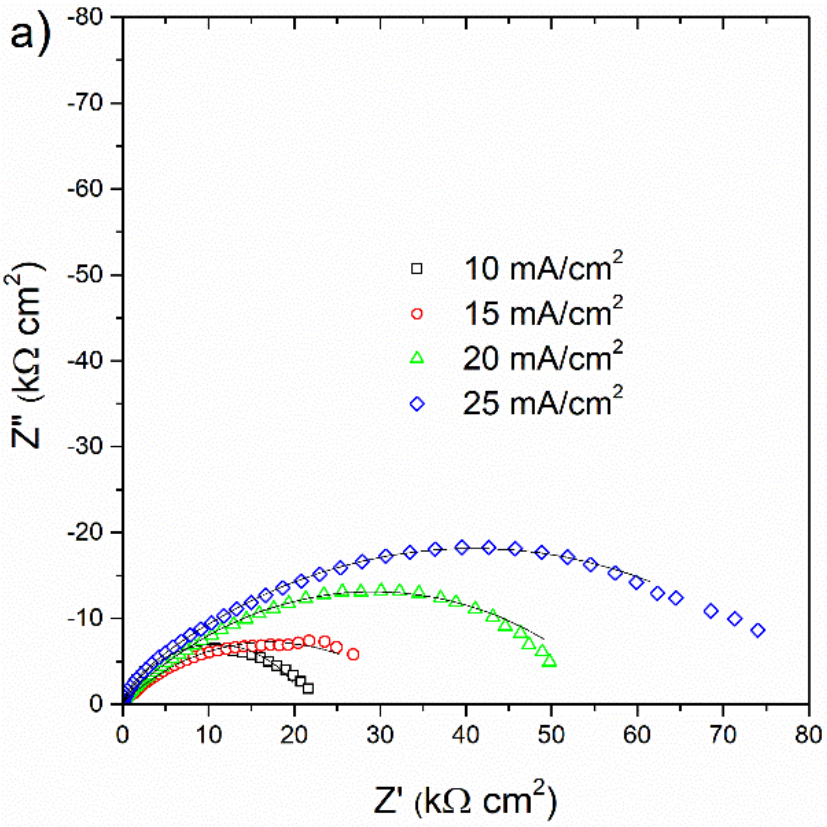

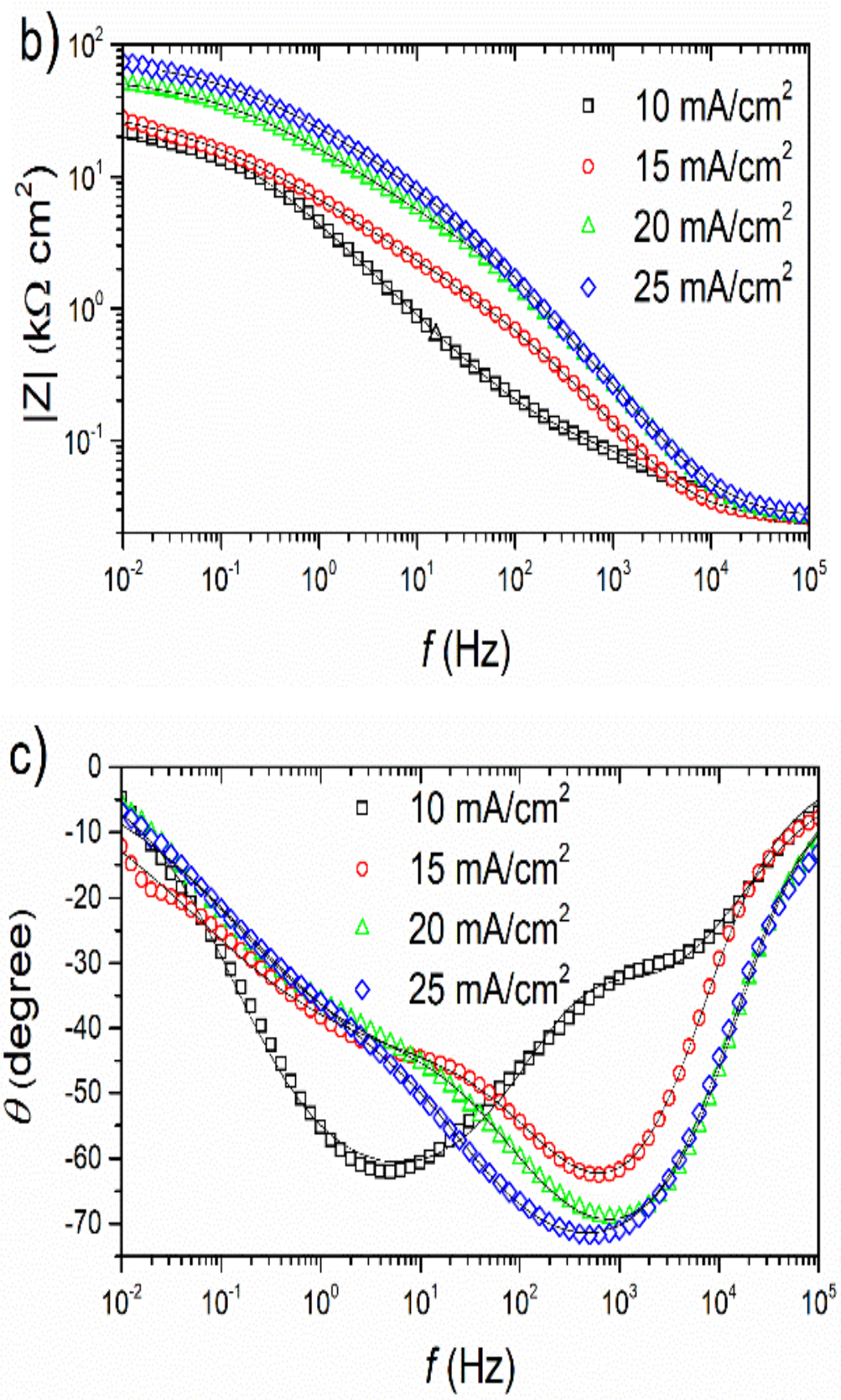

Fig. 23. Nyquist (a) and Bode (b, c) plots of the impedance spectra of Zn-Fe-Mo alloy coatings deposited from the plating bath containing Na_2SO_4 salt, recorded after 24 hours of exposure of the samples in 0.5 M solution of NaCl. Solid lines are the fitting lines.

Table 6. Fitting results for the impedance spectra of Zn-Fe-Mo alloy coatings deposited from a plating bath containing Na_2SO_4 salt, recorded after 24 hours of exposure of the samples in 0.5 M solution of NaCl.

Electrodeposition current density (mA cm^{-2})	R_1 (Ω cm^2)	CPE_1-T (Ω^{-1} cm^{-2} s^P)	CPE_1-P	R_2 (kΩ cm^2)	CPE_2-T (Ω^{-1} cm^{-2} s^P)	CPE_2-P	R_3 (kΩ cm^2)
10	24 (1.5) *	2.15×10^{-5} (21)	0.70 (2.8)	0.12 (11)	3.19×10^{-5} (14)	0.76 (2.0)	21.2 (0.9)
15	26 (0.6)	3.70×10^{-6} (4.7)	0.87 (0.55)	0.83 (6.7)	5.04×10^{-5} (0.9)	0.50 (0.8)	33.5 (1.5)
20	25 (0.5)	1.89×10^{-6} (2.2)	0.87 (0.3)	3.09 (3.9)	1.94×10^{-5} (0.8)	0.53 (0.8)	55.6 (1.1)
25	26 (0.5)	2.06×10^{-6} (1.8)	0.86 (0.2)	7.08 (5.1)	1.43×10^{-5} (1.2)	0.51 (1.5)	75.7 (2.0)

* values in brackets are the % error

The result of the fitting method, along with the corresponding error values (in brackets), is provided in Table 6. The goodness of the fits, in the form of the chi-squared (χ^2) values, was in the range from 1.5×10^{-5} to 5×10^{-4}, thereby indicating a good agreement between the experimental data and the proposed equivalent circuit model. The fitted curves are superimposed in Figures 23 on the impedance spectra as well. For electrodeposited coatings in the presence of Na_2SO_4, increasing the electrodeposition current density significantly increased the surface layer resistance, from 0.1 to 7 kΩ cm². Meanwhile, the CPE1-T parameter decreased and CPE1-P rose, indicating that the surface layer became more homogeneous and had a more ideal capacitive behavior, as observed in Table 6. Moreover, the charge transfer resistance (R_3) was notably elevated, from 21 to 75 kΩ cm², in response to the increasing current density. The observation was accompanied by a reduction in CPE2-T, which indicates less non-ideal capacitive behavior. Nevertheless, the CPE2-P value continued to be in the vicinity of 0.5, i.e., the electric double layer does not behave purely capacitively. Rather, a P value close to 0.5 tends to point to the prominent role of diffusion-controlled processes in the corrosion mechanism of these coatings.

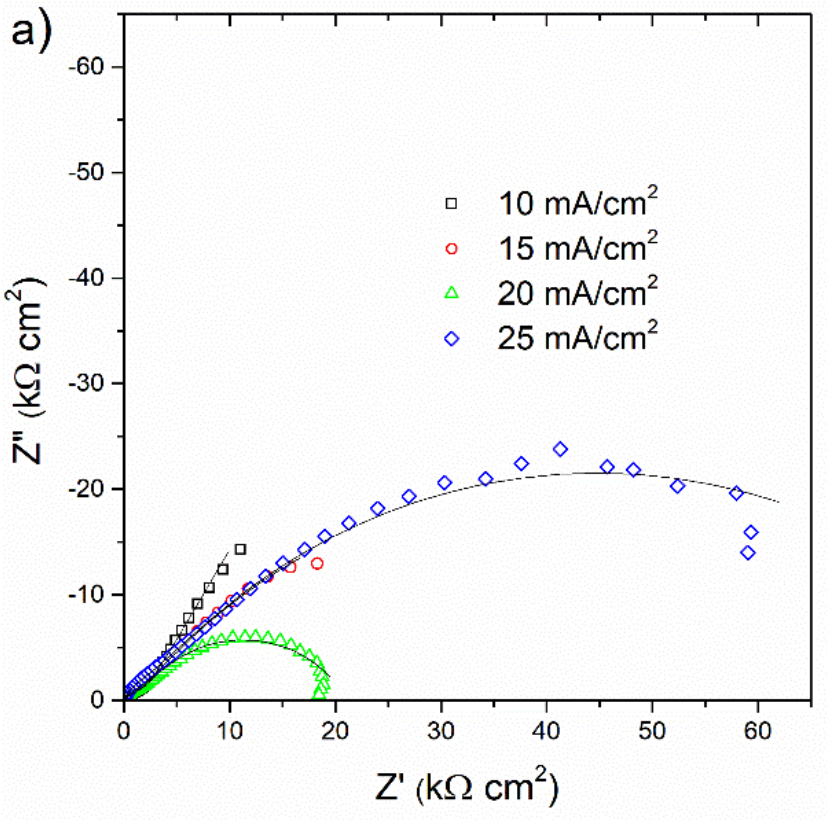
a)
-60
-50
-40
-30
-20
-10
0
Z'' (kΩ cm2)
10 mA/cm2
15 mA/cm2
20 mA/cm2
25 mA/cm2
0
10
20
30
40
50
60
Z' (kΩ cm2)

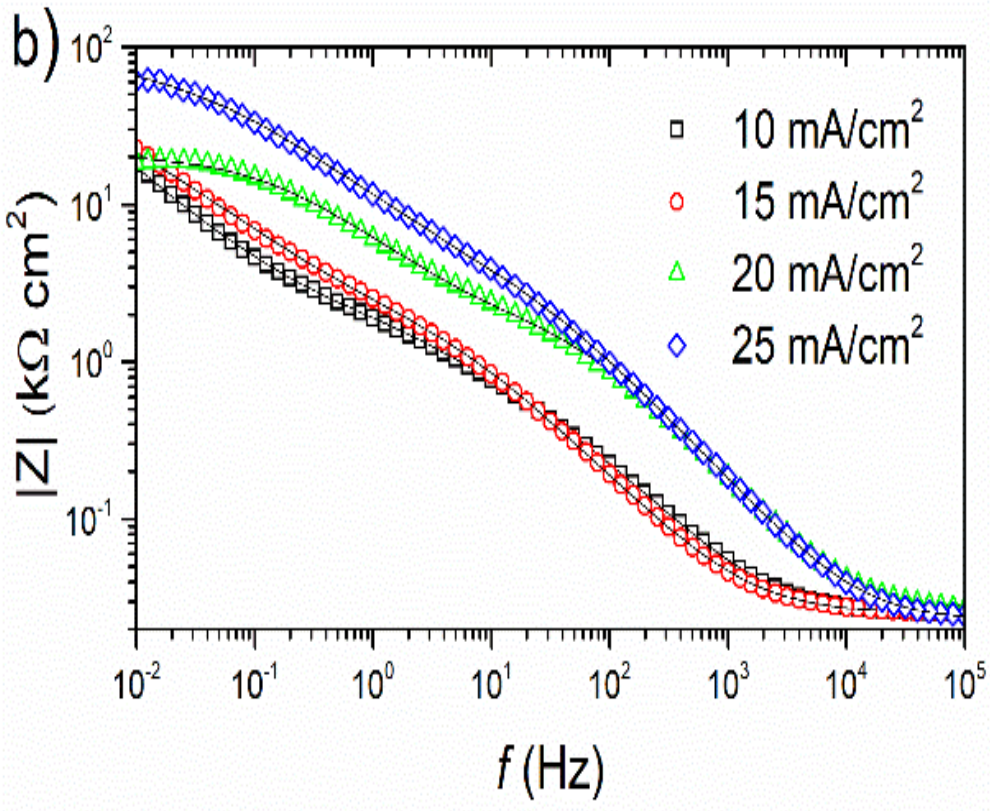
b)
10^2
10^1
10^0
10^-1
|Z| (kΩ cm2)
10 mA/cm2
15 mA/cm2
20 mA/cm2
25 mA/cm2
10^-2
10^-1
10^0
10^1
10^2
10^3
10^4
10^5
f (Hz)

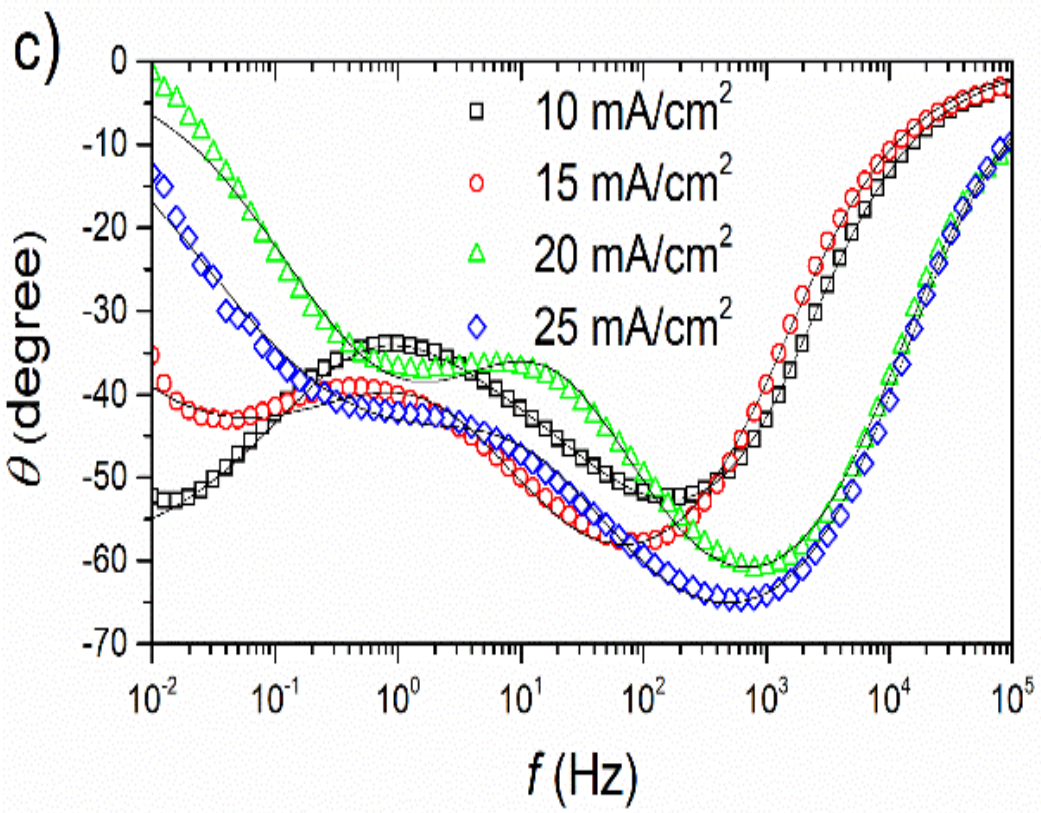

Fig. 24. Nyquist (a) and Bode (b, c) plots of the impedance spectra of Zn-Fe-Mo alloy coatings deposited from the plating bath containing $(NH_4)_2SO_4$ salt, recorded after 24 hours of exposure of the samples in 0.5 M solution of NaCl. Solid lines are the fittings lines.

Table 7. Fitting results for the impedance spectra of Zn-Fe-Mo alloy coatings deposited from a plating bath containing $(NH_4)_2SO_4$ salt, recorded after 24 hours of exposure of the samples in 0.5 M solution of NaCl.

Electrodeposition current density (mA cm^{-2})	R_1 (Ω cm^2)	CPE_1-T (Ω^{-1} cm^{-2} s^P)	CPE_1-P	R_2 (kΩ cm^2)	CPE_2-T (Ω^{-1} cm^{-2} s^P)	CPE_2-P	R_3 (kΩ cm^2)
10	25 (0.3) *	2.17×10^{-5} (4.5)	0.80 (0.6)	0.25 (11)	W_o1 **	W_o1 **	W_o1 **
15	25 (0.5)	3.94×10^{-5} (2.2)	0.76 (0.4)	2.11 (3.7)	1.80×10^{-4} (1.0)	0.57 (1.6)	81.5 (9.8)
20	25 (0.9)	5.20×10^{-6} (3.2)	0.80 (0.4)	2.07 (2.7)	4.66×10^{-5} (1.5)	0.66 (1.2)	19.1 (1.4)
25	22 (0.7)	4.73×10^{-6} (2.5)	0.81 (0.3)	3.76 (4.0)	2.76×10^{-5} (0.9)	0.56 (1.0)	85.0 (2.0)

* % error in brackets

** for "10 mA cm^{-2}" sample the values of W_o1 were: W_o1-R = 4979 (2.1) (Ω cm^2); W_o1-T = 2.5 (3.8) s; W_o1-P = 0.33 (0.5)

W0= 2.6410e-04

Electrodeposited Zn-Fe-Mo coatings in solutions containing $(NH_4)_2SO_4$ produced similar spectra, but with higher impedances. According to the Nyquist and Bode representations (Figs. 24a, 24b, and 24c), two-time constants exist, thus supporting the model in Fig. 23a should be sufficient.

The model displayed in Figure 23a was utilized for this research, with the same physical meaning as its respective components defined. The outcome of the fitting process is presented in Table 7, where the errors of each parameter are, in turn, inserted in parentheses. The obtained chi-squared (χ^2) values varied between 1.0×10^{-5} and 4.6×10^{-4}, revealing a good fit between the experimental data and the fitted curves. These fitted curves are shown as solid lines in Figure 24. In the case of the coating deposited at 10 mA cm^{-2} current density, however, the resistance parameter R_3 had a very large error (10^7 Ω cm^2). This, along with the shape of the impedance spectrum, indicated that the diffusion effects could be extremely pronounced in the corrosion process of this sample. Therefore, for this coating, a modified model (Fig. 23b) was used. In the modified model, the second time constant is substituted by a finite-length Warburg element (W_o) which is responsible for the diffusion of species through the coating thickness. The coating deposited at 10 mA cm^{-2} shows a well-developed powder-like surface morphology. This type of microstructure can generate inhomogeneity and porosity internally, which will impede the mobility of ionic species. Thus, impedance response diffusion limitations are most probably caused by the intricate internal structure of this heterogeneous layer.

4.8.2 Zn-Fe-W

The value of the corrosion potential (E_{corr}) calculated using 24 hour linear polarization measurements is shown in Figure 25. In these studies, E_{corr} values were continuously recorded to assess the electrochemical corrosion resistance of Zn-Fe-W coatings. From Figure 25a, it is evident that both 20 mA cm^{-2} and 25 mA cm^{-2} samples deposited using the Na_2SO_4 base galvanic bath possessed relatively higher initial corrosion potentials at -1020 mV and -990 mV vs. Ag|AgCl electrode, respectively. The observed steady-state behavior is presumably due to their tightly packed microstructure, which inhibits active dissolution.

For coating samples deposited at relatively low current densities of 10 and 15 mA cm^{-2}, there are slightly more negative initial corrosion potentials close to -1050 mV Ag|AgCl. However, with time, these potentials migrated to relatively more positive values. This can be attributed to secondary processes taking place at the electrode/electrolyte interface, especially on rough surfaces. Roughness on such surfaces can facilitate localized activity related to corrosion, thus affecting polarization. Similar trends have been shown to exist previously between surface roughness, localized electrolytic processes, and polarization [122].

On the other hand, the specimens produced using the ammonium-containing bath (Fig. 25b) revealed similar passive behavior at higher current densities of 20 mA cm^{-2} and 25 mA cm^{-2}, with both initial and final values of the corrosion potential settling around -1000 mV vs. Ag|AgCl. This indicates that those samples produced at higher current densities have enough strength to provide long-term protection during immersion. At lower current densities, there was a corresponding raise in corrosion potential values similar to those observed on samples produced using ammonium-free baths. This can be attributed to interface-driven reactions owing to higher surface roughness values corresponding to samples deposited at low current densities.

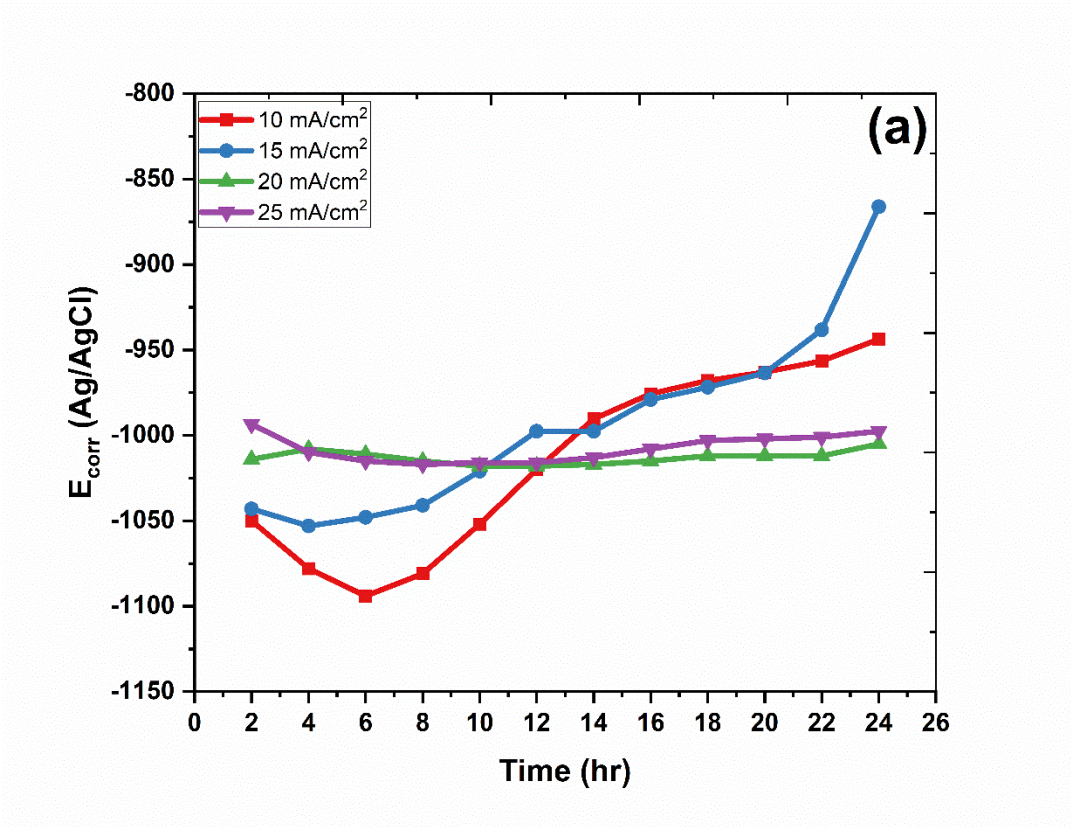

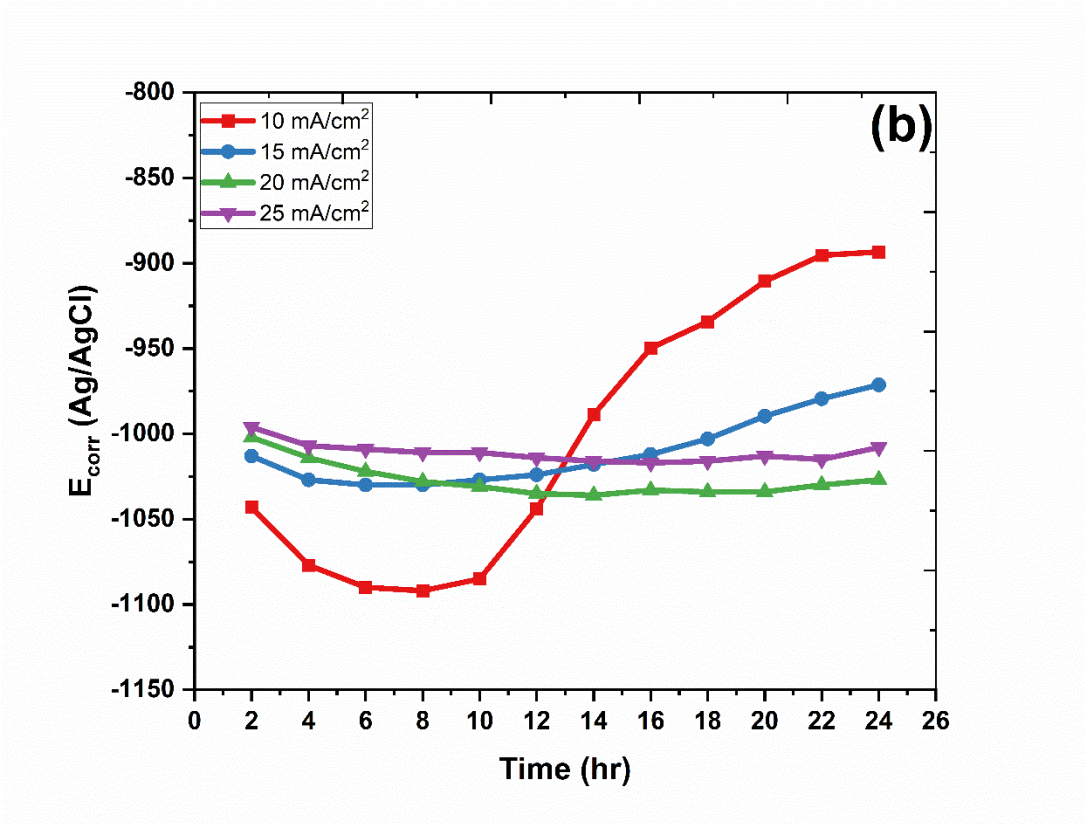

Fig. 25. Evolution of E_{corr} determined from LPR measurements in 0.5 M solution of NaCl for 24 hours exposure of the steel samples electrodeposited with Zn-Fe-W alloy coatings from (a) Na_2SO_4 and (b) $(NH_4)_2SO_4$ base galvanic baths at different current densities

As shown in Figure 26a, the polarization resistance (R_p) values of coatings deposited at different current densities using the Na_2SO_4 base galvanic bath are presented. Among these samples, it is observed that the coating deposited at a current density of 20 mA cm^{-2} has shown a higher initial value of R_p, which is approximately 8.0 kΩ cm^2, and this value remains higher after 24 hours of immersion. This is definitely an indication of higher corrosion resistance, which can be attributed to its compact, uniform, and strongly developed microstructure. However, there is a decrease in these values with time, which could be attributed to some kind of degradation process at the interface.

At higher current density, 25 mA cm^{-2}, there is a decrease in polarization resistance values. This can also be attributed to microstructural features such as higher grain sizes and surface irregularities that may allow easy electrolyte access, which could lead to reduced coating quality. The lowest values for polarization resistance, about 0.5 kΩ cm^2, are observed for samples deposited at 10 mA cm^{-2} and 15 mA cm^{-2}. This is attributed to low corrosion

resistance, which is due to the formation of a porous coating layer generally observed at low values of current density.

The corresponding values of R_p for the coatings deposited from the ammonium-containing bath are shown in Fig. 26b. Again, like the ammonium-free counterpart, the coating deposited at 20 mA cm^{-2} generally shows higher initial values of R_p, approximately 4.0 kΩ cm^2, which reflects better corrosion resistance due to relatively fast deposition rates and a more compact layer. An increase in current density to 25 mA cm^{-2} results in a decrease in R_p to approximately 3.0 kΩ cm^2, which can be attributed to defects such as coarse grains and, to some extent, localized regions.

At 15 mA cm^{-2}, both polarization resistance values decrease to approximately 2.0 kΩ cm^2, which could be attributed to higher surface roughness and less controlled growth processes. The lowest polarization resistance is achieved at 10 mA cm^{-2}, showing a sharp decrease to approximately 0.5 kΩ cm^2. This could be attributed to a very porous, irregular microstructure. The results obtained make it very evident that the bath composition and current density exert a strong effect on the electrochemical behavior of the Zn-Fe-W deposits.

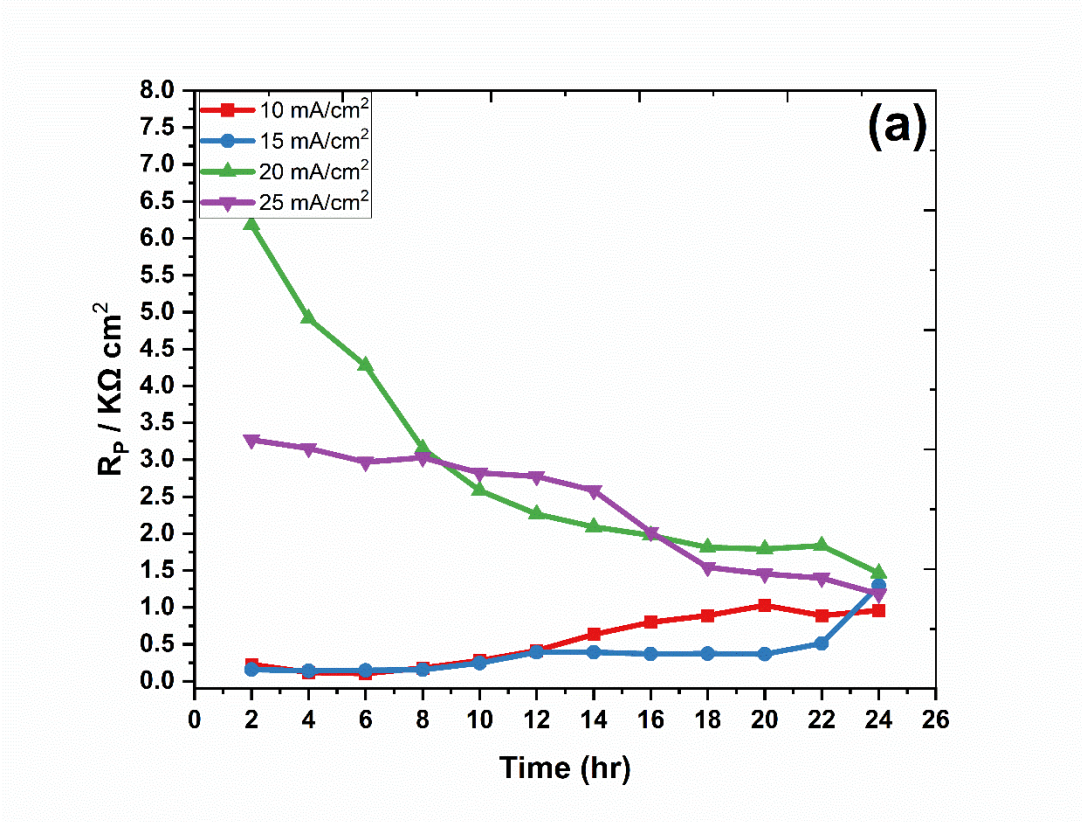

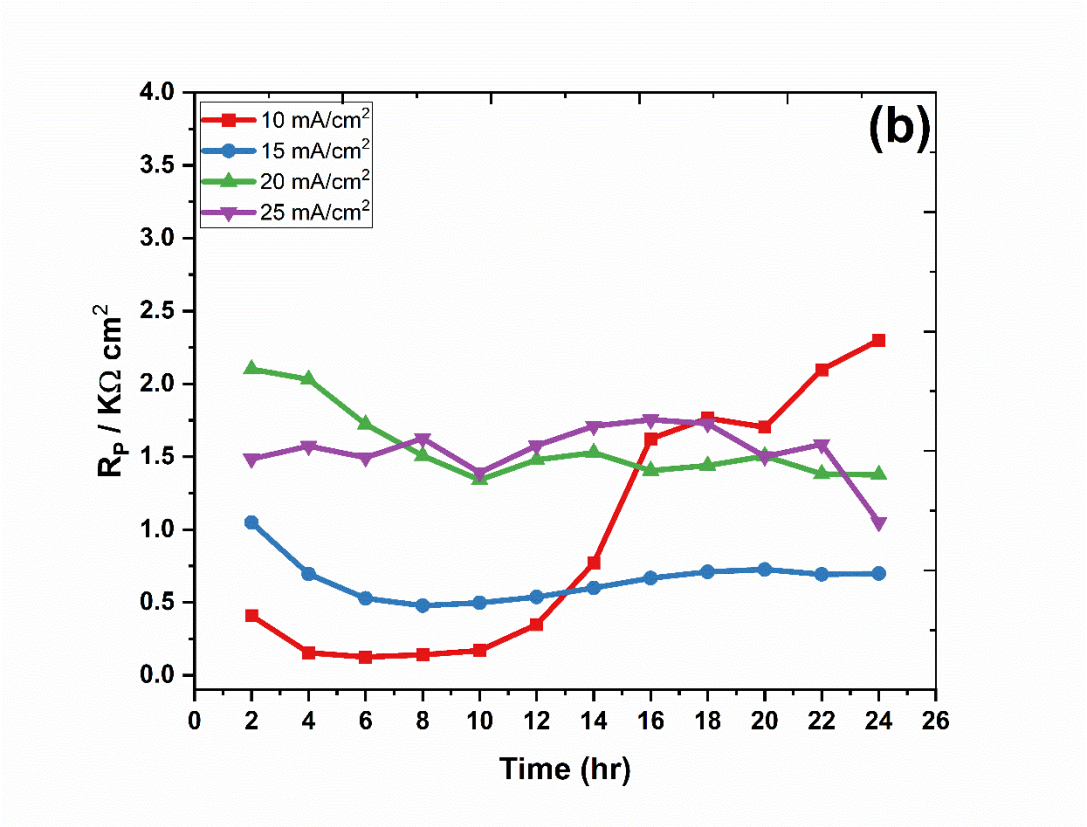

Fig. 26. Evolution of the polarisation resistance R_p calculated from LPR measurements in a 0.5 M solution of NaCl for 24 hours exposure of the steel samples electroplated with Zn-Fe-W alloy coatings from (a) Na_2SO_4 and (b) $(NH_4)_2SO_4$ base galvanic baths at different current densities.

Potentiodynamic polarization studies provide additional information on the corrosion characteristics of the Zn–Fe–W alloys deposited from both electrolytes. In Table 8, the Tafel slopes of anodic and cathodic reactions are found to be within the expected limits of a typical zinc-based alloys system, signifying proper curve fitting and clear activation-controlled reactions. In Table 8, in the case of Na_2SO_4 electrolyte, the coating deposited at a current density of 15 mA cm^{-2} had the highest i_{corr} value of 5.8 µA cm^{-2}, in line with its reduced impedance components and signifying the poorest microstructure quality due to its defective nature. In contrast, the i_{corr} values of the coating layers deposited at a current density of 20 mA cm^{-2} and 25 mA cm^{-2} were found to be lower (3.4 µA cm^{-2} and 3.9 µA cm^{-2}), indicating better barrier quality, as exemplified by the linear polarization resistance (LPR) measurement of the high corrosion potential, and the polarization resistance noted at higher current densities. Furthermore, the iron content (Fe wt.%) and the distinct phase structures present within the Zn-Fe alloy are additional factors that can significantly affect the corrosion performance of the coatings, as supported by previous studies[121]. Similar observations were noted in the

case of $(NH_4)_2SO_4$ electrolyte solution also. In this case, the least i_{corr} value of 7.9 µA cm^{-2} was noted when the coating was electrodeposited at a current density of 15 mA cm^{-2}. There is also a sudden increase of E_{corr} and R_p noticed for the current density of 15 mA cm^{-2} in linear polarization (LPR) measurements after 24 hours of exposure. However, there's a large jump in i_{corr} value noted at the next current densities of 20 mA cm^{-2} and 25 mA cm^{-2}, signifying the poor quality at this medium electrodepositing current density value.

This pronounced degradation in performance suggests that the coating's initial protection was not stable over extended exposure. One possible explanation for this behavior could be the relatively high iron content (Fe wt.%) in the alloy, which may have contributed to accelerated corrosion processes. A higher Fe content can alter the microstructure and phase distribution within the coating, potentially leading to less stable corrosion-resistant phases or galvanic interactions that promote localized corrosion. Therefore, the combination of deposition conditions and compositional factors appears to play a crucial role in the long-term corrosion behavior of these coatings.

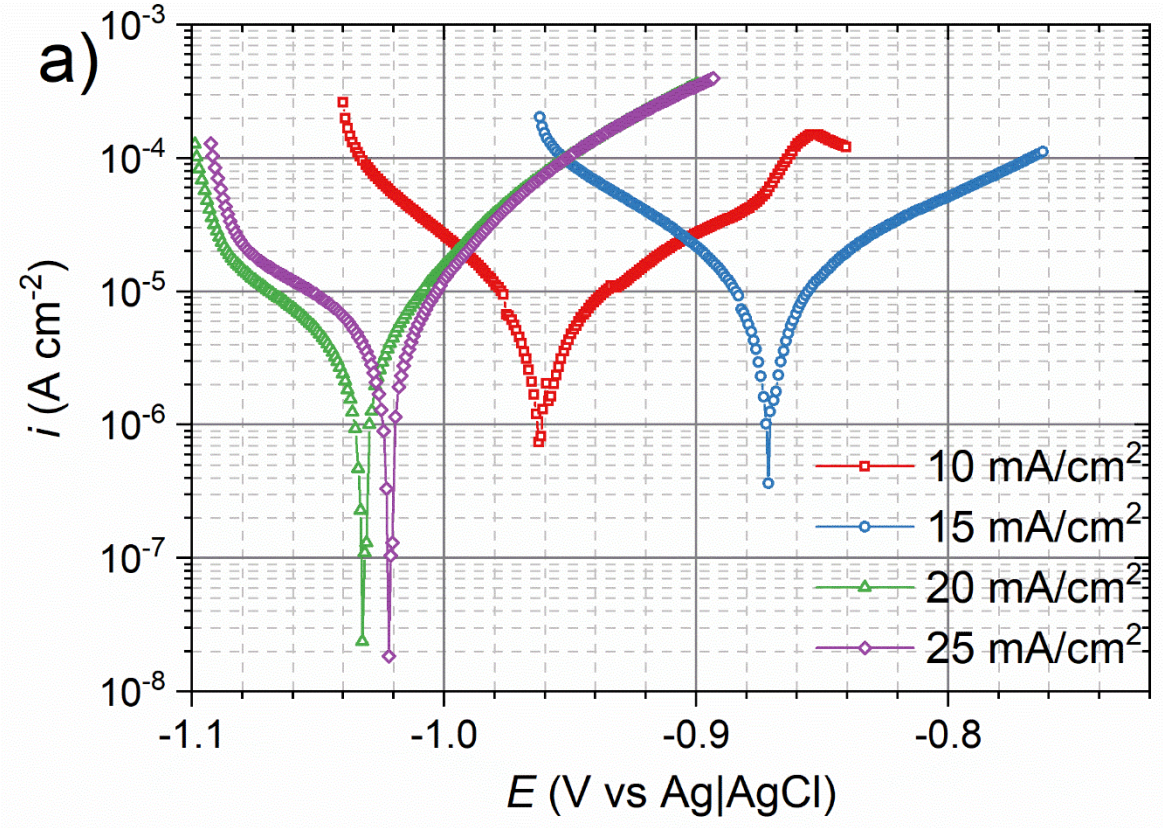

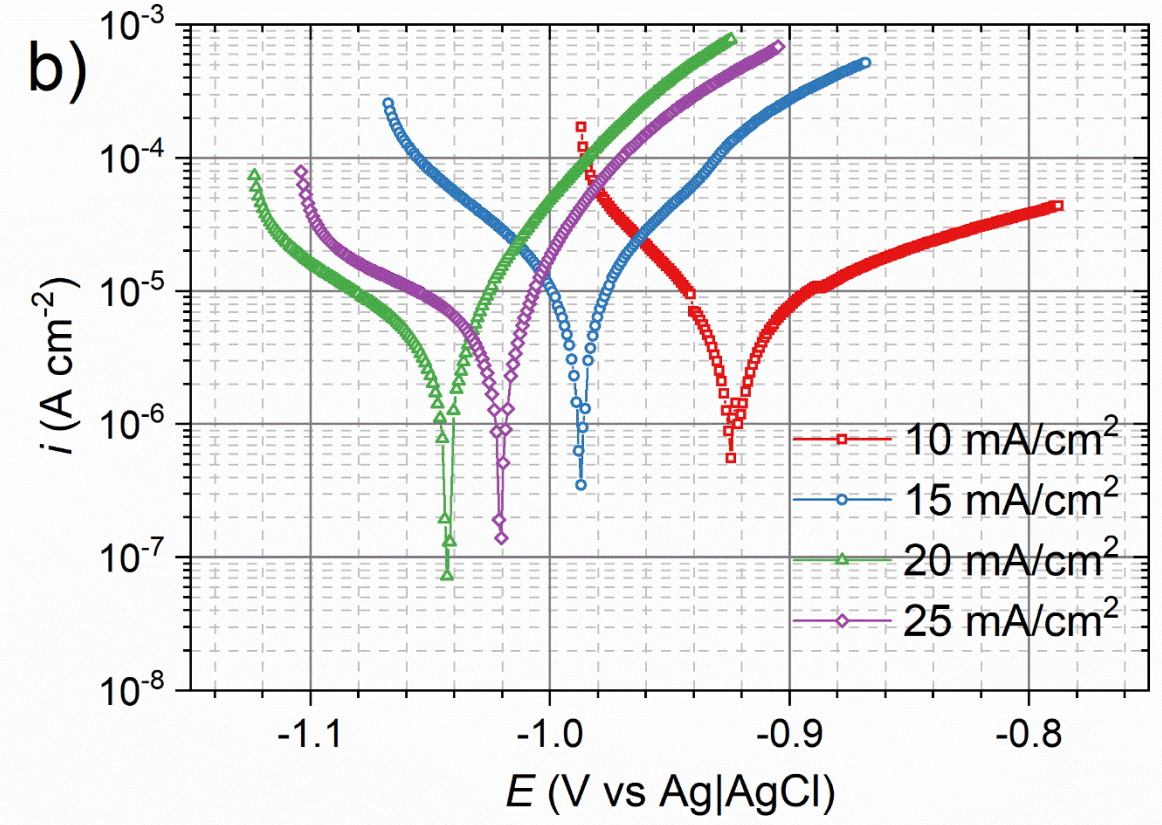

Fig. 27. Polarization curves of Zn-Fe-W alloy coatings deposited at different current densities from plating baths containing (a) Na_2SO_4 and (b) $(NH_4)_2SO_4$ salt, recorded after 24 hours of exposure of the samples in 0.5 M solution of NaCl

Table 8. Corrosion parameters estimated from potentiodynamic polarization curves recorded for Zn-Fe-W alloy coatings deposited at different current densities from plating baths containing Na_2SO_4 or $(NH_4)_2SO_4$

Parameter	Na_2SO_4 plating bath current density (mA cm^{-2})				$(NH_4)_2SO_4$ plating bath current density (mA cm^{-2})			
	10	15	20	25	10	15	20	25
β_a (mV dec^{-1})	89.8	57.4	50.0	44.4	106	48.4	28.1	27.2
β_c (mV dec^{-1})	56.3	48.3	78.4	74.0	53.9	57.9	53.6	63.3
i_{corr} (μA cm^{-2})	5.7	5.8	3.4	3.9	4.7	7.9	2.4	3.2
E_{corr} (mV vs Ag|AgCl)	-961.6	-870.8	-1033	-1022	-924.5	-987.4	-1043	-1021

Electrochemical Impedance Spectroscopy (EIS) was utilized to investigate the corrosion response of electrodeposited coatings in a corrosive environment with high chloride content, with particular focus on the influence of different sulphate salts utilized in the plating baths. The electrical elements of the equivalent circuit model shown in Figure 28 can be described as follows. The element R_1 is the bulk electrolytic solution resistance, a measure of ionic medium conductivity. CPE1 (Constant Phase Element) and R_2 account for capacitive and resistive behavior of the surface layer, including those resulting from oxide or hydroxide films and exterior metallic surface porosity. CPE2 and R_3 describe capacitive and resistive responses associated with the corrosion process occurring at the electrolyte/metal interface. Such an equivalent circuit is utilized to model the electrochemical behavior of metal coatings, particularly for the zinc and zinc alloy systems, since it can handle both the corrosion mechanism and the surface film characteristics.

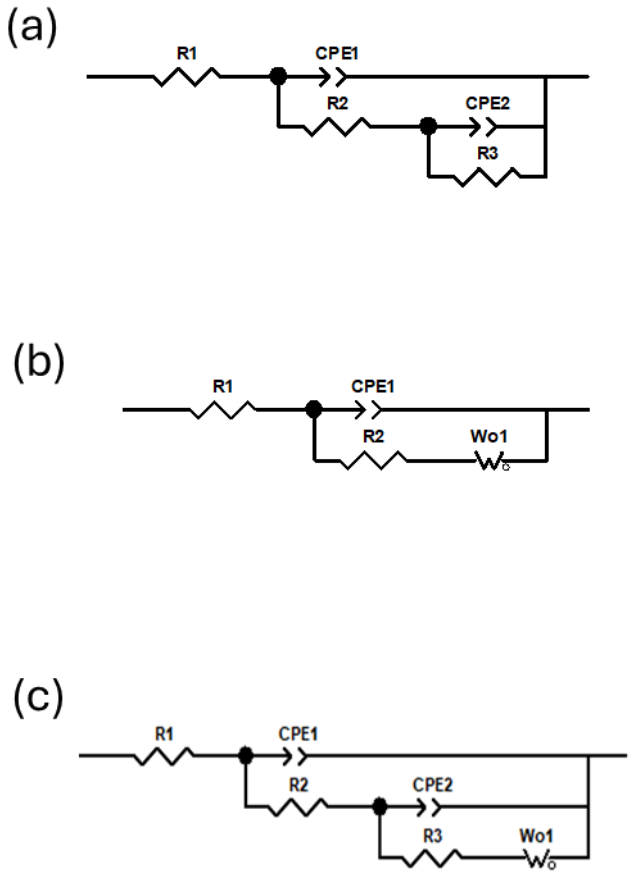

Fig. 28. Electric equivalent circuits used to fitting the impedance spectra recorded for the Zn-Fe-W alloy coatings after 24 hours of exposure of the samples in 0.5 M solution of NaCl.

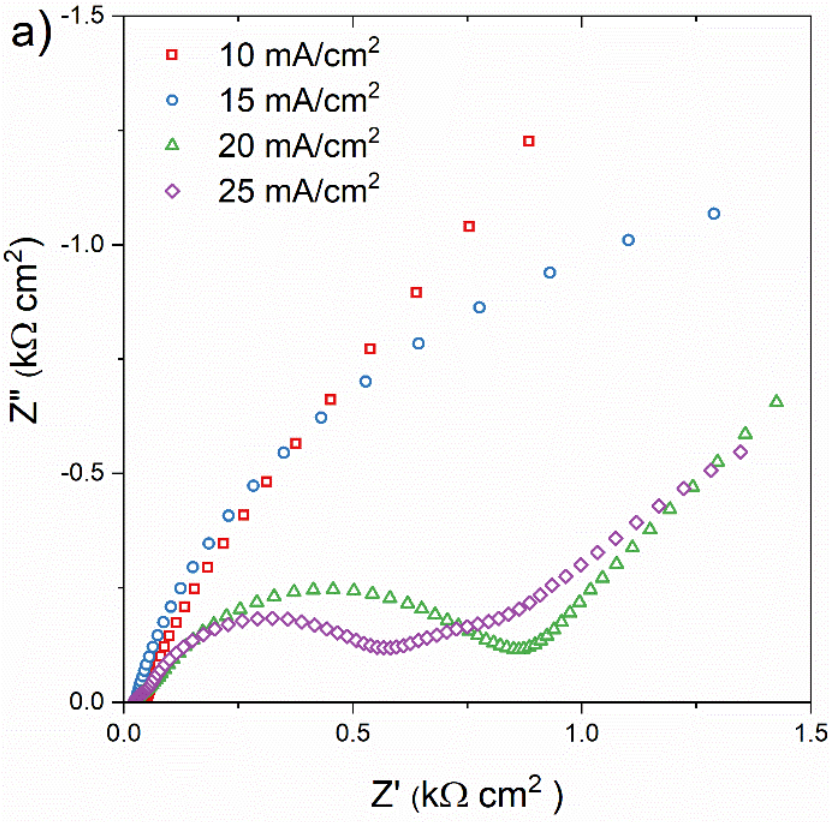
a)
10 mA/cm2
15 mA/cm2
20 mA/cm2
25 mA/cm2
Z'' (kΩ cm2)
Z' (kΩ cm2)
-1.5
-1.0
-0.5
0.0
0.0
0.5
1.0
1.5

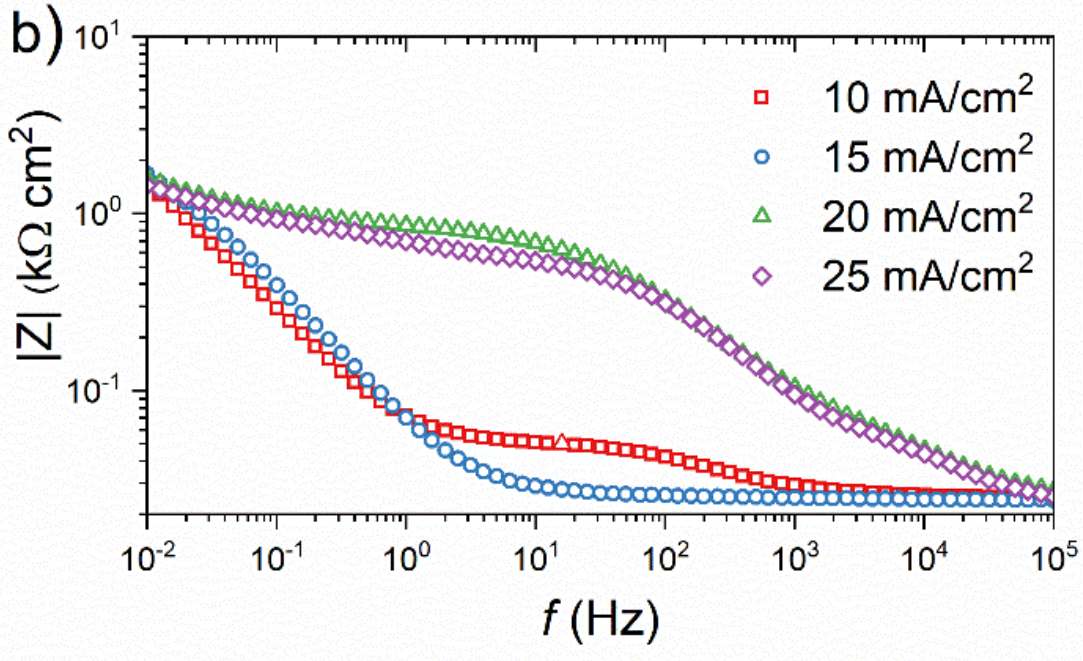
b)
10 mA/cm2
15 mA/cm2
20 mA/cm2
25 mA/cm2
|Z| (kΩ cm2)
f (Hz)
10^1
10^0
10^-1
10^-2
10^-1
10^0
10^1
10^2
10^3
10^4
10^5

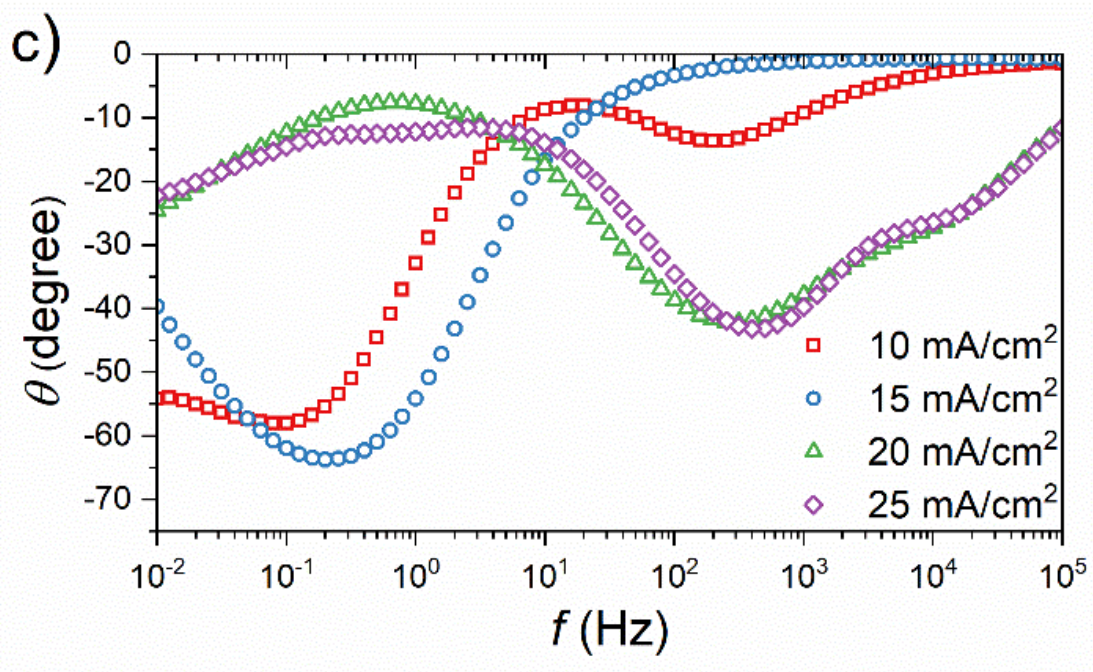

Fig. 29. Nyquist (a) and Bode (b, c) plots of the impedance spectra of Zn-Fe-W alloy coatings deposited from plating bath containing Na_2SO_4 salt, recorded after 24 hours of exposure of the samples in 0.5 M solution of NaCl.

Table 9. Fitting results for the impedance spectra of Zn-Fe-W alloy coatings deposited from the plating bath containing Na_2SO_4 salt, recorded after 24 hours of exposure of the samples in 0.5 M solution of NaCl.

Electrodeposition current density (mA cm^{-2})	R_1 (Ω cm^2)	CPE_1-T (Ω^{-1} cm^{-2} s^P)	CPE_1-P	R_2 (Ω cm^2)	CPE_2-T (Ω^{-1} cm^{-2} s^P)	CPE_2-P	R_3 (kΩ cm^2)
10	25 (1)*	2.49×10^{-4} (23)	0.73 (4.2)	30 (3.8)	5.10×10^{-3} (1.5)	0.82 (0.9)	3.5 (6.2)
15	24 (0.9)	1.83×10^{-3} (26)	0.70 (4.7)	25 (29)	1.87×10^{-3} (25)	0.92 (3.5)	2.9 (5.7)
20	24 (1.8)	5.28×10^{-5} (4.2)	0.60 (0.8)	910 (1.5)	6.92×10^{-3} (8.8)	0.71 (6.8)	3.2 (36)
25	24 (1.8)	4.42×10^{-5} (6.1)	0.62 (1.1)	630 (3.2)	3.43×10^{-3} (5.5)	0.5 (9.7)	6.6 (85)

* Values in brackets are the % error

Table 10. Fitting results for the impedance spectra of Zn-Fe-W alloy coatings deposited from the plating bath containing Na_2SO_4 salt, with Warburg correction

Electrodeposition current density (mA cm^{-2})	R_1 (Ω cm^2)	CPE_1-T (Ω^{-1} cm^{-2} s^P)	CPE_1-P	R_2 (Ω cm^2)	CPE_2-T (Ω^{-1} cm^{-2} s^P)	CPE_2-P	R_3 (kΩ cm^2)
10	25 (1)*	2.49×10^{-4} (23)	0.73 (4.2)	30 (3.8)	5.10×10^{-3} (1.5)	0.82 (0.9)	3.5 (6.2)
15	24 (0.9)	1.83×10^{-3} (26)	0.70 (4.7)	25 (29)	1.87×10^{-3} (25)	0.92 (3.5)	2.9 (5.7)
20**	25 (1.4)	4.75×10^{-5} (3.8)	0.61 (0.7)	847 (1.4)	_	_	_
25***	24 (2.0)	4.30×10^{-5} (6.1)	0.62 (1.1)	641 (3.2)	4.21×10^{-3} (12.5)	0.58 (15)	0.89 (40)

* Values in brackets are the % error

**W_o-T =4.79×10^{-5} (3.2), W_o-P=17.2(0.10)

***W_o-T = 1.13×10^{-2} (24.4), W_o-P= 3.94 (1.06)

The result of the fitting method, along with the corresponding error values (in brackets), is provided in Table 9. The goodness of the fits, in the form of the chi-squared (χ^2) values, was in the range from 1.5×10^{-5} to 5×10^{-4}, thereby indicating a good agreement between the experimental data and the proposed equivalent circuit model. The impedance spectra obtained from the Zn–Fe–W alloy coatings deposited at different current densities exhibit distinct differences in their electrochemical behavior following 24 h exposure in 0.5 M NaCl solution. In Table 9 for all samples, the solution resistance (R_1) was seen to be essentially unchanged (24–25 Ω cm^2) suggesting that changes in deposition current density have no significant impact on either the electrolyte or cell resistance and that variations in impedance response can be ascribed to changes in the coating structure.

Parameters of CPE1 reflect the dielectric properties of the outer coating layer. One can see that CPE1-T decreases noticeably with increasing current density from 10 to 25 mA cm^{-2}, while the CPE1-P exponent decreases only slightly. This indicates that coatings obtained at higher current densities are characterized by a denser and less porous microstructure. Lower effective capacitance corresponds typically to fewer defects in the coating, which agrees with the denser deposits formed at higher current densities.

R_2 significantly increased in coatings deposited at 20 and 25 mA cm^{-2}, attaining values around or above 0.6 kΩ cm^2, as compared with those obtained for 10 and 15 mA·cm^{-2}, which were substantially lower. The significant increase in R_2 points to a decreased rate of corrosion reactions at the metal/coating interface, confirming that coatings deposited at higher current densities exhibit superior protection against corrosion induced by chloride ions. This is also in agreement with the trend shown by the second CPE, CPE2, whose exponent decreases with the increase in current density, evidencing an enhancement of interfacial heterogeneity while the composition and microstructure of the alloy evolve.

Barrier or diffusion-related resistance, R_3, showed the most pronounced improvement in corrosion resistance. At 25 mA cm^{-2}, a high value of R_3 as much as 6.6 kΩ cm^2 was obtained, nearly double those determined at lower current densities. Such an increase indicates the growth of a superior quality barrier layer that is more able to impede ion permeation and retard the kinetics of corrosion processes. While the % error for R_3 determined at the higher current density was found to be greater, the extent of its increase still shows marked improvement in coating performance.

The samples with higher current density (20 and 25 mA cm^{-2}) showed a high percentage of fitting error (Table 9), as the diffusion-controlled processes were not included in the initial model fig. 28(a).

From the Nyquist diagram for the 20 mA/cm^2 sample, a 45° tail is observed at low frequencies, indicating semi-infinite diffusion. For the 25 mA/cm^2 sample, three time constants are observed, one of which is a 45° diffusion tail, showing the effect of mass transport.

In order to improve the fitting results for the 20 and 25 mA cm^{-2}, samples, a Warburg element was included (Table 10). The W_o element helped in improving the results by reducing the parameter uncertainty. For the 20 mA cm^{-2} sample, the Warburg element is sufficient to explain the diffusion controlled processes, with an additional to capacitive elements fig. 28(b). For the 25 mA cm^{-2} sample, the Warburg element and multiple time constants are required fig. 28(c), showing the complexity of the structure and corrosion processes at high current density.

Generally, the results obtained from EIS studies show that an increase in electrodeposition current density improves the protective performance of Zn–Fe–W alloy coatings. The coatings obtained at 20–25 mA cm^{-2} present a denser morphology, lower effective capacitance, and remarkably higher charge-transfer and barrier resistances. In contrast, those coatings obtained at 10–15 mA cm^{-2} exhibit lower resistance values and higher capacitance responses, which

indicate more defective and permeable structures. According to the impedance response, the coating obtained at 25 mA cm^{-2} presents the most favorable corrosion protection characteristics under the tested conditions.

Table 11. Fitting results for the impedance spectra of Zn-Fe-W alloy coatings deposited from plating bath containing $(NH_4)_2SO_4$ salt, recorded after 24 hours of exposure of the samples in 0.5 M solution of NaCl.

Electrodeposition current density (mA cm^{-2})	R_1 (Ω cm^2)	CPE_1-T (Ω^{-1} cm^{-2} s^P)	CPE_1-P	R_2 (Ω cm^2)	CPE_2-T (Ω^{-1} cm^{-2} s^P)	CPE_2-P	R_3 (kΩ cm^2)
10	26 (1.0)	2.79×10^{-4} (13)	0.68 (2.7)	58.8 (2.7)	4.72×10^{-3} (1.3)	0.86 (0.9)	7.0 (9.7)
15	27 (1.2)	1.00×10^{-3} (6.0)	0.48 (1.6)	344 (12)	2.92×10^{-4} (3.4)	1.0 (7.2)	0.93 (3.4)
20	25 (1.0)	1.58×10^{-4} (5.8)	0.66 (1.2)	510 (4.8)	1.6×10^{-3} (4.1)	0.62 (4.4)	2.1 (7.1)
25	24 (1.3)	1.46×10^{-4} (10)	0.63 (2.0)	225 (6.3)	1.58×10^{-3} (2.3)	0.55 (3.5)	1.98 (6.4)

It can be seen that the impedance behavior of Zn–Fe–W alloy coatings deposited from the $(NH_4)_2SO_4$ containing electrolyte exhibits significant corrosion performance differences as a function of electrodeposition current density. In Table 11, the values of R_1 for all samples remained almost identical, and only slight variations were observed between 24 and 27 Ω cm^2. This consistency assures that the observed differences in impedance response originate from structural and compositional changes in the coatings themselves rather than from changes in the test medium.

The dielectric properties of the outer coating layer, represented by CPE1, present a clear dependence on current density. The values of CPE1-T decreased from 10 to 25 mA cm^{-2}, suggesting a decrease in coating capacitance and pointing out that the coatings are more compact for higher values of current density. It is also possible to observe variations of the exponent CPE1-P, with an accentuated decrease at 15 mA cm^{-2} (0.48), indicating heterogeneous structure and diffusion through a porous layer. For 20 and 25 mA·cm^{-2}, the values of CPE1-P recover to ~0.63–0.66, reflecting a heterogeneous surface and closer to a homogeneous surface compared to the coating deposited at 15 mA·cm^{-2}.

Charge-transfer resistance, R_2, increased with increasing current density, passing through a maximum at 20 mA cm^{-2} (0.5 kΩ cm^2); this increase in charge-transfer resistance indicates a decrease in corrosion rate and better interfacial protection at higher current density. Coatings deposited at 15 mA cm^{-2} presented a significantly lower R_2 value (0.3 kΩ cm^2), in agreement with higher capacitance and higher heterogeneity of CPE1 parameters. This can be related to a microstructure with more defects or discontinuities at 15 mA cm^{-2}, which decreases their electrochemical stability.

Further evidence is provided by the behavior of CPE2: the CPE2-P exponent decreased progressively with the increase in current density, from nearly ideal capacitive behavior at 15 mA cm^{-2} ($P \approx 1.0$) to substantially lower values at 20 and 25 mA cm^{-2} (0.62–0.55). This trend suggests an increase in interfacial complexity, which also corresponds to an increased heterogeneity consistent with alloy co-deposition at higher applied currents. Nevertheless, the corresponding resistance values suggest enhanced protection.

R_3 presented the strongest response at low current density, reaching as high as 7.0 kΩ cm^2 at 10 mA cm^{-2}. This unusually high R_3 value at low current density may suggest that this coating has a particularly effective diffusion barrier, possibly due to either a smoother surface or more favorable alloy distribution. At intermediate current densities, specifically 15 mA cm^{-2}, R_3 shows a sharp decline to 0.93 kΩ cm^2, reflecting poorer barrier properties that are probably linked to increased porosity and/or microstructural irregularities. At higher values of 20 and 25 mA cm^{-2}, R_3 rises moderately to ca. 2.0 kΩ cm^2, indicating the partial recovery of barrier performance with increasing deposition rate, where the coating becomes denser and more uniform. The impedance response of Zn–Fe–W coatings deposited from the $(NH_4)_2SO_4$ bath shows that corrosion protection is extremely sensitive to current density, but trends differ from those in the case of coatings prepared from the Na_2SO_4 containing bath. While the highest barrier resistance corresponds to low (10 mA cm^{-2}) current density, the best compromise between charge-transfer resistance, capacitive behavior and structural compactness is attained by coatings deposited at 20 mA cm^{-2}. By contrast, the coating deposited at 15 mA cm^{-2} displays comparatively poor protection due to higher capacitance, increased heterogeneity and reduced resistive parameters. These findings demonstrate the complex interaction among deposition conditions, alloy composition and microstructural features as influencing factors for the corrosion performance of Zn–Fe–W coatings.

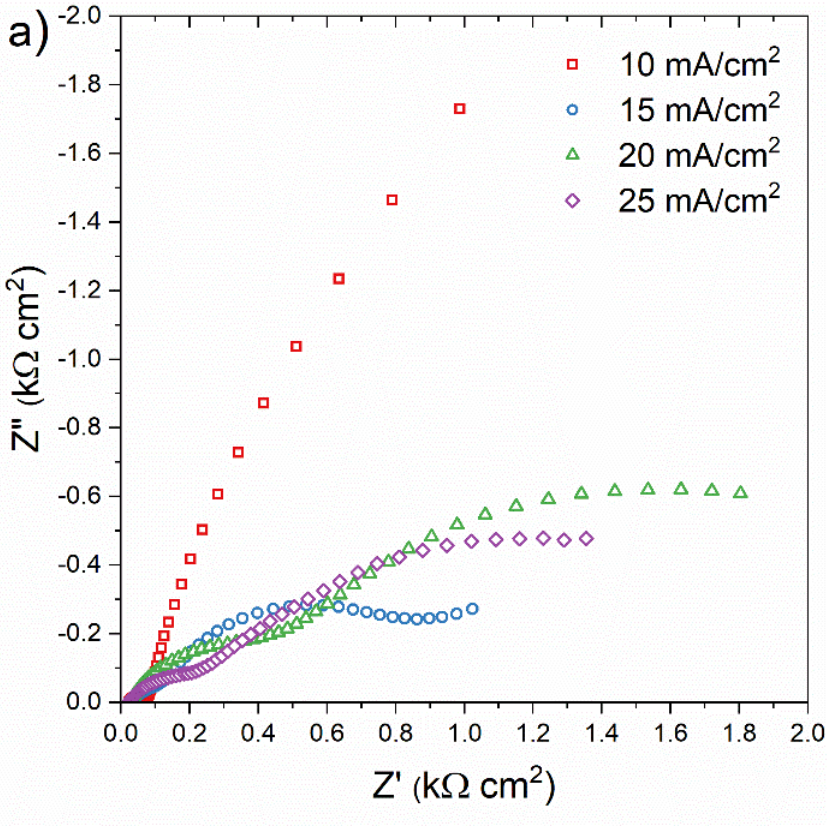
a)
10 mA/cm2
15 mA/cm2
20 mA/cm2
25 mA/cm2
Z'' (kΩ cm2)
Z' (kΩ cm2)
-2.0
-1.8
-1.6
-1.4
-1.2
-1.0
-0.8
-0.6
-0.4
-0.2
0.0
0.0
0.2
0.4
0.6
0.8
1.0
1.2
1.4
1.6
1.8
2.0

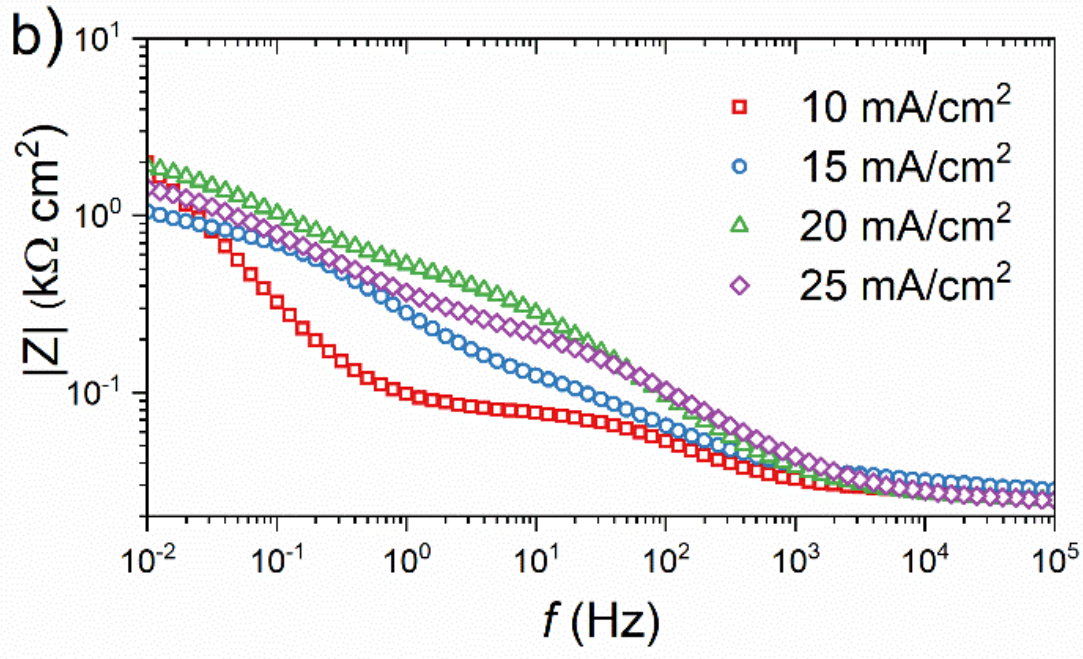
b)
10 mA/cm2
15 mA/cm2
20 mA/cm2
25 mA/cm2
|Z| (kΩ cm2)
f (Hz)
10^1
10^0
10^-1
10^-2
10^-1
10^0
10^1
10^2
10^3
10^4
10^5

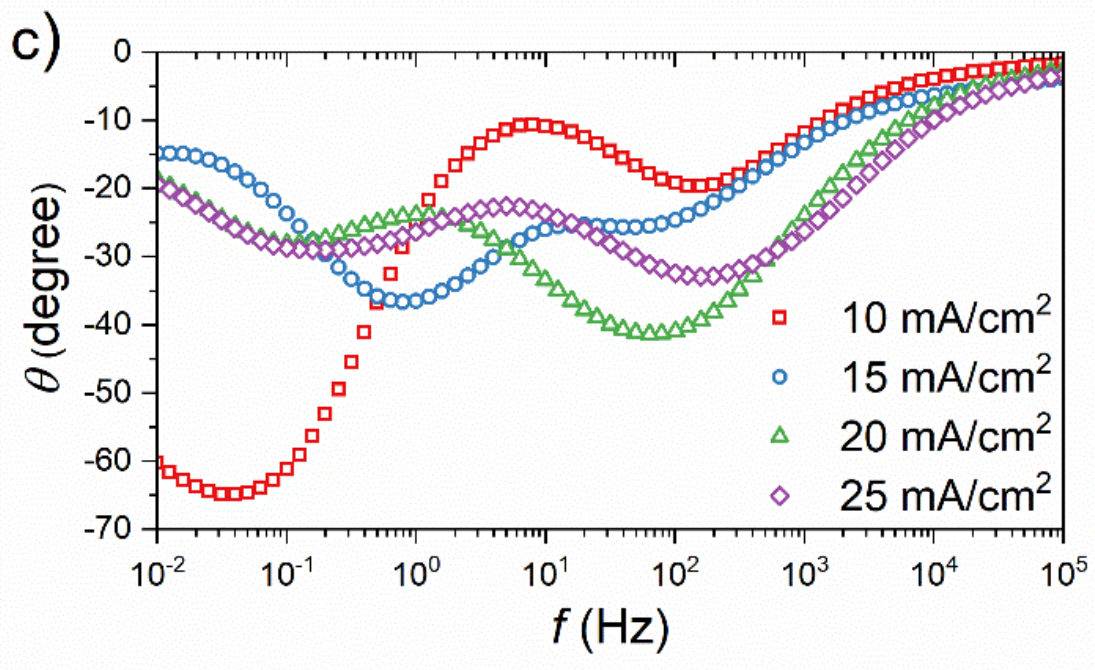

Fig. 30. Nyquist (a) and Bode (b, c) plots of the impedance spectra of Zn-Fe-W alloy coatings deposited from plating bath containing $(NH_4)_2SO_4$ salt, recorded after 24 hours of exposure of the samples in 0.5 M solution of NaCl.

Chapter 5

Conclusion

This work was dedicated to the electrodeposition process of Zn-Fe-Mo and Zn-Fe-W alloy coatings in sulfate plating baths at different plating parameters. By combining microscopic techniques, structural studies, electrochemical impedance spectroscopy analysis, potentiodynamic polarization measurements, and time-dependent UV-Vis spectroscopy analysis, the comprehensive examination of the influence of the electrodeposition process on the coatings performance/properties was achieved. The findings clearly demonstrate that parameters play a decisive role in controlling the deposition mechanism and the resulting coating properties.

5.1 Detailed conclusions related to the Cyclic Voltammogram and UV-Vis Spectroscopy:

- Electrochemical analysis showed that there are observable changes in the potentials for the oxidation and reduction of zinc (Zn reduction potential moves from -1.12 V vs. Ag|AgCl to -1.2 V vs. Ag|AgCl with the addition of ammonium sulphate and more negatively -1.25 V vs. Ag|AgCl with the addition of sodium sulphate), iron (Fe reduction potential move from -0.4 V vs. Ag|AgCl to -0.8 V vs. Ag|AgCl with the addition of ammonium sulphate and more negative, -1.25 V vs. Ag|AgCl with the addition of sodium sulphate), for molybdenum, and tungsten co-reduction with Fe observed. Which may be facilitated through the use of mixed metal complexes of ammonium and citrate compounds.
- Analysis by UV-Vis spectroscopy indicates that the electrolyte undergoes continuous chemical alteration during the deposition process. This is expected to occur because of metal ion complexation reactions, polynuclear molybdate/tungstate formations, along with redox reactions of the transition metals. The stepwise reduction or consumption of metals, iron (peak related to 480nm), and molybdenum/tungstate (peak hump related to 650-880nm) was observed.

5.2 Detailed conclusions related to the morphology and composition of the coatings (SEM/EDXS):

5.2.1 Zn-Fe-Mo

The deposits formed at low current densities of 10 to 15 mA cm^{-2} were grayish and powdery for both baths, which was an indication of poor packing density. As the current density was raised to 20 to 25 mA cm^{-2}, the deposited coatings became smooth and fine grained. Furthermore, the presence of ammonium ions was found to significantly influence the microstructural development of the deposits, particularly at lower current densities. In the absence of ammonium ions, the coatings displayed porous, agglomerated particle structures, suggesting non-uniform nucleation and growth. Conversely, coatings deposited from ammonium-containing baths exhibited more developed and interconnected fibrous structures, indicating enhanced nucleation kinetics and more controlled growth behavior. Energy-dispersive X-ray (EDX) analysis showed that deposit made from baths with ammonium ions had a measurable amount of molybdenum from 3-5.0 wt.% at low current densities, and at high current densities decreased to below 1 wt.%; meanwhile, iron content increased up to 12.2 wt.%. As the current density increases, the amounts of molybdenum goes down a lot. In contrast, in the sodium sulphate base bath molybdenum amount tends to remain below 1 wt.%, and the iron content increases with an increase in current density.

5.2.2 Zn-Fe-W

Results from the SEM analysis showed that the coatings deposited from low current densities (10-15mA cm^{-2})possessed pores and coarse grains structures. Increasing the values of the current density to 20mA/cm^2 led to the deposition of more uniform and fine Zn-Fe-W coatings. Moreover, deposition from the highest values of the current density (25mA/cm^2) led to the deposition of coatings with non-uniform surfaces and irregular nodular structures with coarse grains. These structures are indicative of reduced microstructural control during deposition. Results from the EDX analysis also showed that the presence of ammonium in the baths led to the increased values of iron from 5-11 wt.% and tungsten 3-5 wt.% composition with the increase of current density. The values of tungsten are below 1 wt.% in the coatings deposited from the baths containing sodium sulphate. Moreover, the tungsten and iron values increased with the increased of the current density from 10-25mA cm^{-2}.

5.3 Detailed conclusions related to the topography (profilometry):

5.3.1 Zn-Fe-Mo

The surface roughness was found to be greater at low current densities in both the ammonium-based bath (Ra values of 0.76 µm, 0.17 µm) and ammonium ion-free baths (Ra values of 0.56 µm, 0.75 µm). As the current density was raised to 20–25 $mAcm^{-2}$, the surface roughness was found to have improved in both the ammonium-containing (Ra values of 0.091 µm, 0.048 µm) and ammonium-free baths (Ra values of 0.041 µm, 0.035 µm). This is an indication that the surface topography is finer at high current densities, irrespective of the bath composition.

5.3.2 Zn-Fe-W

At a lower current density range of 10 to 15 mA cm^{-2}, there is a large surface roughness (Ra value 0.94 µm, 0.62 µm) for ammonium-based, and (Ra value 1.25 µm, 1.18 µm) ammonium ions-free plating baths, correlating to rough, pore-ridden, and poorly adhered coatings. An increase in current density to 20 to 25 mA cm^{-2} leads to a large reduction in Ra (0.25 µm, 0.15 µm) for ammonium-based, and Ra (0.28 µm, 0.20 µm) for ammonium ions-free bath solutions, pointing towards smooth, dense coatings, corresponding to fine microstructures. Ammonium plating baths have a slightly lower Ra, attributing to efficient metal ion complexing and deposition.

5.4 Detailed conclusions related to the phase composition (XRD) and structure (TEM and SAED):

5.4.1 Zn-Fe-Mo

All coatings were found to be nanocrystalline in nature, exhibiting columnar growth made up of fibrous assemblies of oval-shaped crystallites with sizes between 20 and 40 nm, regardless of the bath composition. A uniform distribution of Zn, Fe, and Mo over the whole coating thickness was verified by elemental mapping, indicating stable co-deposition behavior. In contrast to the more randomly oriented microstructures seen in coatings deposited from ammonium ion-free baths, coatings generated from baths containing ammonium sulfate exhibited a strong crystallographic texture. The impact of ammonium ions on crystal growth orientation and microstructural development during electrodeposition is further highlighted by this texturing effect. Phase analysis using the X-ray diffraction technique revealed that the electroplated films were primarily made up of crystalline zinc and iron phases. Molybdenum was found in

neither metallic nor intermetallic forms; instead, the presence of Mo is assumed because of the lower concentration of the element that is below the detection limit of the XRD technique. With an increase in the current density values, the presence of iron-zinc intermetallic phases in the diffraction patterns became more prominent. The likely intermetallic phases included $Fe_{22}Zn_{78}$, $Fe_{11}Zn_{40}$, and hexagonal $FeZn_{10.98}$ phases.

5.4.2 Zn-Fe-W

FIB/SEM cross-sectional images of the 20 mA·cm^{-2}-coated samples reveal dense and columnar microstructure morphologies for both baths with significant differences at the interfaces. The ammonium ion-free bath sample has a dense columnar to equiaxed microstructure with slight interfacial microvoids and dark bands corresponding to early nucleation-related and hydrogen-related stresses. The ammonium ion-based bath sample has a dense matrix with localized interfacial microvoids as discrete microvoids, which may be due to increased hydrogen evolution and entrapments during early growth deposition. XRD analysis shows that when the current density was increased to 15 mA cm^{-2}, the iron peaks were suppressed and significant phase evolution was initiated. At low current density (10 mA cm^{-2}), metallic zinc predominated in the coatings with minor iron contributions. Metallic Zn and Fe phases vanished at higher current densities (20–25 mA cm^{-2}) and were replaced by Fe–Zn intermetallic phases, primarily $Fe_{22}Zn_{78}$, suggesting improved alloying under higher deposition rates. The low concentration of tungsten-related phases and the XRD detection limits prevented their detection.

5.5 Detailed conclusions related to the corrosion resistance:

5.5.1 Zn-Fe-Mo

Results of the corrosion potential measurement over 24 h revealed that the coatings obtained at higher current densities of 20–25 mA cm^{-2} have higher nobility in the initial stages, thus providing superior corrosion resistance properties. In ammonium ion-free bath samples, the specimen at 20 mA cm^{-2} had outstanding stability in its E_{corr} value, which remained relatively constant throughout. In contrast to this, the ammonium-ion based bath coating started with a transiently noble value of E_{corr} that decreased with time as the immersion time increased. The coatings produced from the ammonium bath

at low current densities (10-15 mA cm^{-2}) had E_{corr} shifting in the positive direction due to Mo-induced passivation caused by the high Mo content.

Linear polarization resistance data show R_p increases with the increase of current densities for the ammonium ion-free sapmles, and 20 and 25 mA cm^{-2} showed the best R_p after 24 h of exposure. Some variations in R_p were seen at shorter exposure times, especially for the higher Fe content samples. For the coating obtained from the ammonium ion-based solution, the R_p for the 20 mA cm^{-2} sample was very high initially and then decreased over time, indicating deterioration.

The potentiodynamic polarization current measurements after 24 hours of deposition indicated a decrease in anodic and cathodic currents with an increase in deposition current density, independent of bath solutions, which indicated improved corrosion resistance properties. The value of i_{corr} ranged from 0.3-1 µA cm^{-2}, which indicated excellent performance of the coatings. The value of i_{corr} increased with a decrease in current density for the coatings in the ammonium ion-free bath solution. On the other hand, the i_{corr} values for the coatings from the bath containing ammonium ion were generally lower (better resistance), with the exception for 20 mA cm^{-2}, which had the highest i_{corr} value. This is consistent with the LPR data, indicating high levels of Fe and unstable phase distribution for this current favor corrosion reactions possibly due to galvanic or microstructural effects.

EIS analysis revealed the corrosion resistance and barrier properties of the coatings. In the case of ammonium ion-free bath samples, it was observed that the current density increased the values of impedance, R_2 from 0.1 to 7 kΩ·cm^2, and R_3 from 21 to about 75 kΩ cm^2 at a current density of 25 mA cm^{-2}. The values of capacitance decreased, and the exponents of CPE increased due to increased homogeneity and reduced porosity of the coating due to increased current density. The impedance of the ammonium bath coating was even higher, but the behavior was more complex. Diffusion-controlled behavior at 10 mA cm^{-2} required a Warburg component because of the powdery, porous morphology that inhibited ionic diffusion. However, at larger current densities, the impedance behavior indicated enhanced surface smoothness and resistance to corrosion.

5.5.2 Zn-Fe-W

The E_{corr} measurements revealed that the coatings deposited at higher current densities of 20-25 mA cm^{-2} in Na_2SO_4 and in $(NH_4)_2SO_4$ solutions had higher and nobler

corrosion potential values of about -1000 mV Ag|AgCl. This can be attributed to the dense and tight microstructure. Lower current densities of 10-15 mA cm^{-2} showed lower corrosion potential values at the beginning, and then the potential slowly moved towards nobility. This can be attributed to interface reactions due to higher surface roughness and corrosion activity.

Linear polarisation resistance measurements further substantiated these results. In both electrolytes, the coating deposited at a current density of 20 mA cm^{-2} presented the highest values of R_p (8.0 kΩ·cm^2), thereby reflecting enhanced corrosion resistance with dense deposits. On the other hand, the coating deposited at a current density of 10 mA cm^2 presented the lowest values of R_p (approximately 0.5 kΩ cm^2), thereby reflecting the defective microstructures. The decrease in R_p with the current density of 25 mA cm^{-2} suggests that high current density can lead to the deterioration of coating quality due to grain coarsening and surface topography.

The results of the potentiodynamic polarisation tests supported the LPR results. For the ammonium ion-free bath, the coatings deposited at current densities of 20 and 25 mA cm^{-2} had smaller i_{corr} values (3.44 µA cm^{-2} and 3.91 µA cm^{-2}) compared to those deposited at smaller current densities. On the other hand, the coatings deposited at a current density of 15 mA cm^{-2} had the largest i_{corr} values (5.8 µA cm^{-2}), which correlated well with their poor microstructures. For the ammonium ion-based bath, although there was a temporary enhancement of E_{corr} and R_p at a current density of 15 mA cm^{-2} also higher i_{corr} (7.86 µA cm^{-2}), the substantial increase in i_{corr} at higher current densities indicated the instability of the first layer formation, which could be attributed to the higher iron content.

EIS studies show that increasing the current density for ammonium ion-free based coatings led to a reduction in the effective capacitance (CPE1-T), an increase in the R_2 (0.03 to 0.63 kΩ cm^2), and a substantial increase in the R_3 to a maximum of 25 mA cm^{-2} (approximately 6.6 kΩ cm^2). The above observations strongly indicate the development of a dense coating with lower porosity and enhanced resistance at a high current density. The coating at 10-15 mA cm^{-2} had a higher capacitance and lower resistance values. The coatings deposited from the ammonium ion bath show more complex results. Although the highest value of R_3 occurred at 10 mA cm^{-2}, this did not correspond to optimal charge transfer resistance and capacitance. Rather, coatings deposited at 20 mA cm^{-2} showed the best overall trade-off between compactness, interface stability, and corrosion resistance. The lowest results were always found for

coatings deposited at 15 mA cm^{-2}, which showed enhanced inhomogeneity, capacitance, and lower resistance values.

5.3 Key Findings:

Thus, in the broad field of electrodeposition research, the work presented in the current manuscript not only enlarges the scope of multi-component alloy electrodeposition research but also indicates the crucial role of both optimized current density values and controlled electrolyte compositions in achieving corrosion-resistant coatings.

- These experiments revealed that the current density was an extremely crucial parameter in controlling the coating morphology, compactness, and electrochemical properties.
- In the microstructural analysis, current density and chemical composition are the dominant factors influencing the deposition behavior, composition, and microstructure in Zn-Fe-Mo and Zn-Fe-W alloys. Ammonium ion-containing baths enable co-deposition of Mo or W by metal-ammonia or citrate complexes, produce nanocrystalline, textured, fibrous, or columnar deposits, and facilitate uniform elemental distribution. Higher current density leads to finer surface morphology, from rough, powder-like, and porous at low current density to dense, smooth, and uniform at approximately 20 mA cm^{-2}, but excessive current density induces compositionally irregular, coarser deposits, and reduced control. Cross-sectional views by FIB/SEM analysis indicate relatively dense films across the thickness, but ammonium ion-containing baths can produce localized interfacial porosity due to the evolution of hydrogen gas at the initial stages of deposition.
- In the Zn-Fe-Mo and Zn-Fe-W alloys, the surface roughness and morphology are largely affected by the cathodic current density, while the composition of the electroplating bath is of secondary importance, with lower current densities (10-15 mA cm^{-2}) giving rough, porous, and poorly adherent surfaces due to irregular and large-grained morphology, while higher current densities (20-25 mA cm^{-2}) give much smoother and more refined surfaces, with ammonium-containing baths giving slightly better refinement of the surfaces.
- From the XRD analysis, it was found that, in case of both Zn–Fe–Mo and Zn–Fe–W alloy coatings, the major controlling factor is the value of current density, where low current densities are conducive to the formation of metallic zinc and trace iron, and higher current densities (20-25 mA cm^{-2}) are conducive to the development of Fe-Zn

intermetallic compounds, specifically $Fe_{22}Zn_{78}$, and that no peaks corresponding to Mo and W phases are detected because their concentration and dispersivity are below the detection limit of XRD.

- The overall electrochemical analysis reveals that Zn-Fe-Mo or Zn-Fe-W coatings deposited under moderate to high current densities (approximating 20 mA cm^{-2}) provide maximum resistance to corrosion because of their more densely packed microstructures, lower defects, and higher interfacial or barrier resistances. Though higher values of current densities are desirable for higher resistance, particularly in Na_2SO_4 based electrolytes. However, in ammonium containing baths, enhanced initial protection may be offset by long-term instability, especially at intermediate current densities. The values above or different from the optimal values can lead to defects or compositional differences in microstructures, thereby affecting overall long-term properties.
- Collectively, these findings uncover how bath chemistry, current density, and alloy composition all impact Zn-Fe-Mo and Zn-Fe-W coating corrosion behavior. They also indicate that deposition parameter optimization would help balance short-term corrosion resistance with long-term superficial stability.

5.4 Future Work

On the basis of the findings of this thesis, the following areas can be identified for further exploration to improve the existing knowledge and applicability of the alloy coatings of Zn-Fe-W and Zn-Fe-Mo:

- Use the techniques of ICP-OES, Raman spectroscopy, or ESI-MS to directly observe the dynamic metal species concentration over time within the deposition bath.
- Examine the effect of agitation, temperature of the bath, and surfactants on coating uniformity and corrosion properties.
- Analyze heat treatment, annealing, or surface passivation for improving the hardness, adhesion, and corrosion protection of the coating.
- Perform salt spray, humidity, and natural weathering tests to relate laboratory electrochemical testing to actual field experience.

References

[1] A. C. Hegde, K. Venkatakrishna, and N. Eliaz, 'Electrodeposition of Zn–Ni, Zn–Fe and Zn–Ni–Fe alloys', *Surf. Coat. Technol.*, vol. 205, no. 7, pp. 2031–2041, Dec. 2010, doi: 10.1016/J.SURFCOAT.2010.08.102.

[2] R. Bhat, A. H.-J. of E. S. and, and undefined 2019, 'Studies on electrodeposited Zn-Fe alloy coating on mild steel and its characterization', *hrcak.srce.hrR Bhat, AC HegdeJournal of Electrochemical Science and Engineering, 2019•hrcak.srce.hr*, doi: 10.5599/jese.565.

[3] E. Chassaing, N. Portail, A. F. Levy, and G. Wang, 'Characterisation of electrodeposited nanocrystalline Ni-Mo alloys', *J. Appl. Electrochem.*, vol. 34, no. 11, pp. 1085–1091, Nov. 2004, doi: 10.1007/S10800-004-2460-Z.

[4] J. Winiarski, W. Tylus, M. Krawczyk, B. S.-E. Acta, and undefined 2016, 'The influence of molybdenum on the electrodeposition and properties of ternary Zn–Fe–Mo alloy coatings', *ElsevierJ Winiarski, W Tylus, MS Krawczyk, B SzczygiełElectrochimica Acta, 2016,* doi.org/10.1016/j.electacta.2016.03.027

[5] B. Szczygieł, A. Laszczyńska, and W. Tylus, 'Influence of molybdenum on properties of Zn-Ni and Zn-Co alloy coatings', *Surf. Coat. Technol.*, vol. 204, no. 9–10, pp. 1438–1444, Jan. 2010, doi: 10.1016/j.surfcoat.2009.09.042.

[6] A. Laszczyńska, W. Tylus, … J. W.-S. and C., and undefined 2017, 'Evolution of corrosion resistance and passive film properties of Ni-Mo alloy coatings during exposure to 0.5 M NaCl solution', *ElsevierA Laszczyńska, W Tylus, J Winiarski, I SzczygiełSurface and Coatings Technology, 2017,* doi.org/10.1016/j.surfcoat.2017.03.043

[7] T. Akiyama and H. Fukushima, 'Recent Study on the Mechanism of the Electrodeposition of Iron-group Metal Alloys', *ISIJ International*, vol. 32, no. 7, pp. 787–798, Jul. 1992, doi: 10.2355/ISIJINTERNATIONAL.32.787.

[8] J. Winiarski, 'The effect of current density on the structure and mechanical properties of protective Zn–Fe–Mo alloy coatings electrodeposited on a mild steel', *Mater. Chem. Phys.*, vol. 239, p. 122258, Jan. 2020, doi: 10.1016/J.MATCHEMPHYS.2019.122258.

[9] D. Kosugi *et al.*, 'Effect of the Addition of Molybdenum on the Structure and Corrosion Resistance of Zinc–Iron Plating', *Coatings 2017, Vol. 7,* vol. 7, no. 12, Dec. 2017, doi: 10.3390/COATINGS7120235.

[10] F. Assaf, M. Abou-Krisha, T. A. Yousef, A. Abushoffa, F. El-Sheref, and A. Toghan, 'Influence of current density on the mechanism of electrodeposition and dissolution of Zn–Fe–Co alloys', *SpringerF Assaf, M Abou-Krisha, TA Yousef, A Abushoffa, F El-Sheref, A ToghanRussian Journal of Physical Chemistry A, 2020•Springer*, vol. 94, no. 8, pp. 1708–1715, Aug. 2020, doi: 10.1134/S0036024420080026.

[11] R. C. Alkire, 'Historical Perspectives on Electroplating during the Past 100 Years', *ECS Meeting Abstracts*, vol. MA2022-02, no. 24, p. 1000, Oct. 2022, doi: 10.1149/MA2022-02241000MTGABS.

[12] ‘Electroplating | Metal Coating & Finishing Techniques | Britannica’. Accessed: Mar. 03, 2025. [Online]. Available: https://www.britannica.com/technology/electroplating

[13] L. B. Hunt, ‘The early history of gold plating - A tangled tale of disputed priorities’, *Gold Bull.*, vol. 6, no. 1, pp. 16–27, Mar. 1973, doi: 10.1007/BF03215178.

[14] J. E. Greene, ‘Tracing the 5000-year recorded history of inorganic thin films from ∼3000 BC to the early 1900s AD’, *Appl. Phys. Rev.*, vol. 1, no. 4, p. 041302, Dec. 2014, doi: 10.1063/1.4902760.

[15] R. Veinthal *et al.*, ‘Coatings and surface engineering. Industry oriented research’, *kirj.eeR Veinthal, P Kulu, A Zikin, H Sarjas, M Antonov, V Podgurski, E AdobergEstonian Journal of Engineering, 2012•kirj.ee*, vol. 18, no. 3, pp. 176–184, 2012, doi: 10.3176/eng.2012.3.02.

[16] C. L.-T. of the IMF and undefined 2012, ‘Global comparisons of metal finishing sectors: Part 2, some technology and operational variations’, *Taylor & FrancisC LarsonTransactions of the IMF, 2012•Taylor & Francis*, vol. 90, no. 5, pp. 232–236, 2012, doi: 10.1179/0020296712Z.00000000054.

[17] P. Nuss and M. J. Eckelman, ‘Life Cycle Assessment of Metals: A Scientific Synthesis’, *PLoS One*, vol. 9, no. 7, p. e101298, Jul. 2014, doi: 10.1371/JOURNAL.PONE.0101298.

[18] F. Presuel-Moreno, M. A. Jakab, N. Tailleart, M. Goldman, and J. R. Scully, ‘Corrosion-resistant metallic coatings’, *Materials Today*, vol. 11, no. 10, pp. 14–23, Oct. 2008, doi: 10.1016/S1369-7021(08)70203-7.

[19] M. Innocenti *et al.*, ‘Sustainability in the Electroplating Industry: A Challenge to Overcome’, *Meeting abstracts*, vol. MA2024-02, no. 22, pp. 1930–1930, Nov. 2024, doi: 10.1149/MA2024-02221930MTGABS.

[20] T. A. Kurilina, O. G. Dubrovskaya, V. A. Kulagin, A. I. Matyushenko, and A. G. Bobrik, ‘The Prospects of Utilizing the Modified Sorption Material to Intensify Purification of Waste Water from Electroplating Production’, *Journal of Siberian Federal University: Engineering & Technologies*, vol. 12, no. 2, pp. 182–191, Mar. 2019, doi: 10.17516/1999-494X-0127.

[21] ‘Electroplating Market Size, Trends & Forecast, 2023-2033’. Accessed: Mar. 10, 2025. [Online]. Available: https://www.futuremarketinsights.com/reports/electroplating-market

[22] D.C. Yu and D.S. Tan, ‘Applications of copper plating technology to electronic materials’, *Electroplating Finishing*, vol. 26, no. 2, p. 43, 2007.

[23] H. P. Feng, T. Paudel, B. Yu, S. Chen, Z. F. Ren, and G. Chen, ‘Nanoparticle-enabled selective electrodeposition.’, *Advanced Materials*, vol. 23, no. 21, pp. 2454–2459, Jun. 2011, doi: 10.1002/ADMA.201004656.

[24] I. R. A. Christie, ‘Electroplating in the Electronics Industry’, *Transactions of The Institute of Metal Finishing*, vol. 60, no. 1, pp. 33–40, Jan. 1982, doi: 10.1080/00202967.1982.11870600.

[25] H. K. Straschil, I. Kadija, J. Maisano, and J. A. Abys, ‘Electroplating of Thick and Ductile Palladium-Nickel Alloys’, *Circuit World*, vol. 17, no. 2, pp. 9–15, Jan. 1991, doi: 10.1108/EB046121/FULL/HTML.

[26] ‘METHOD OF ELECTROPLATING PLASTIC SUBSTRATE - CAO DE TIAN’. Accessed: Feb. 02, 2026. [Online]. Available: https://www.freepatentsonline.com/y2016/0083859.html

[27] M. Verrucchi *et al.*, 'Electrodeposition of Sn-Ru Alloys by Using Direct, Pulsed, and Pulsed Reverse Current for Decorative Applications', *Materials*, vol. 17, no. 21, pp. 5326–5326, Oct. 2024, doi: 10.3390/MA17215326.

[28] W. Giurlani *et al.*, 'New Frontiers in Electrodeposition for More Sustainable Electroplating Processes', *Meeting abstracts*, vol. MA2022-02, no. 23, pp. 956–956, Oct. 2022, doi: 10.1149/MA2022-0223956MTGABS.

[29] V. S. Protsenko and F. I. Danilov, 'Current Trends in Electrodeposition of Electrocatalytic Coatings', *Methods for Electrocatalysis: Advanced Materials and Allied Applications*, pp. 263–299, Jan. 2020, doi: 10.1007/978-3-030-27161-9_11.

[30] B. N. Popov, 'Electrodeposition of alloys and composites with superior corrosion and electrocatalytic properties..', *Plating and surface finishing* , vol. 91, no. 10, pp. 40–49, 2004.

[31] A. Yli-Pentti, 'Electroplating and Electroless Plating', *Comprehensive Materials Processing: Thirteen Volume Set*, vol. 4, pp. V4-277-V4-306, Jan. 2014, doi: 10.1016/B978-0-08-096532-1.00413-1.

[32] I. S. Aisyah, R. R. Susilo, and Murjito, 'The effect of distance variation on electroplating process of decorative nickel-chrome on the microstructure, thickness and weight of plating on A36 steel', *Nucleation and Atmospheric Aerosols*, vol. 2453, Jan. 2022, doi: 10.1063/5.0094401.

[33] B. Valdez, M. Schorr, R. Zlatev, … M. C.-E. and, and undefined 2012, 'Corrosion control in industry', *intechopen.comB Valdez, M Schorr, R Zlatev, M Carrillo, M Stoytcheva, L Alvarez, A Eliezer, N RosasEnvironmental and Industrial Corrosion-Practical and Theoretical Aspects, 2012*

[34] K. S. Ryder, C. Lei, A. J. Lucio, and S. Viles, 'Perspectives for Deep Eutectic Solvents and Ionic Liquid Analogues in Metal Electroplating', *Meeting abstracts*, vol. MA2022-02, no. 24, pp. 1010–1010, Oct. 2022, doi: 10.1149/MA2022-02241010MTGABS.

[35] J. G. dos R. da Costa, J. M. Costa, and A. F. de Almeida Neto, 'Progress on Electrodeposition of Metals and Alloys Using Ionic Liquids as Electrolytes', *Superalloys*, vol. 12, no. 12, pp. 2095–2095, Dec. 2022, doi: 10.3390/MET12122095.

[36] I. R. A. Christie, 'Electroplating in the Electronics Industry', *Transactions of The Institute of Metal Finishing*, vol. 60, no. 1, pp. 33–40, Jan. 1982, doi: 10.1080/00202967.1982.11870600.

[37] M. Becker *et al.*, 'Application of electroplating in MEMS-micromachining exemplified by a microrelay', *Microsystem Technologies-micro-and Nanosystems-information Storage and Processing Systems*, vol. 7, no. 4, pp. 196–202, Feb. 2001, doi: 10.1007/S005420000086.

[38] W. Ruythooren *et al.*, 'Electrodeposition for the synthesis of microsystems', *Journal of Micromechanics and Microengineering*, vol. 10, no. 2, p. 101, Jun. 2000, doi: 10.1088/0960-1317/10/2/301.

[39] J. Thomas and D. Milosevic, 'An Application Based Introduction to the Brush Plating Technique', *Meeting abstracts*, vol. MA2022-02, no. 26, pp. 1012–1012, Oct. 2022, doi: 10.1149/MA2022-02261012MTGABS.

[40] L. Xu *et al.*, 'Electroplating of Thick Hard Chromium Coating from a Trivalent Chromium Bath Containing a Ternary Complexing Agent: A Methodological and Mechanistic Study', *ACS*

Sustain. Chem. Eng., vol. 8, no. 41, pp. 15540–15549, Sep. 2020, doi: 10.1021/ACSSUSCHEMENG.0C04529.

[41] 'Corrosion Resistance of Zinc Plating - Sharretts Plating Company'. Accessed: Mar. 10, 2025. [Online]. Available: https://www.sharrettsplating.com/blog/corrosion-resistance-of-zinc-plating/

[42] 'The Benefits of Selecting Zinc-Coated Metal for Commercial Building Products | Activar Construction Products Group'. Accessed: Mar. 10, 2025. [Online]. Available: https://www.activarcpg.com/benefits-of-zinc-coated-metal/

[43] W. Giurlani *et al.*, 'Electroplating for Decorative Applications: Recent Trends in Research and Development', *Coatings 2018, Vol. 8, Page 260*, vol. 8, no. 8, p. 260, Jul. 2018, doi: 10.3390/COATINGS8080260.

[44] P. M.-B. of Electrochemistry and undefined 2000, 'Critical review on alloy plating: A viable alternative to conventional plating', *cecri.csircentral.netP MalathyBulletin of Electrochemistry, 2000•cecri.csircentral.net*, vol. 16, no. 12, pp. 3–50, 2000,

[45] K. K. Maniam and S. Paul, 'Corrosion Performance of Electrodeposited Zinc and Zinc-Alloy Coatings in Marine Environment', *Corrosion and Materials Degradation*, vol. 2, no. 2, pp. 163–189, Apr. 2021, doi: 10.3390/CMD2020010.

[46] A. B. Pop, G. Iepure, A. M. Titu, and S. Ravai-Nagy, 'Characterization and Corrosion Behavior of Zinc Coatings for Two Anti-Corrosive Protections: A Detailed Study', *Coatings*, vol. 13, no. 8, Aug. 2023, doi: 10.3390/COATINGS13081460.

[47] A. Keyvani, M. Yeganeh, and H. Rezaeyan, 'Electrodeposition of Zn-Co-Mo Alloy on the Steel Substrate from Citrate Bath and Its Corrosion Behavior in the Chloride Media', *J. Mater. Eng. Perform.*, vol. 26, no. 4, pp. 1958–1966, Mar. 2017, doi: 10.1007/S11665-017-2619-5.

[48] S. Awasthi, B. P. Palomero, A. Srivastava, S. Selvaraj, D. Kumar, and S. K. Pandey, 'Surface Functionalized Zinc Composite Coatings: A Review', *Adv. Eng. Mater.*, Dec. 2024, doi: 10.1002/ADEM.202401597.

[49] S. H. Bae, S. Oue, Y. K. Taninouchi, I. Son, and H. Nakano, 'Corrosion Resistance of Zn–Ni Alloy Films Electroplated in Alkaline Zincate Solutions Containing a Brightener', *Isij International*, vol. 63, no. 11, pp. 1897–1907, Nov. 2023, doi: 10.2355/ISIJINTERNATIONAL.ISIJINT-2023-236.

[50] W. Paatsch, W. Kautek, and M. Sahre, 'Corrosion behaviour and mechanical properties of plated Zn-alloys', *Transactions of The Institute of Metal Finishing*, vol. 75, no. 6, pp. 216–218, Jan. 1997, doi: 10.1080/00202967.1997.11871177.

[51] R. S. ; Bhat *et al.*, 'Structural Properties of Zn-Fe Alloy Coatings and Their Corrosion Resistance', *Coatings*, vol. 13, no. 4, pp. 772–772, Apr. 2023, doi: 10.3390/COATINGS13040772.

[52] C. M. P. Kumar, A. Lakshmikanthan, M. P. G. Chandrashekarappa, D. Y. Pimenov, and K. Giasin, 'Electrodeposition Based Preparation of Zn–Ni Alloy and Zn–Ni–WC Nano-Composite Coatings for Corrosion-Resistant Applications', *THE Coatings*, vol. 11, no. 6, p. 712, Jun. 2021, doi: 10.3390/COATINGS11060712.

[53] T. Monyai, O. S. I. Fayomi, A. P. I. Popoola, and O. Agboola, 'Integration of MoO_2 Composite on the Micro-evolution and Anticorrosion Mitigation of Zn–Ni–MoO_2 Thin Films Coating by Electrodeposition System', *J. Bio Tribocorros.*, vol. 5, no. 1, pp. 1–9, Mar. 2019, doi: 10.1007/S40735-018-0206-4.

[54] R. Ramanauskas, P. Quintana, L. Maldonado, R. Pomés, and M. A. Pech-Canul, 'Corrosion resistance and microstructure of electrodeposited Zn and Zn alloy coatings', *Surf. Coat. Technol.*, vol. 92, no. 1–2, pp. 16–21, Jun. 1997, doi: 10.1016/S0257-8972(96)03125-8.

[55] N. Lotfi, M. Aliofkhazraei, H. Rahmani, and G. B. Darband, 'Zinc–Nickel Alloy Electrodeposition: Characterization, Properties, Multilayers and Composites', *Protection of Metals and Physical Chemistry of Surfaces*, vol. 54, no. 6, pp. 1102–1140, Nov. 2018, doi: 10.1134/S2070205118060187.

[56] C. A. M. Dutra, J. W. J. Silva, and R. Z. Nakazato, 'Corrosion Resistance of Zn and Zn-Ni Electrodeposits: Morphological Characterization and Phases Identification', *Materials Sciences and Applications*, vol. 04, no. 10, pp. 644–648, 2013, doi: 10.4236/MSA.2013.410079.

[57] Z. F. Lodhi, J. M. C. Mol, A. Hovestad, L. 't Hoen-Velterop, H. Terryn, and J. H. W. de Wit, 'Corrosion resistance of Zn-Co-Fe alloy coatings on high strength steel', *Surf. Coat. Technol.*, vol. 203, no. 10–11, pp. 1415–1422, Feb. 2009, doi: 10.1016/j.surfcoat.2008.11.019.

[58] C. A. M. Dutra, R. M. de Oliveira, E. N. Codaro, H. de Felipe, and R. Z. Nakazato, 'ESTUDO DA CORROSÃO DE ELETRODEPÓSITOS DE Zn E ZnFeCo EM SOLUÇÃO DE NaCl NA PRESENÇA DOS OXI- ÂNIONS DO GRUPO VIB', pp. 205–214, Aug. 2009, doi: 10.5151/2594-5300-15295.

[59] J. S. Kavirajwar, S. Basavanna, and B. K. Devendra, 'An investigation on corrosion properties of bright Zn-Ni alloy coated mild steel', *Electrochemical Science Advances*, vol. 2, no. 5, p. e2100097, Oct. 2022, doi: 10.1002/ELSA.202100097.

[60] M. R. Lambert, R. G. Hart, H. E. Townsend, M. R. Lambert, R. G. Hart, and H. E. Townsend, 'Corrosion Mechanism of Zn-Ni Alloy Electrodeposited Coatings', *SAE Technical Papers*, Dec. 1983, doi: 10.4271/831817.

[61] G. D. Wilcox and D. R. Gabe, 'Electrodeposited zinc alloy coatings', *Corros. Sci.*, vol. 35, no. 5–8, pp. 1251–1258, 1993, doi: 10.1016/0010-938X(93)90345-H.

[62] P. P. Chung, J. Wang, and Y. Durandet, 'Deposition processes and properties of coatings on steel fasteners — A review', *Friction*, vol. 7, no. 5, pp. 389–416, Oct. 2019, doi: 10.1007/S40544-019-0304-4.

[63] R. Münz, G. K. Wolf, L. Guzman, and M. Adami, 'Zinc/manganese multilayer coatings for corrosion protection', *Thin Solid Films*, vol. 459, no. 1–2, pp. 297–302, Jul. 2004, doi: 10.1016/J.TSF.2003.12.148.

[64] I. Kozina, H. Krawiec, M. Starowicz, and M. Kawalec, 'Corrosion Resistance of MgZn Alloy Covered by Chitosan-Based Coatings', *International Journal of Molecular Sciences 2021, Vol. 22, Page 8301*, vol. 22, no. 15, p. 8301, Aug. 2021, doi: 10.3390/IJMS22158301.

[65] W. Wu, Z. Wang, S. Zang, X. Yu, H. Yang, and S. Chang, 'Research Progress on Surface Treatments of Biodegradable Mg Alloys: A Review', *ACS Omega*, vol. 5, no. 2, pp. 941–947,

Jan. 2020, doi: 10.1021/ACSOMEGA.9B03423/ASSET/IMAGES/LARGE/AO9B03423_0006.JPEG.

[66] G. U. Mingyuan, M. R. Notis, and A. R. Marder, 'The effect of continuous heating on the phase transformations in zinc- iron electrodeposited coatings', *Metallurgical Transactions A*, vol. 22, no. 8, pp. 1737–1743, Aug. 1991, doi: 10.1007/BF02646497.

[67] V. Narasimhamurthy and B. S. Sheshadri, 'Physico-chemical properties of Zn-Fe alloy deposits from an alkaline sulphate bath containing triethanolamine', *J. Appl. Electrochem.*, vol. 26, no. 1, pp. 90–94, 1996, doi: 10.1007/BF00248193.

[68] R. S. ; Bhat *et al.*, 'Structural properties of Zn-Fe alloy coatings and their corrosion resistance', *mdpi.comRS Bhat, MK Balakrishna, P Parthasarathy, AC HegdeCoatings, 2023•mdpi.com*, 2023, doi: 10.3390/coatings13040772.

[69] N. Eliaz, K. Venkatakrishna, and A. C. Hegde, 'Electroplating and characterization of Zn–Ni, Zn–Co and Zn–Ni–Co alloys', *Surf. Coat. Technol.*, vol. 205, no. 7, pp. 1969–1978, Dec. 2010, doi: 10.1016/j.surfcoat.2010.08.077.

[70] N. Eliaz and E. Gileadi, *Physical electrochemistry: fundamentals, techniques, and applications*. 2019. Accessed: May 13, 2025. [Online]. Available: https://books.google.com/books?hl=en&lr=&id=I3BuDwAAQBAJ&oi=fnd&pg=PR17&ots=nMFcla6pAp&sig=swpqCl8XN_4Q4-Ai2v9Y5cV4BvU

[71] N. Tsyntsaru, H. Cesiulis, M. Donten, J. Sort, E. Pellicer, and E. J. Podlaha-Murphy, 'Modern trends in tungsten alloys electrodeposition with iron group metals', *Surface Engineering and Applied Electrochemistry 2012 48:6*, vol. 48, no. 6, pp. 491–520, Feb. 2013, doi: 10.3103/S1068375512060038.

[72] T. Akiyama and H. Fukushima, 'Recent Study on the Mechanism of the Electrodeposition of Iron-group Metal Alloys', *Isij International*, vol. 32, no. 7, pp. 787–798, 1992, doi: 10.2355/isijinternational.32.787.

[73] J. Winiarski, W. Tylus, A. Lutz, I. De Graeve, B. S.-C. Science, and undefined 2018, 'The study on the corrosion mechanism of protective ternary ZnFeMo alloy coatings deposited on carbon steel in 0.5 mol dm–3 NaCl solution', *ElsevierJ Winiarski, W Tylus, A Lutz, I De Graeve, B SzczygiełCorrosion Science, 2018,* doi.org/10.1016/j.corsci.2018.04.011

[74] J. Winiarski, A. Leśniewicz, P. Pohl, and B. Szczygieł, 'The effect of pH of plating bath on electrodeposition and properties of protective ternary Zn–Fe–Mo alloy coatings', *Surf. Coat. Technol.*, vol. 299, pp. 81–89, Aug. 2016, doi: 10.1016/j.surfcoat.2016.04.073.

[75] Y. Jinku, Z. Lili, S. Hui, W. Yuehua, … Y. M.-R. M. M., and undefined 2018, 'Effect of Processing Parameters and Ascorbic Acid on the Electrodeposition NiFeW Alloy Coatings', *Elsevier*, Accessed: Apr. 07, 2025. doi.org/10.1016/S1875-5372(18)30084-5

[76] J. Park, T. Hagio, … Y. K.-J. of the, and undefined 2020, 'Electrodeposition of a novel ternary Fe–W–Zn alloy: Tuning corrosion properties of Fe–W based alloys by Zn addition', *iopscience.iop.orgJH Park, T Hagio, Y Kamimoto, R IchinoJournal of the Electrochemical Society, 2020•iopscience.iop.org*, 2020, doi: 10.1149/1945-7111/abbe59.

[77] A. Brenner, *Electrodeposition of Alloys: Practical and specific information*, vol. 2. Academic Press, 1963.

[78] D. Rashmi, G. P. Pavithra, B. M. Praveen, D. Devapal, K. O. Nayana, and S. P. Hebbar, 'Characterization and Corrosion Analysis of Electrodeposited Nanostructured Zn–Fe Alloy Coatings', *J. Bio Tribocorros.*, vol. 6, no. 3, pp. 1–8, Sep. 2020, doi: 10.1007/S40735-020-00380-9.

[79] B. Szczygiel and A. Laszczynska, 'Influence of bath concentration and pH on electrodeposition process of ternary Zn-Ni-Mo alloy coatings', *Transactions of the IMF*, vol. 92, no. 4, pp. 196–202, 2014, doi: 10.1179/0020296714Z.000000000183.

[80] C. Wang, 'Influence of Concentration of Zn~(2+) and Ni~(2+) in Bath on Content of Nickel in Electroplated Zn-Ni Alloy Coating.', *Materials protection,* 2008.

[81] M. M. Abou-Krisha, F. H. Assaf, O. K. Alduaij, and A. A. Eissa, 'Deposition Potential Influence on the Electrodeposition of Zn–Ni–Mn Alloy', *Transactions of the Indian Institute of Metals*, vol. 70, no. 1, pp. 31–40, Jan. 2017, doi: 10.1007/S12666-016-0859-Y/FULLTEXT.HTML.

[82] A. Laszczyńska, J. Winiarski, B. Szczygieł, and I. Szczygieł, 'Electrodeposition and characterization of Ni–Mo–ZrO2 composite coatings', *Appl. Surf. Sci.*, vol. 369, pp. 224–231, Apr. 2016, doi: 10.1016/J.APSUSC.2016.02.086.

[83] A. Apelblat, 'Citric Acid', 2014, doi: 10.1007/978-3-319-11233-6.

[84] Z. Yue, M. Muig, X. Xiao-Ming, … L. Z.-C. J. of, and undefined 2000, 'Kinetic model of induced codeposition of Ni-Mo alloys', *Wiley Online LibraryZ Yue, M Muig, X Xiao-Ming, L Ze-Lin, L Shi-Xun, Z Sbao-MinChinese Journal of Chemistry, 2000•Wiley Online Library*, vol. 18, no. 1, pp. 29–34, 2000, doi: 10.1002/cjoc.20000180106.

[85] E. Caldin, M. Grant, B. H.-J. of the C. Society, and undefined 1972, 'Kinetics and thermodynamics of the complex-formation of nickel (II) and cobalt (II) ions with ammonia and pyridine-2-azodimethylaniline in water, at pressures from 1', *pubs.rsc.orgEF Caldin, MW Grant, BB HasinoffJournal of the Chemical Society, Faraday Transactions 1: Physical, 1972•pubs.rsc.org*, 1972, **https://doi.org/10.1039/F19726802247**

[86] S. Harsimran, K. Santosh, and K. Rakesh, 'OVERVIEW OF CORROSION AND ITS CONTROL: A CRITICAL REVIEW', *Proceedings on Engineering Sciences*, vol. 3, no. 1, pp. 13–24, 2021, doi: 10.24874/PES03.01.002.

[87] P. Pedeferri, 'Corrosion Science and Engineering', *Corrosion Science and Engineering*, 2018, doi: 10.1007/978-3-319-97625-9.

[88] A. I. Ayodeji, O. S. I. Fayomi, A. A. Daniyan, K. O. Babaremu, P. O. Abioye, and O. Agboola, 'Corrosion Phenomena and the Occurrences; A comment', *IOP Conf. Ser. Mater. Sci. Eng.*, vol. 1107, no. 1, p. 012101, Apr. 2021, doi: 10.1088/1757-899X/1107/1/012101.

[89] H. Tamura, 'The role of rusts in corrosion and corrosion protection of iron and steel', *Corros. Sci.*, vol. 50, no. 7, pp. 1872–1883, Jul. 2008, doi: 10.1016/J.CORSCI.2008.03.008.

[90] D. Dwivedi, K. Lepková, and T. Becker, 'Carbon steel corrosion: a review of key surface properties and characterization methods', *RSC Adv.*, vol. 7, no. 8, pp. 4580–4610, 2017, doi: 10.1039/C6RA25094G.

[91] A. I. Biryukov, O. A. Kozaderov, and T. V. Batmanova, 'Features of the corrosion of coatings based on zinc alloys: oxidation products and the selective dissolution of zinc. Review',

Kondensirovannye sredy i mežfaznye granicy, vol. 26, no. 1, pp. 25–36, Jan. 2024, doi: 10.17308/KCMF.2024.26/11806.

[92] F. Feldmann, L. L. E. Mears, M. Roth, and M. Valtiner, 'Characterisation of the galvanic protection of zinc flake coating by spectroelectrochemistry and industrial testing', *Materials and Corrosion-werkstoffe Und Korrosion*, vol. 74, no. 8, pp. 1148–1158, May 2023, doi: 10.1002/MACO.202213719.

[93] D. K. H. and M. S. K. H. Y. Kim, 'Zinc alloy coated steel having excellent corrosion resistance and surface property method for manufacturing the same', Jun. 2020.

[94] A. N. C. Costa, G. C. Silva, E. A. Ferreira, and R. Z. Nakazato, 'Comparative analysis of corrosion resistance of Zinc and Zn-Al-Mg coatings on carbon steel', *Research, Society and Development*, vol. 10, no. 1, pp. e49810111973–e49810111973, Jan. 2021, doi: 10.33448/RSD-V10I1.11973.

[95] P. D. L. Neto, A. N. Correia, R. P. Colares, and W. S. Araujo, 'Corrosion study of electrodeposited Zn and Zn-Co coatings in chloride medium', *J. Braz. Chem. Soc.*, vol. 18, no. 6, pp. 1164–1175, 2007, doi: 10.1590/S0103-50532007000600010.

[96] K.-T. Bae, J.-H. La, K.-B. Kim, and S.-Y. Lee, 'The Study on the Corrosion Property of the Zn-Mg Alloy Coatings with Various Mg Contents using EIS Measurement', *Journal of the Korean institute of surface engineering*, vol. 47, no. 6, pp. 330–334, Dec. 2014, doi: 10.5695/JKISE.2014.47.6.330.

[97] V. Barranco, S. Feliu, and S. Feliu, 'EIS study of the corrosion behaviour of zinc-based coatings on steel in quiescent 3% NaCl solution. Part 1: Directly exposed coatings', *Corros. Sci.*, vol. 46, no. 9, pp. 2203–2220, Sep. 2004, doi: 10.1016/J.CORSCI.2003.09.032.

[98] J. J. Duprat and M. Kelly, 'Dedicated processes for electroplating on fasteners', *National Association for Surface Finishing Annual Technical Conference 2009, SUR/FIN 2009*, pp. 481–493, Jan. 2009.

[99] M. Babutzka, S. Grabowski, H. Sahrhage, and T. Lampke, 'Electrochemical Corrosion Investigations on Binary and Ternary Zinc Alloy Coatings using Gel Electrolytes', *Adv. Eng. Mater.*, vol. 24, no. 6, p. 2101336, Jun. 2022, doi: 10.1002/ADEM.202101336.

[100] T. Zhou, M. İ. Coşkun, S. Sanders, A. M. A. Mohamed, and T. D. Golden, 'Corrosion protection of Zn-Mo coatings electrodeposited from alkaline solutions', *Surf. Coat. Technol.*, vol. 467, p. 129737, Aug. 2023, doi: 10.1016/J.SURFCOAT.2023.129737.

[101] Y. M. Panchenko, A. I. Marshakov, T. N. Igonin, T. A. Nenasheva, L. A. Nikolaeva, and A. A. Ivanenko, 'Corrosion Resistance of Zinc and Zinc-Aluminum-Magnesium Coatings in Atmosphere on the Territory of Russia', *Materials 2023, Vol. 16, Page 5214*, vol. 16, no. 15, p. 5214, Jul. 2023, doi: 10.3390/MA16155214.

[102] S. Fashu and R. Khan, 'Electrodeposition of ternary Zn–Ni–Sn alloys from an ionic liquid based on choline chloride and their characterisation', *Transactions of The Institute of Metal Finishing*, vol. 94, no. 5, pp. 237–245, Sep. 2016, doi: 10.1080/00202967.2016.1209920.

[103] D. W. Ernst and M. L. Holt, 'Cathode Potentials during the Electrodeposition of Molybdenum Alloys from Aqueous Solutions', *J. Electrochem. Soc.*, vol. 105, no. 11, p. 686, Nov. 1958, doi: 10.1149/1.2428691/XML.

[104] G. Trejo, R. Ortega, Y. Meas, E. Chainet, and P. Ozil, 'Effect of benzylideneacetone on the electrodeposition mechanism of Zn-Co alloy', *J. Appl. Electrochem.*, vol. 33, no. 5, pp. 373–379, May 2003, doi: 10.1023/A:1024466604939/METRICS.

[105] P. Vukosav, M. Mlakar, and V. TomiŠić, 'Revision of iron(III)–citrate speciation in aqueous solution. Voltammetric and spectrophotometric studies', *Anal. Chim. Acta*, vol. 745, pp. 85–91, Oct. 2012, doi: 10.1016/J.ACA.2012.07.036.

[106] R. A. Løvstad, 'Interaction of serum albumin with the Fe(III)-citrate complex', *International Journal of Biochemistry*, vol. 25, no. 7, pp. 1015–1017, 1993, doi: 10.1016/0020-711X(93)90115-U.

[107] S. A. Ahmad, M. Y. Shukor, N. A. Shamaan, W. P. Mac Cormack, and M. A. Syed, 'Molybdate reduction to molybdenum blue by an Antarctic bacterium', *Biomed Res. Int.*, vol. 2013, 2013, doi: 10.1155/2013/871941.

[108] M. Myachina, N. Gavrilova, and V. Nazarov, 'Formation of Molybdenum Blue Nanoparticles in the Organic Reducing Area', *Molecules 2021, Vol. 26, Page 4438*, vol. 26, no. 15, p. 4438, Jul. 2021, doi: 10.3390/MOLECULES26154438.

[109] S. Yoshio, M. Wakabayashi, and K. Adachi, 'Cesium polytungstates with blue-tint-tunable near-infrared absorption', *RSC Adv.*, vol. 10, no. 18, pp. 10491–10501, Mar. 2020, doi: 10.1039/D0RA00505C.

[110] W. L. N. Dayaratne, R. Torres-Cadena, B. P. Schmitt, E. M. Westrick, and A. Jaffe, 'Hybrid bronzes: mixed-valence organic–inorganic metal oxides as a tunable material platform', *Chem. Sci.*, vol. 14, no. 39, p. 10756, Sep. 2023, doi: 10.1039/D3SC03828A.

[111] Y. Nakagawa, Y. Shiratsuchi, T. Shibayama, and M. Takeguchi, 'Ultraviolet Light-Induced Surface Changes of Tungsten Oxide in Air: Combined Scanning Transmission Electron Microscopy and X-ray Photoelectron Spectroscopy Analysis', *Nanomaterials 2024, Vol. 14, Page 1486*, vol. 14, no. 18, p. 1486, Sep. 2024, doi: 10.3390/NANO14181486.

[112] R. S. Fernandes and N. Dey, 'Ion-specific bathochromic shifts: Simultaneous detection of multiple heavy metal pollutants via charge transfer interactions', *J. Mol. Liq.*, vol. 367, p. 120369, Dec. 2022, doi: 10.1016/J.MOLLIQ.2022.120369.

[113] D. Mohammadyani and M. H. Sohi, 'MORPHOLOGICAL STUDY OF PULSE CURRENT ELECTRODEPOSITED Zn-Fe ALLOY', *Int. J. Mod. Phys. B*, vol. 22, no. 18–19, pp. 3023–3030, Jul. 2008, doi: 10.1142/S0217979208047882.

[114] B. YUAN, K. LIU, and M. KOWAKA, 'Electrodeposition of Amorphous Ni-Mo Alloys from Ammonia Citrate Bath and Their Corrosion Resisitance', *Journal of The Surface Finishing Society of Japan*, vol. 42, no. 6, pp. 639–644, Jun. 1991, doi: 10.4139/SFJ.42.639.

[115] H. Kazimierczak, P. Ozga, and R. P. Socha, 'Investigation of electrochemical co-deposition of zinc and molybdenum from citrate solutions', *Electrochim. Acta*, vol. 104, pp. 378–390, Aug. 2013, doi: 10.1016/J.ELECTACTA.2012.12.140.

[116] H. M. Shoaib, K. Winiarska, and J. Winiarski, 'Preliminary studies on electrodeposition of Zn-Fe-W alloy coatings from citrate-sulphate baths', *Ochrona przed Korozją*, vol. 66, no. 2, pp. 44–47, 2023, doi: 10.15199/40.2023.2.2.

[117] D. T. To, S. H. Park, M. J. Kim, H. S. Cho, and N. V. Myung, 'Effects of NH4 +/citrate complexing agent ratio on Ni–Mo and Ni–Mo–O electrodeposits from ammonium citrate baths', *Front. Chem.*, vol. 10, Aug. 2022, doi: 10.3389/FCHEM.2022.942423.

[118] F. Cao *et al.*, 'A Study on the Influence of the Electroplating Process on the Corrosion Resistance of Zinc-Based Alloy Coatings', *Coatings 2023, Vol. 13, Page 1774*, vol. 13, no. 10, p. 1774, Oct. 2023, doi: 10.3390/COATINGS13101774.

[119] I. Rodriguez-Torres, G. Valentin, and F. Lapicque, 'Electrodeposition of zinc-nickel alloys from ammonia-containing baths', *J. Appl. Electrochem.*, vol. 29, no. 9, pp. 1035–1044, 1999, doi: 10.1023/A:1003610617785.

[120] V. B. Mišković-Stanković, J. B. Zotović, Z. Kačarević-Popović, and M. D. Maksimović, 'Corrosion behaviour of epoxy coatings electrodeposited on steel electrochemically modified by Zn–Ni alloy', *Electrochim. Acta*, vol. 44, no. 24, pp. 4269–4277, Jul. 1999, doi: 10.1016/S0013-4686(99)00142-5.

[121] R. S. Bhat and A. C. Hegde, 'Electrodeposition of Cyclic Multilayer Zn-Co Films Using Square Current Pulses and Investigaions on Their Corrosion Behaviors', *Journal of Minerals and Materials Characterization and Engineering*, vol. 11, no. 09, pp. 896–903, 2012, doi: 10.4236/JMMCE.2012.119085.

[122] M. P. Pavlov, N. V. Morozova, and V. N. Kudryavtsev, 'Electrodeposition of nickel-molybdenum alloys from ammonium citrate baths containing intermediate valence molybdenum compounds', *Protection of Metals*, vol. 43, no. 5, pp. 459–464, Sep. 2007, doi: 10.1134/S0033173207050074.